中国科学院北京天文台

博士学位论文

太阳大气中磁场空间结构的研究

张 枚

导　　师：张洪起　研究员
专　　业：天体物理
研究方向：太阳磁场

一九九九年七月

Beijing Astronomical Observatory
Chinese Academy of Sciences

Ph.D. Degree Dissertation

A Study of Spatial Structure of Magnetic Fields in Solar Atmosphere

by

Mei Zhang

Beijing Astronomical Observatory
Chinese Academy of Sciences
Beijing 100012, P.R.China

July 1999

目 录

摘 要

本论文对传统的描述太阳大气中磁流管空间结构的伞盖模型进行了观测和理论上的探讨。作者在论文中的主要贡献为：

1. 对从日面中心到边缘的宁静区光球磁场进行了观测。观测表明，宁静区磁元在光球层的水平分量很小，没有形成在活动区附近观测到的伞盖结构。

2. 对日面边缘的光球磁场进行了分析与观测。发现太阳赤道与南北极的磁场结构存在着不同。太阳赤道附近宁静区磁元的水平分量较小，而南北极附近磁元则存在着一定的水平分量。这一现象亦被整个日面边缘光球磁场的观测所证实。

3. 采用超深积分方法，在世界上首次得到了高信躁比的色球宁静区磁图。首次观测到了色球层上的宁静区网络内磁元结构。发现光球层磁元与色球层磁元的结构非常相似并且它们的演化有一一对应关系。

4．对传统的伞盖模型进行了理论分析。分析表明，磁流管的形状以及磁流管中的磁场结构特征可能存在着多样性。同一磁流管中，不同伞盖高度的定义将给出不同的伞盖高度。不同作者对伞盖高度的定义不同可能是造成不同作者对伞盖高度值估计不同的部分原因。

5．对 FeI5324 和 H_β谱线的形成深度进行了探讨。对日面边缘 H_β谱线在光球以上的形成厚度进行了观测估计。

6．讨论了色球宁静区磁场观测结果对理论模型可能有的限制。分析表明，当 H_β谱线形成在一定高度以上时，部分伞盖模型将不能很好地解释观测事实。

7．通过将太阳过渡区及日冕的紫外观测与怀柔光球磁图进行比较，探讨

了日冕及过渡区磁场的可能形式。发现紫外像中亮丝结构的根部位于光球磁元中心。紫外像中亮丝结构的宽度不变可能反映了磁场在从光球向日冕发展过程中扩散不大。

8．通过综合各方面观测研究及理论分析，作者提出了太阳磁场结构的纤维树模型，并探讨了这种模型对日冕及色球加热的意义。

ABSTRACT

Observational and theoretical studies on the traditional canopy model, which described the spatial structures of magnetic tubes in the solar atmosphere, have been discussed in this dissertation. The author's main contributions are:

1. Center-to-limb photospheric magnetic fields of small-scale magnetic flux tubes have been observed from near solar disk center to solar west limb. The observation shows that the small-scale magnetic elements in quiet-Sun regions show little horizontal components and have not formed that kind of magnetic canopies observed near the active regions.

2. Solar polar and equatorial limb photospheric magnetic fields have been observed and analyzed. It is found that the spatial configurations of small-scale magnetic flux tubes near the solar southern and northern poles are different from those near the equatorial limbs. The horizontal components of those small-scale magnetic elements near the equatorial limbs are quite small, while those small-scale magnetic elements near solar southern and northern poles show a certain horizontal components. This phenomenon is also found by the observation of photospheric magnetic fields near the whole solar limb.

3. Using deep integration method, high signal-to-noise chromospheric magnetograms of quiet-Sun regions have been archived. The intranetwork magnetic elements have been found in the solar chromosphere. It is found that the magnetic structures of photospheric and chromospheric elements look similar each other and there is a corresponding variation between identical photospheric and chromospheric magnetic elements.

4. Theoretical analysis has been made on a simple canopy model. The analysis shows that the shapes of magnetic tubes and the magnetic structures within the tubes may be diversified. The calculated canopy heights may be different due to different definitions. The different estimated values of canopy heights by different authors may partially caused by their different definitions of canopy heights.

5. The formation heights of FeI5324 and H_β lines have been discussed briefly. The formation width of the H_β line above the photosphere has been measured in the solar limb.

6. Observational constrains of our deep chromospheric observations on the canopy models have been discussed. If the H_β line formed above a certain height above the photosphere, then some canopy models may have difficulties in fitting our quiet-Sun observations.

7. By comparing the TRACE ultraviolet observations with our photospheric magnetic field observations, the possible magnetic structures in the solar transition region and corona have been discussed. The fibril structures in the ultraviolet image root near the centers of photospheric magnetic elements. The little-changed fibril widths may imply that the thin magnetic tubes have little expansions when extending from photosphere to high solar atmosphere.

8. Based on various observations and analysis, a possible magnetic structure model (fibril-tree model) has been proposed. The meaning of this model on heating the solar chromosphere and coronal is also mentioned.

第一章 导 论

1．1 研究太阳磁场空间结构的意义

1．1．1 研究太阳活动的意义

太阳是离我们最近的一颗恒星，也是唯一可以作为面源观测的恒星。对太阳上各种物理现象的充分观测给我们提供了一个内涵丰富的物理实验室，用以检验各种物理理论的适用性。同时，太阳又是唯一一颗与地球生命直接相关的恒星。太阳风和日冕物质抛射（CME）带来的日地空间电离层的变化将直接影响地球大气外层空间以及可能带来的地球大气的许多变化。因此，充分理解太阳以及太阳上的各种物理现象无疑将是十分必要和十分有意义的。

1．1．2 研究太阳磁场的意义

目前普遍认为，太阳磁场在太阳各种物理现象中起着主要的作用。太阳磁场可能是太阳上各种活动现象，如太阳黑子、太阳耀斑以及日冕物质抛射等的主导因素。因此，要想掌握太阳活动的规律以及这些活动对人类的影响，掌握太阳磁场的规律无疑是十分重要的。

1．1．3 研究太阳磁场空间结构的意义

了解太阳磁场的物理规律包括了解它的产生、发展及演化。目前人们普遍认为太阳磁场是通过由 Dynamo 理论描述的发电机在太阳对流层中产生的[1]。随着太阳磁场从太阳内部向外扩展，太阳磁场将形成一定的结构。这种结构又会随时间演化。

虽然要想从整体上把握太阳磁场的规律就要从其产生、发展到演化来共同考虑，但在实际过程中，我们通常把问题分解开来，采取各个突破的办法，而太阳磁场空间结构的研究就成了其中不可缺少的一环。

1．1．4 研究磁流管空间结构的意义

虽然太阳磁场的表现形式多种多样，但人们普遍认为它们都是由小的磁流管组成的。较强的磁场是由大量的集中的小磁流管组成的，而较弱的磁场区域是由个别的或少数的磁流管组成的。当然，人们有时也把一个活动区整体上当作一个大磁流管来处理。因此，了解作为磁场组件的磁流管的空间结构就显得十分必要。

1．2 磁流管空间结构的伞盖模型

1．2．1 概念的提出

太阳磁场在光球层是以孤立磁流管的形式存在的，这已是大多数太阳物理学家普遍承认的事实[2]。但是，对磁流管在色球及日冕的扩展形式，则尚无统一的认识。较为流行的观点是 Gabriel 于 1976 年提出的伞盖模型[3]。如图 1.1 即为一张标准伞盖模型的示意图。这种模型认为，磁流管在从光球向色球及太阳高层大气扩散的过程中，由于内外压力差，磁流管会不断地膨胀，直至充满整个色球和日冕空间。Gabriel 的模型计算出磁流管在高出光球 1500 - 2500 公里处膨胀到充满整个空间而形成覆盖整个色球和日冕的伞盖。这种模型被用来解释一些色球和日冕层中的现象[4-6]。

1．2．2 观测的挑战

八十年代初，Giovanelli 等人利用美国国立天文台中等分辨率的磁象仪进行了一系列的工作。他们通过观测活动区和增强网络区附近的磁场，提出了伞盖高度并没有理论计算的那么高的观点[7-12]。他们认为伞盖高度只高出光球层 200 - 800 公里。

1．2．3 进一步的观测

随后，一些天文学家在太阳黑子附近进行了一系列观测[13-16]，试图探

讨伞盖高度到底有多高。他们发现，太阳磁场从黑子向外扩展，具有较强的水平分量，可以用伞盖高度很低、甚至处于中上光球层的伞盖模型来描述[13]。

1．2．4 进一步的理论模型

与此同时，理论天文学家也计算了各种物理条件下的不同伞盖模型[17-20]。虽然他们努力调整他们的模型以降低伞盖高度，却发现始终无法将理论的伞盖高度降至观测的伞盖高度。

1．2．5 研究的意义

可见，对于伞盖模型，理论和观测的探讨一直存在着分歧。如何解决和解释这种分歧，就成为当前急需解决的问题。我们注意到，以往的观测通常集中在太阳活动区或增强网络区域，而理论模型往往都是从宁静区磁流管物理条件推出的。因此，为了直接检验从宁静区磁流管物理条件推出的理论模型是否正确，直接观测宁静区的磁流管的空间结构就显得十分必要。同时，我们也考虑了是否分歧是产生于对观测和理论模型的解释上，从而对模型本身也进行了一定的探讨。

1．3 怀柔太阳观测站望远镜简介

此节(§1.3)部分内容摘自怀柔太阳观测站主页。网址：159.226.88.48。

1．3．1 台址简介

怀柔太阳磁场望远镜座落于离北京 60 公里的怀柔水库北岸的一个小岛上。小岛一面靠山，三面环水。东西南方向都环绕着大约 2 公里的水域。望远镜处于离水面大约 31 米高的观测塔顶平台上（见图 1.2)。望远镜的圆顶是可移动的。在天气较好的情况下，圆顶可以被拖出，从而使大气扰动的影响降至最低。小岛处于东经 116.6 度，北纬 40.4 度，海拔 62 米。全年可观测日大约为 300 天。

1．3．2 太阳磁场望远镜

1．3．2．1 组成

太阳磁场望远镜[21]由一个口径 35 厘米的真空折射镜，一个装配三组宽视场 KD*P 电光调制器、半宽为 1/8 埃的窄带双折射滤光器，一个 512×512 点阵的 CCD 照相机以及一个由计算机控制的图象接收系统组成。

1．3．2．2 工作谱线

太阳磁场望远镜可以工作在两个波段：FeI5324.19 埃和 Hβ4861.24 埃。这两个波段分别用于观测光球矢量磁场和速度场以及色球纵向磁场和速度场。当观测光球纵向磁场（Stokes 参量 V）时，观测波段设在离 FeI5324.19 埃谱线线心-0.075 埃处。当观测光球横向磁场（Stokes 参量 Q 和 U）时，观测波段设在 FeI5324.19 埃谱线线心处。当观测色球纵向磁场（Stokes 参量 V）时，观测波段设在离 Hβ4861.24 谱线线心-0.24 埃处。

1．3．2．3 工作原理

在进行磁场测量时，通过在 KD*P 晶体上分别加上正负高压，就可以分别测得圆偏振(I_-)和线偏振(I_+)强度，从而求出磁场的 Stokes 参数：

$Q,U,V=(I_- - I_+)/(I_- + I_+)$ 。

从 Q，U，V 可以求出纵向磁场分量 $B_{\parallel} = C_{\parallel} * V$

和横向磁场分量 $B_{\perp}= C_{\perp}*(Q^2 + U^2)^{1/4}$ ，$\varphi = 0.5tg^{-1}(U/Q)$ ，

其中 $C_{\parallel}$和 $C_{\perp}$分别为纵场和横场的定标系数。

1．3．2．4 谱线定标

FeI5324.19 埃谱线的理论定标是由艾国祥等在 1982 年完成的[22]。1996 年，王同江等利用太阳自转速度方法对 FeI5324.19 埃谱线和 Hβ4861.24 谱线进行了观测定标。结果可参照文献[23]。

1．3．2．5 视场和分辨率

观测时，CCD 的视场大小约为 5.23 角分×3.63 角分，南北方向 CCD 角分辨率为 0.5 角秒，东西方向 CCD 角分辨率为 0.7 角秒。观测的时间分辨率可以根据需要设定。通常采用 256 帧时，时间分辨率为 40 秒。

本论文的光球和色球磁场观测就是用此望远镜观测完成的。关于此系统更详细的情况请参考文献[21]。

1．3．3 多通道太阳望远镜

多通道太阳望远镜(图 1.3)是我国独创的、世界唯一的、能同时测量太阳上不同层次、不同尺度的视频矢量磁场、速度场，以及通过光谱扫描获得光谱线轮廓和 Stokes 参数轮廓的，高时间、高空间分辨率、高灵敏度和适当光谱分辨率的，高科学含量的综合望远镜，是目前世界上具有领先水平的最强大的综合功能的太阳望远镜系统之一。

它由五个不同功能的望远镜组成，组装于统一的带有光电导行的跟踪系统上，同时用 14 个 CCD 接收工作，后接图象、录象和计算机系统。

① 口径 60cm 的真空反射望远镜，经九通道万能双折射滤光器，形成不同层次的九个太阳像，可以获得同时的不同层次的矢量磁场，以及不同时的二维谱线轮廓和 Stokes 参数轮廓。最高光谱分辨率为 0.05 埃（λ5250 埃）。

② 35cm 的真空折射望远镜(太阳磁场望远镜)，能获得光球(λ5324 埃)和色球(λ4861 埃)的矢量磁场及视线速度场。

③ 10cm 全日面矢量磁场和视线速度场望远镜，附有带宽 0.1 埃的万能双折射滤光器。

④ 14cm 色球望远镜，有带宽 0.5 埃±32 埃可调滤光器，能获得全日面和局部区色球 Hα 单色像及色球纵向磁场。

⑤ 8cm 的 CaII λ3933 埃全日面单色像，附有带宽 2 埃的 daystar 滤光片。

关于多通道太阳望远镜的更多情况可参照文献 [24]。

1．3．4 空间太阳望远镜

空间太阳望远镜是由艾国祥院士在充分考虑了空间天文的全波段、全时段、全方位、无大气抖动、无散射光等优点的基础上而设计提出的。

空间太阳望远镜的科学目标为：在较宽的光谱范围和较连续的时间演化上，对太阳瞬变和稳定态磁流体动力学和流体力学过程，进行协同的高分辨观测，以太阳磁元结构为突破点，以实现太阳物理研究的重大进展。

空间太阳望远镜由一个 1 米直径的光学望远镜、二维实时偏振光谱仪和四个小望远镜（软 X 射线、全日面 Hα像和宽带频谱仪）组成。总重量为 2 吨。有效功率 1000 瓦。设计年限 3-5 年。

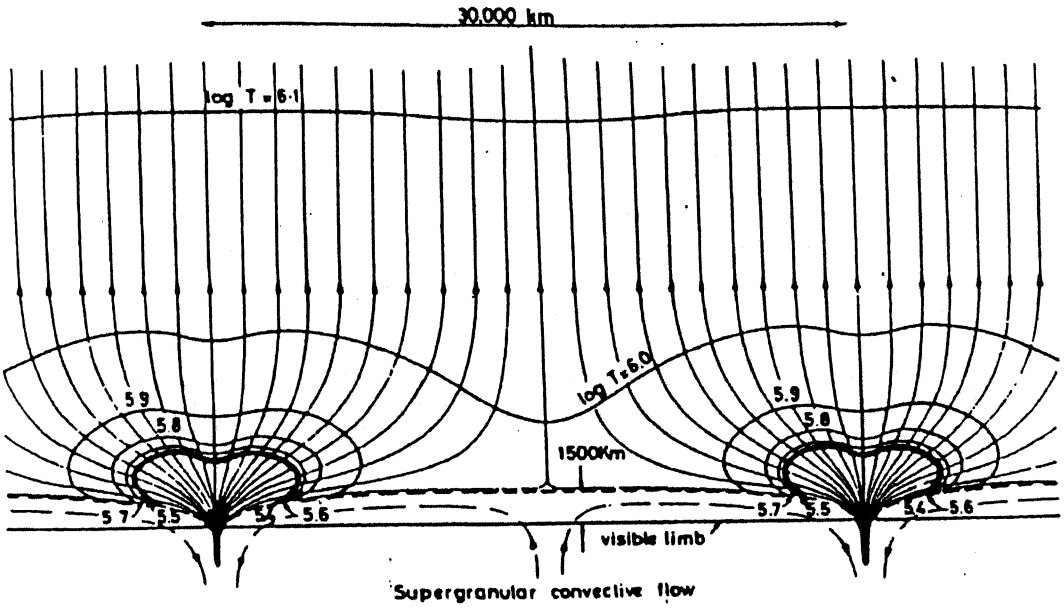
30,000 km
log T = 6·1
log T=6.0
5.9
5.8
1500Km
5.7
5.5
5.6
visible limb
Supergranular convective flow

图 1.1 伞盖模型示意图

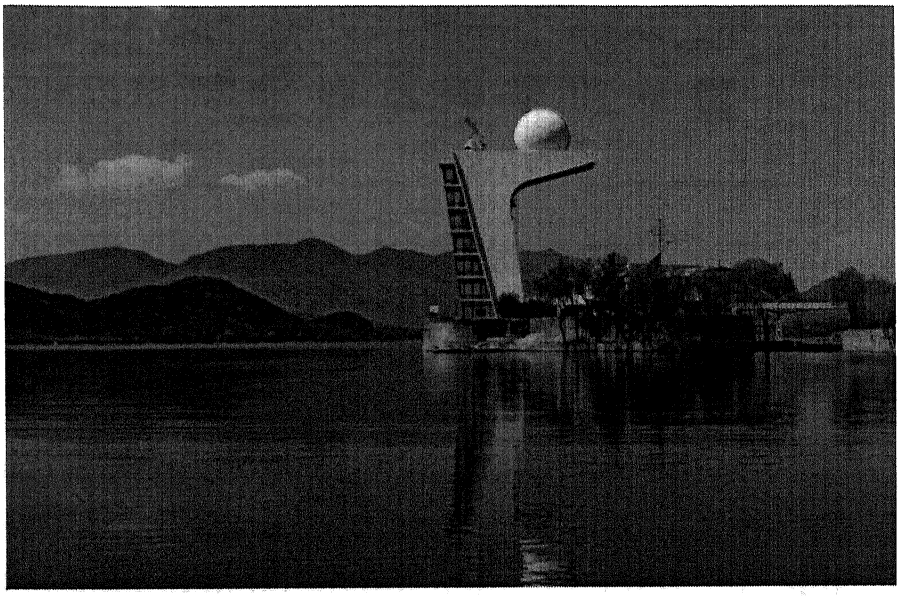

图 1.2 怀柔太阳观测站全景

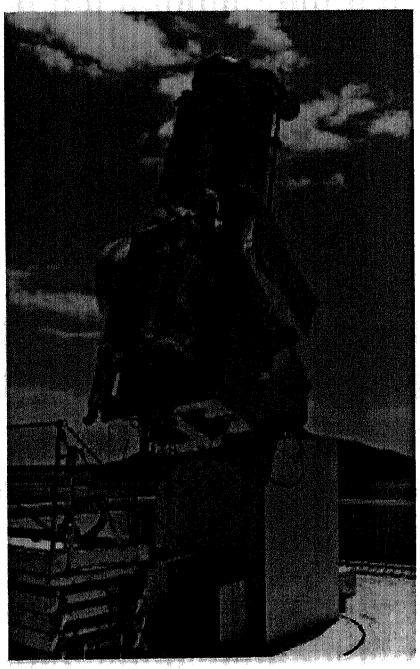

图 1.3 多通道太阳望远镜

第二章 光球宁静区磁场的观测

2．1 日面中心到边缘的光球宁静区磁场观测

2．1．1 观测的目的

如果磁流管是以伞盖模型的形式扩展的，那么它将具有较强的水平分量，从而应在日面边缘的纵向磁图上看到极性反转对。自从 Giovanelli 等人开始把在边缘观测到的极性反转对解释为伞盖模型以后，边缘极性反转对就成了伞盖模型存在的一个重要标志。Giovanelli 等就是用这种标志找到了一些认为是高度很低的伞盖的。但他们的观测都集中在活动区等较强磁场区域附近，而缺乏宁静区的观测证据。

同时，如果磁流管真是以伞盖模型的形式扩展的且具有较强的水平分量，则磁流管从日面中心到边缘应表现出一定的形态变化。因此，观测宁静区磁流管是否有从日面中心到边缘的形态变化，以及宁静区磁流管在日面边缘是否有极性反转对，对于检验伞盖模型在宁静区的适用性将是一项有意义的工作。

2．1．2 观测

1998 年 5 月 30 日，我们对从太阳日面中心到西边缘的光球磁场进行了观测。观测使用的是北京天文台怀柔观测站的太阳磁场望远镜。关于此望远镜的情况，我们在前面的 § 1.3 节中已有介绍。

我们观测了从日面中心到边缘的三个宁静区域。这三个宁静区域被标为区域 A，B 和 C，而分别显示在图 2.1 中。观测当天的日轴夹角 P_0 为-16.26°，日心经度 L_0 为 117.95°，日心纬度 B_0 为-0.92°。每个区域的视场大小约为 6′×4′。虽然我们 CCD 的分辨率为 0.7″ ×0.5″，但为了提高信躁比，我们对磁图进行了 3×4 的平滑，因而实际的空间分辨率约为 2″×2″。时间分辨率为 4 分钟。

2．1．3 观测结果与分析

图 2.2 即为我们观测到的三个区域的磁图。图 2.3 为将这三个区拼接后的磁图。拼接后的视场大小为 13.8'×3.4'。

从图 2.3 可以看出，宁静区磁元的形态从中心到边缘变化很小，且在边缘处大部分磁元没有表现出极性反转对结构。这说明宁静区磁流管并没有较强的水平分量，也没有形成在活动区附近发现的伞盖结构。

在此次观测中，在宁静太阳的西边缘，只发现了一对类似极性反转对的结构。在图 2.3 中以α和β标出。但是，即使是这为数不多的一对，是否真为极性反转对，也存在着问题。根据 Zirin1988[1] 书中的分析，由磁流管扩张而形成的极性反转对应比较靠近且两者的分界线应平行于日面边缘。并且，在许多观测到的可能由磁流管扩张而引起的极性反转对中，通常较靠近边缘的那个磁元磁通量密度较低（见 Zirin 书[1] 中图 6.12 以及此章的图 2.4 中的 a 和 b）。可是，在这一对磁元中，较靠近边缘的β磁元的磁通量密度为 28 高斯，而α磁元的磁通量密度为 17 高斯。各种情况都使得这对磁元看起来更像是两个靠的较近的极性相反的孤立磁元，就像在混合极性的宁静区中常看到的那些，而不像是一个由磁流管扩张而形成的极性反转对。

2．2 太阳赤道与南北极的磁场结构

2．1．1 研究的目的

通过以上的观测，我们发现，在日面边缘的宁静区没有多少极性反转对。而研究极区磁场的邓元勇博士却发现，极区磁图中可以看见许多极性反转对。为此，我们把以往怀柔观测中在同一天内对太阳四个极（南极、北极、东边缘、西边缘）都有光球磁场观测的资料搜集了来进行研究。

2．1．2 观测结果与分析

我们一共收集了 15 天的资料。通过分析这些资料，我们发现：太阳南北两极与赤道边缘（东、西边缘）存在着不同的磁场结构。具体地说，在

赤道边缘的宁静区中，很少能发现极性反转对的存在，而在南北两极则总能发现为数不少的极性反转对。如图 2.4 即为 1993 年 7 月 11 日拍摄的四个极区的磁图。图 a 为太阳北极的磁图。图 b 为太阳南极的磁图。图 c 为日面东边缘的磁图。图 d 为日面西边缘的磁图。每幅图的视场大小约为 6'×4'。空间分辨率为 2″×2″。时间分辨率为 4 分钟。从图 a 和 b 可以看到明显的极性反转对，而从图 c 和 d 则很难看到极性反转对。

这种现象首先说明，太阳磁场的空间结构可能存在着多样性。即使同样是小磁流管，在赤道附近和在南北两极也表现出不同的性质。赤道边缘与南北极磁场在其他方面也表现出一些不同性质[2-3]。其次，这种现象可能预示着小尺度磁流管的空间结构可能受太阳整体磁场的影响，从而与小尺度磁流管在日面的位置有关，甚至可能随太阳活动周变化。最后，这种现象至少说明小尺度磁流管在南北极比在赤道附近有更强的水平分量，从而有可能形成较大一些的伞盖。

关于这一方面的更详细的讨论，可参考附录二中的"Different magnetic features between solar polar and equatorial magnetic fields"一文。

2．3 整个日面边缘的光球磁场观测

为了进一步检验我们对太阳赤道与南北极磁场结构不同的分析，我们对整个日面边缘的光球磁场进行了观测。

观测是在 1998 年 10 月 3 日进行的。观测从太阳北极开始，以顺时针方向进行，然后以回到北极为结束。此次观测共测了 26 个区。对每个区，我们分别测了 4 幅 2 分钟积分的磁图。处理时将每个区的 4 幅磁图对齐后叠加，以得到高信躁比的磁图。

如图 2.5 即为叠加后对应于 26 个观测区的 26 幅磁图。从这些磁图中可以看出，太阳磁场南北极确实存在着不同于其他边缘处的磁场结构。在南北极（图 2.5 中 a 和 n）可以看到明显的极性反转对结构，而在其他边缘处则很难看到（活动区附近除外）。通过这些磁图，确定极性反转对出现和消失的纬度将是一项十分有意义的工作。

2．4 总结

通过对日面中心到边缘及整个日面边缘的光球磁场观测，我们发现：

1．宁静区磁元的形态从中心到边缘变化很小，且在边缘处大部分磁元没有表现出极性反转对结构。这说明宁静区磁流管并没有较强的水平分量，也没有形成在活动区附近发现的伞盖结构。

2．太阳南北两极与赤道边缘（东、西边缘）存在着不同的磁场结构。在赤道边缘的宁静区中，很少能发现极性反转对的存在，而在南北两极则总能发现为数不少的极性反转对。

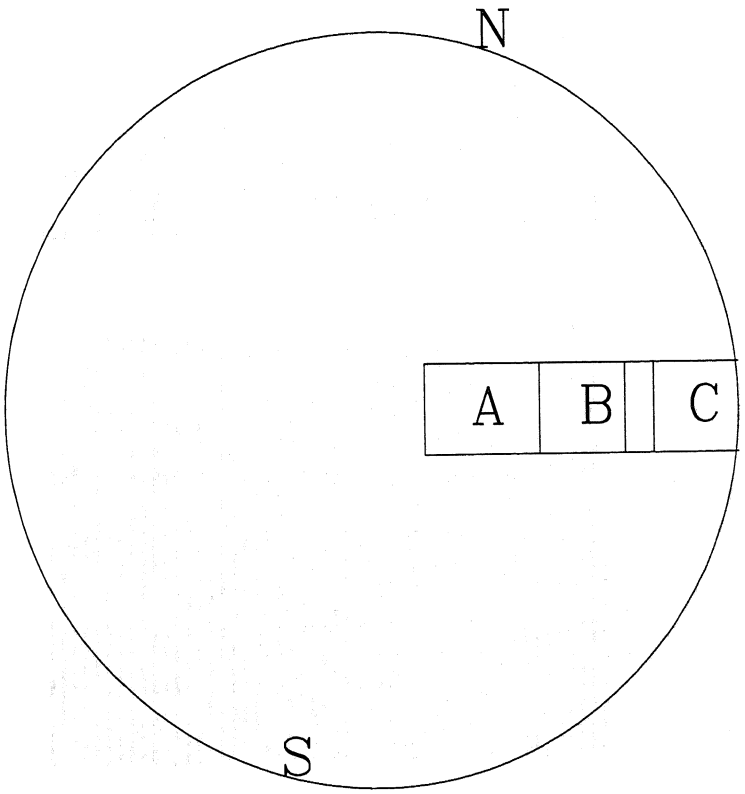

Fig.2.1 Solar disk positions of the fields observed on May 30 1998.

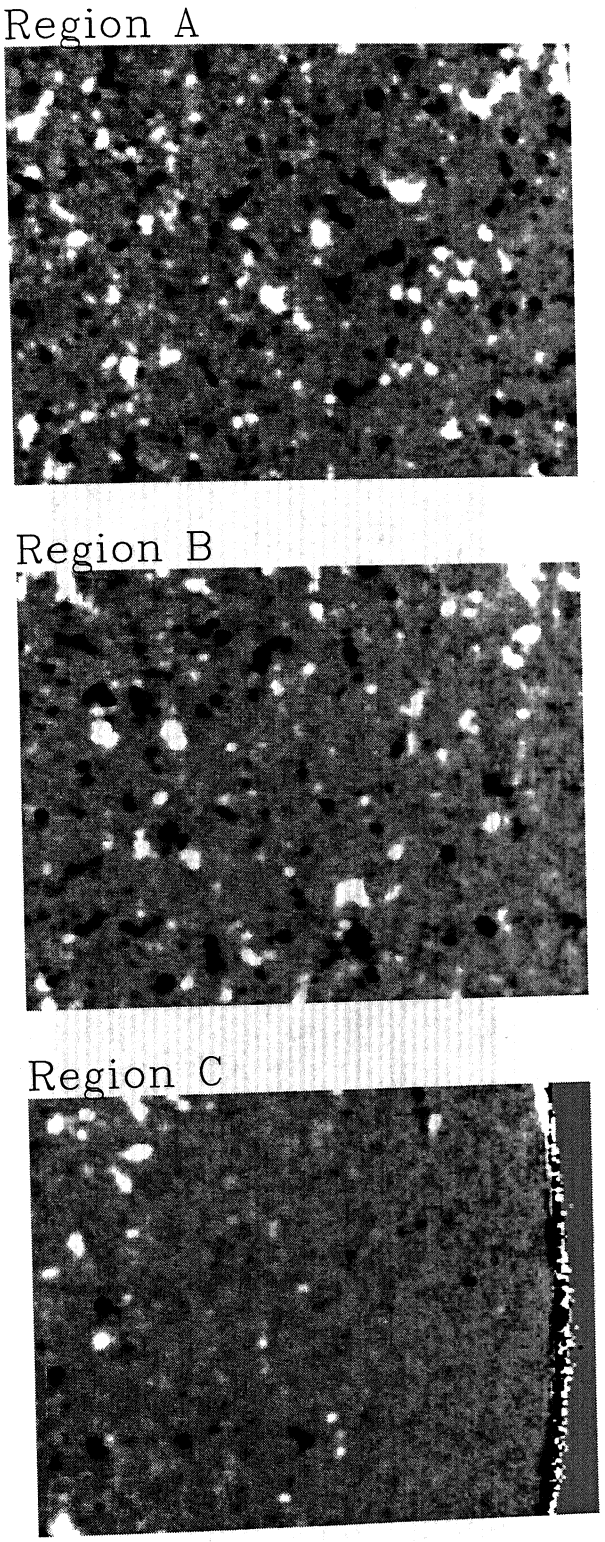

Fig.2.2 Photospheric magnetograms observed on 30 May 1998. Each field of view is 5.2′*3.6′. Bright (dark) structures correspond to positive (negative) polarities.

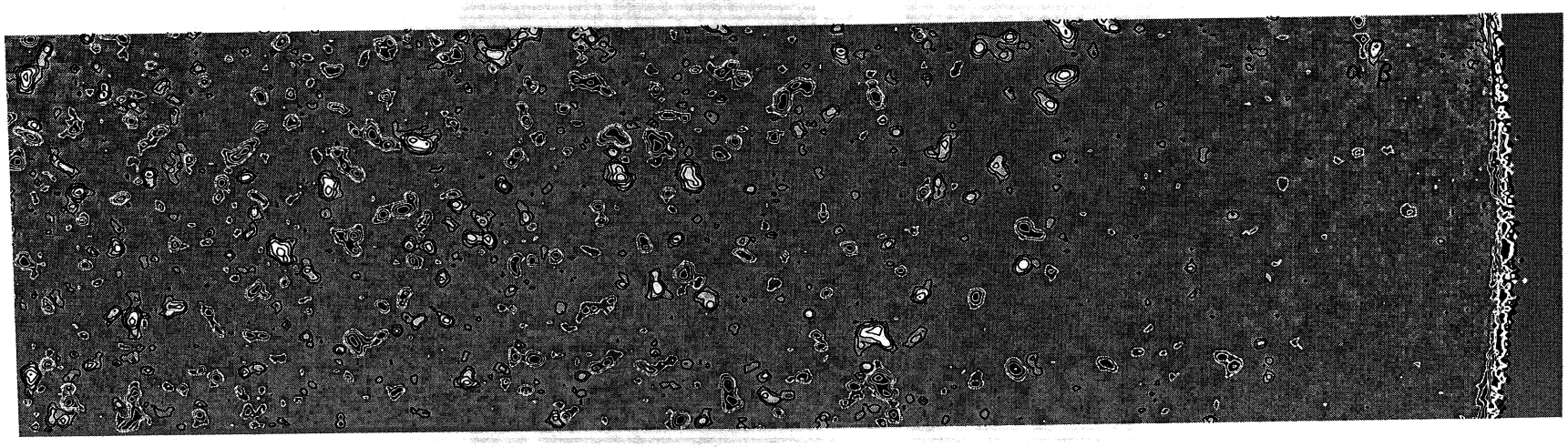

Fig.2.3 Photospheric mosaic magnetogram observed on 30 May 1998. The size of the mosaic field is 13.8'*3.4'. Bright (dark) structures correspond to positive (negative) polarities. Black (white) contours correspond to positive (negative) fields of 10, 20, 40, 80, 160 Guass.

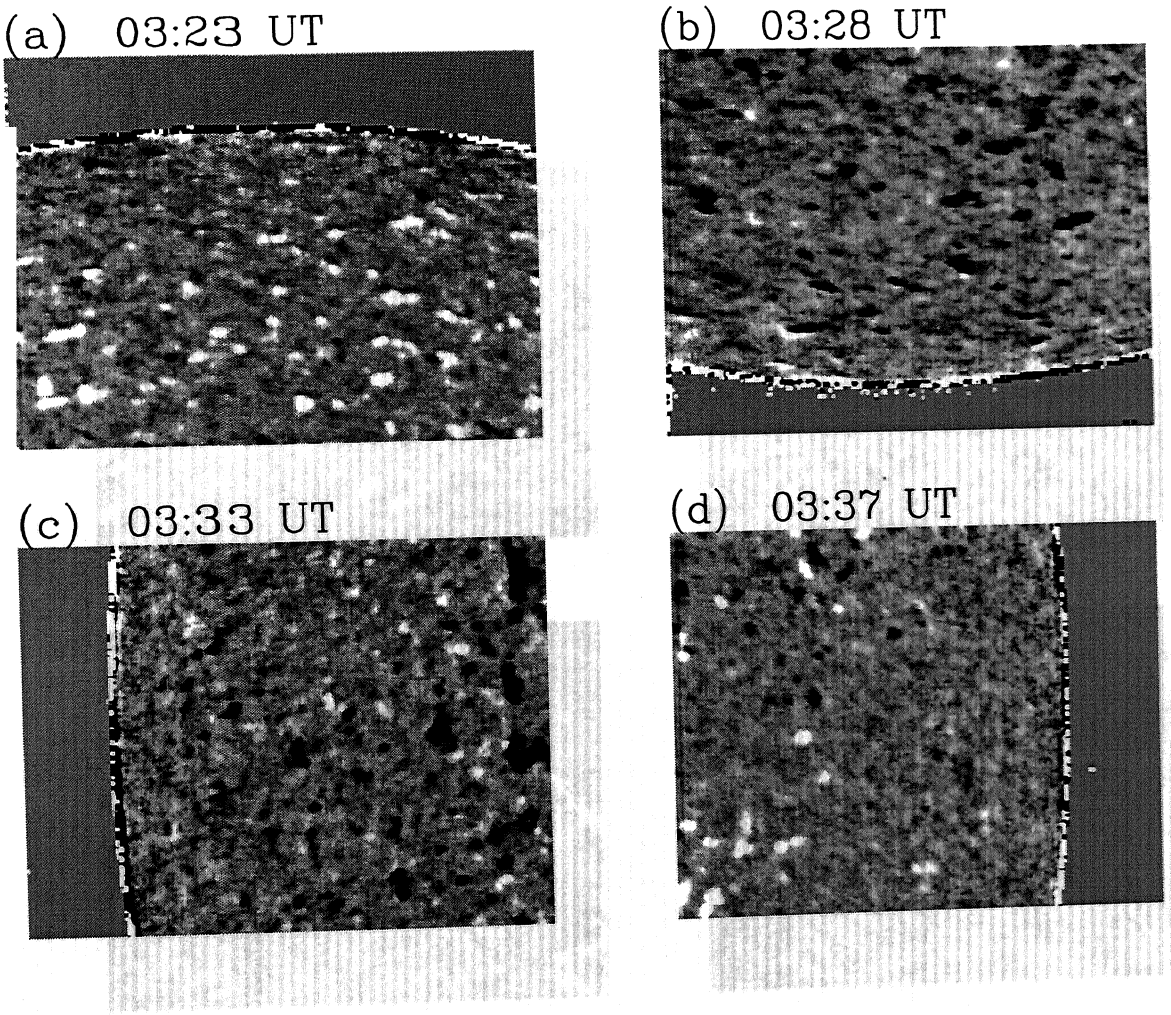

Fig.2.4 Longitudinal photospheric magnetograms near solar poles (a: north pole; b: south pole) and equatorial limbs (c:east limb; d:west limb) observed on 11 July 1993. Each field of view is 5.6′*3.6′. Bright (dark) structures correspond to positive (negative) polarities.

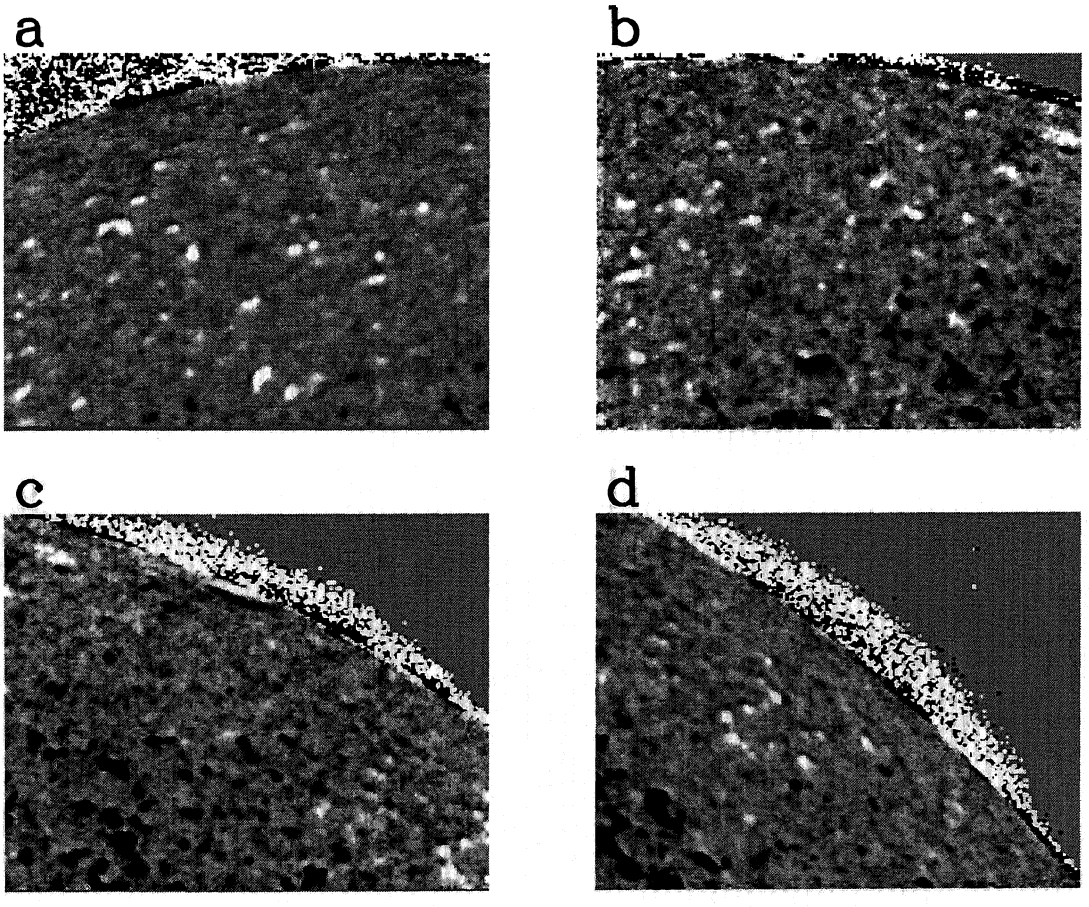

Fig.2.5 Photospheric limb observations on 3 October 1998. The observation is from solar north pole to west limb, south pole, east limb and then back to north pole. Each field of view is 5.2′*3.2′.

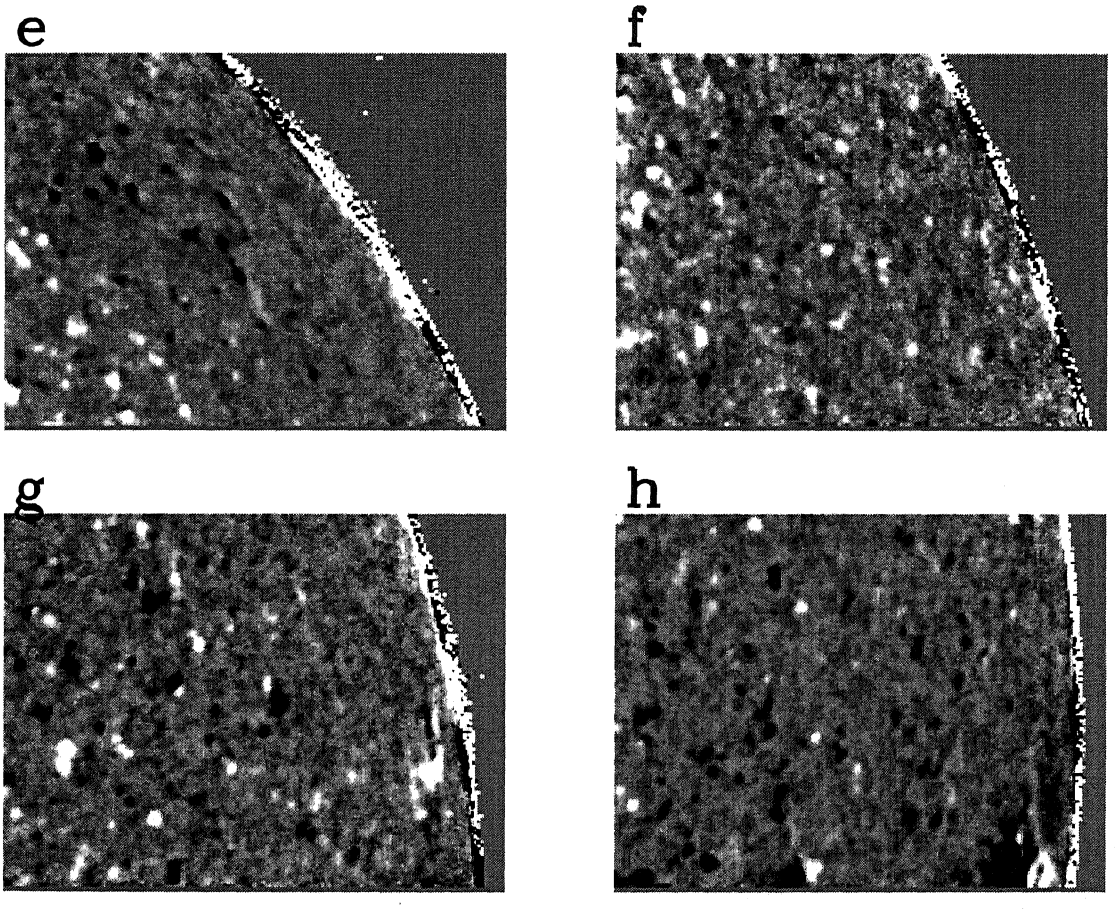

Fig.2.5 continued.

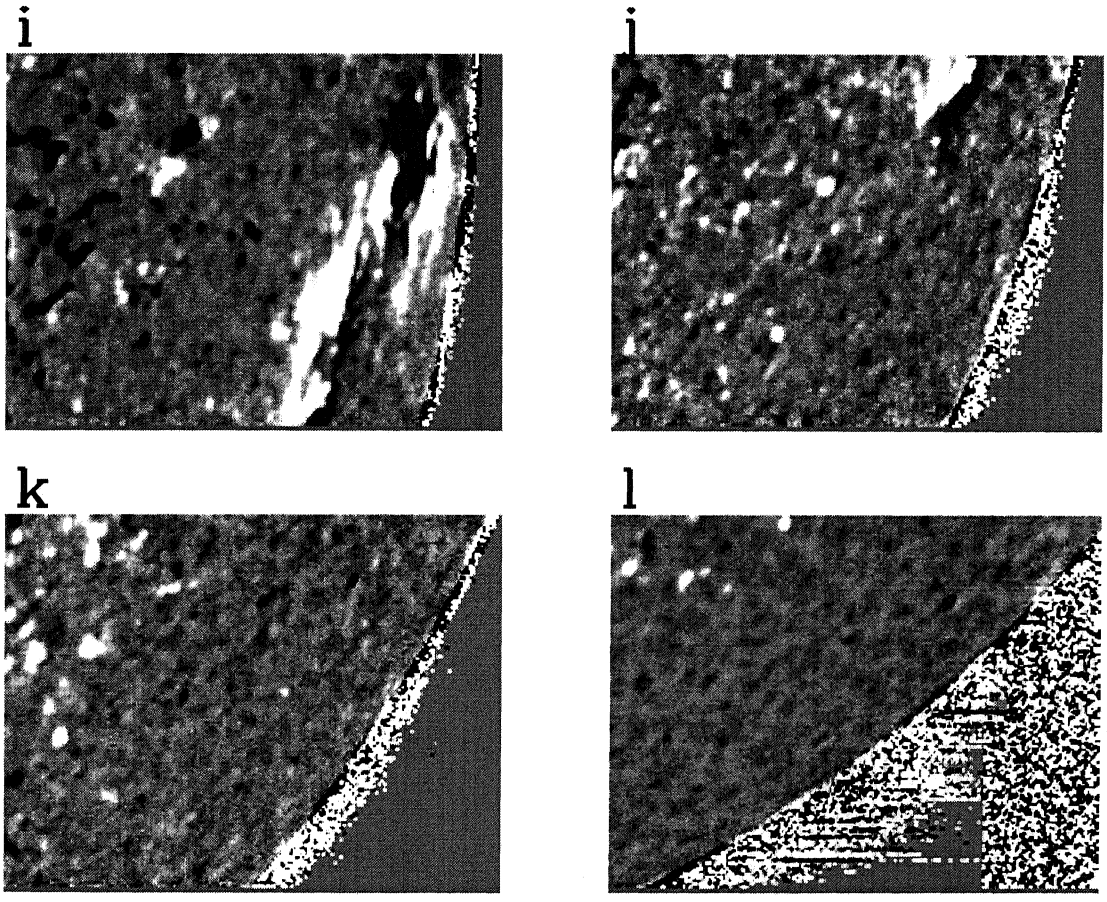

Fig.2.5 continued.

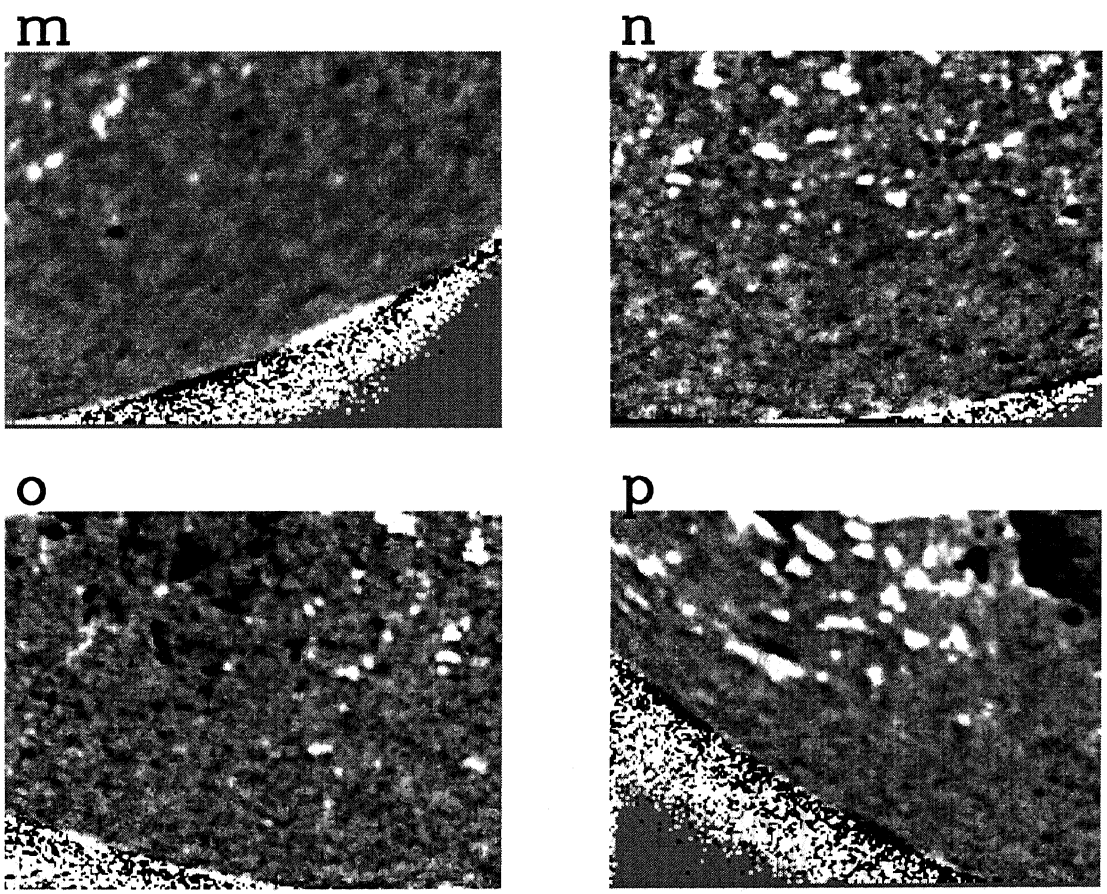

Fig.2.5 continued.

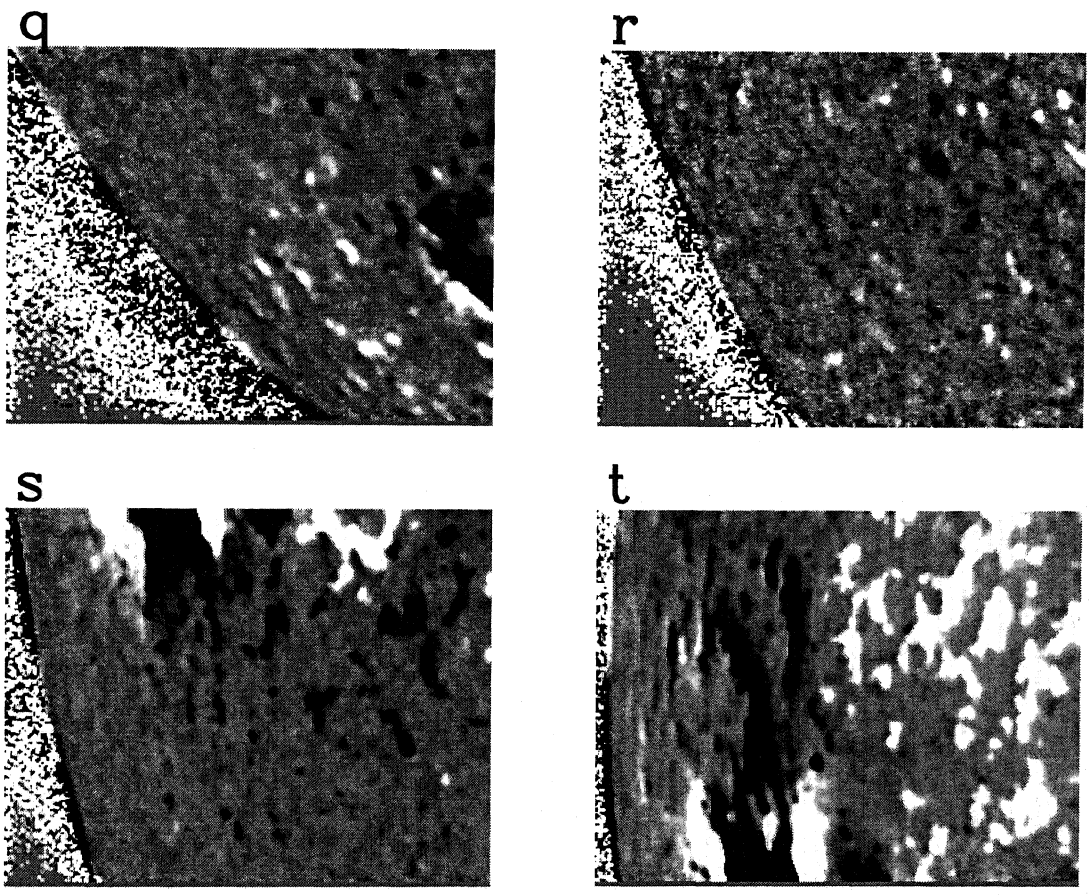

Fig.2.5 continued.

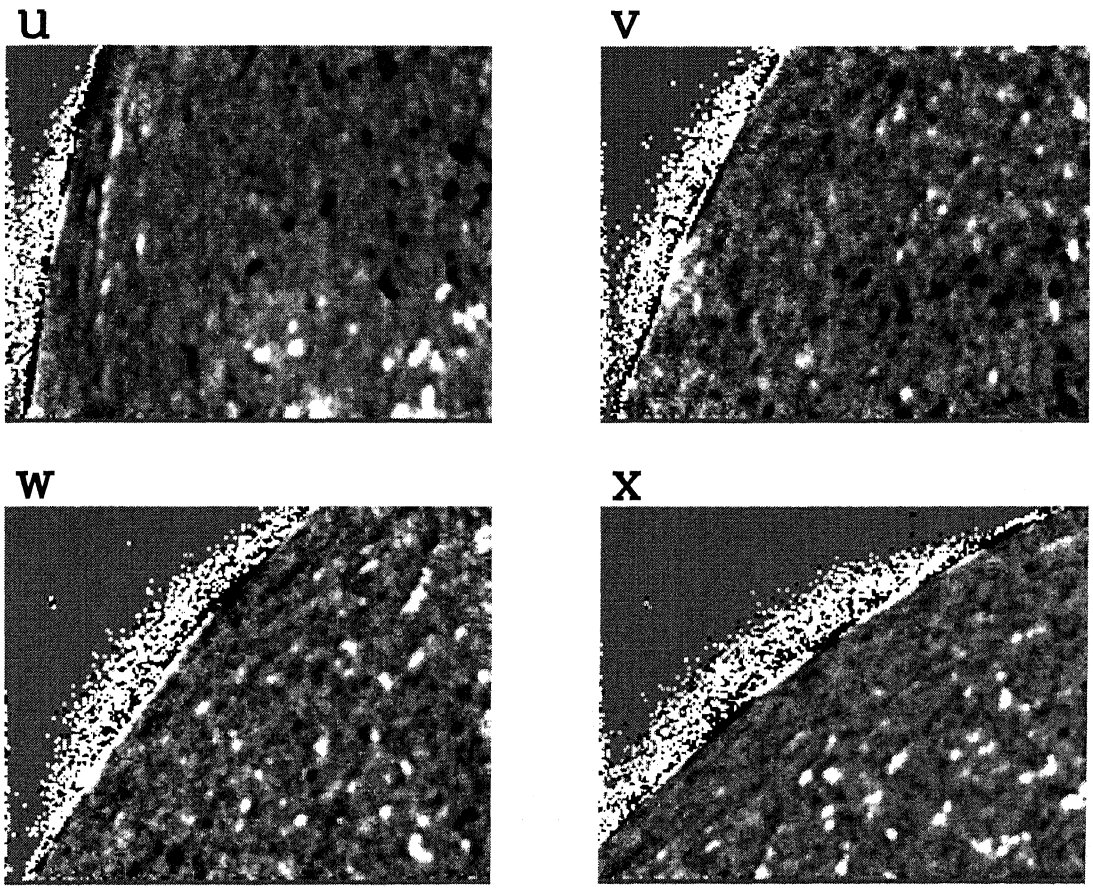

Fig.2.5 continued.

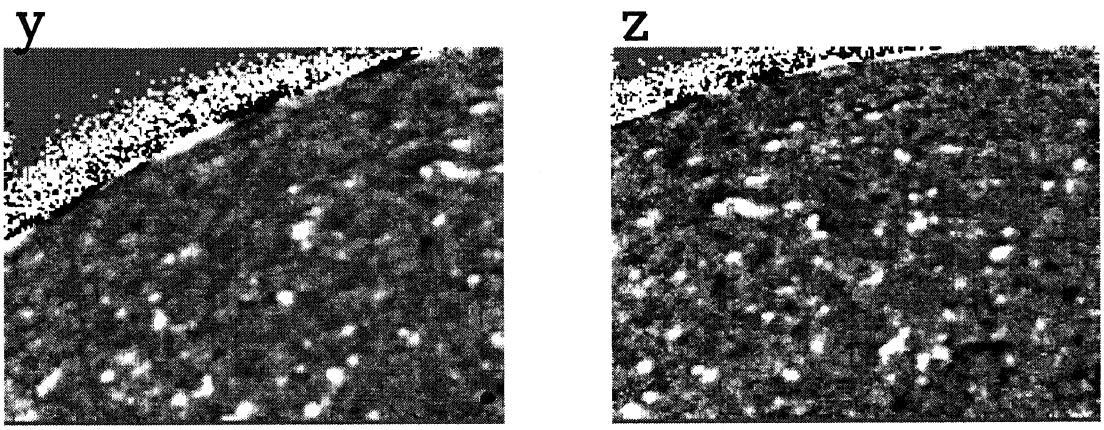

Fig.2.5 continued.

第三章 色球宁静区磁场的深积分观测

3．1 测量的目的和意义

从第一章的介绍可以看到，对于伞盖模型，理论和观测的探讨一直存在着分歧。如何解决和解释这种分歧，就成为当前急需解决的问题。我们注意到，以往的观测通常集中在太阳活动区或增强网络区域，而理论模型往往都是从宁静区磁流管物理条件推出的。因此，为了直接检验从宁静区磁流管物理条件推出的理论模型是否正确，直接观测宁静区的磁流管的空间结构就显得十分必要。

在第二章中，我们介绍了对太阳宁静区光球磁场的一些观测结果，发现在宁静区没有形成如活动区附近那样的伞盖结构。在此章中，我们将介绍利用 H_β谱线对色球宁静区磁场的测量，并对色球磁场观测结果与光球磁场观测结果进行了比较分析。

3．2 色球宁静区磁场测量的难度与我们的处理方法

测量色球宁静区磁场存在着较大的难度。主要原因是形成在太阳色球的谱线（如 H_α，H_β，CaK 和 CaH 线）较宽，对磁场的敏感程度较弱。例如，H_β谱线形成于色球，但谱线较宽，等值宽度约为 4.2 埃，磁敏朗德因子 g 约为 1。而与之对应的形成于光球的谱线，如 Fe5324 谱线，其谱线等值宽度只有 0.3 埃，磁敏朗德因子 g 约为 1.5。这使得多数用于太阳色球磁场观测的磁像仪获得的资料的躁声水平远高于获得的光球磁场资料的躁声水平，从而难于分辨太阳色球磁场的精细结构尤其是色球宁静区的磁场结构。

如图 3.1 即为一张日面中心宁静区的光球磁图（图 a）和一张同一视场的色球磁图（图 b)。两张磁图的积分时间是相同的。但从图中可以看出，色球磁图的躁声水平远高于光球磁图（光球磁图的躁声约为 4 高斯，色球磁图的躁声约为 20 高斯)。从光球磁图上，可以看到宁静区中的网络结构与内网络结构，而在色球磁图上，则看不到内网络结构，网络结构也只能看到较强的几个。

因此，为了获得高信躁比的太阳色球宁静区磁图，我们在世界上首次采用了超深积分磁场观测方法。所谓深积分，就是将多幅短时间积分的磁图进行位置相关后叠加而得到高信躁比的磁图。这是一种被天文学家广泛采用的处理弱光的方法。但以往人们观测太阳磁场时，最多只积分几分钟的时间。而我们突破以往的局限，对太阳宁静区磁场进行了长达几小时的积分观测，即所谓的超深积分观测。当然，这样的超深积分观测会使我们观测不到一些几小时内的磁场演化细节。但另一方面，这种观测却使我们突破以往只能进行太阳活动区（即信号较强区域）色球磁场观测的限制，使我们在世界上首次观测到了高信躁比的太阳色球层上随时间变化较慢的宁静区磁元的精细结构。更详细的讨论可参考附录二的“A comparison between photospheric and chromospheric quiet-Sun magnetograms”一文。

3．3 观测与数据处理

1998 年 4 月 14 日和 9 月 15 日，我们对日面中心的宁静区分别进行了超深积分的光球和色球磁场观测。1998 年 5 月 30 日，我们对日面中心到西边缘的宁静区进行了超深积分的光球和色球磁场观测。我们使用的是北京天文台怀柔观测站的太阳磁场望远镜。关于仪器的性能可参考本论文的第一章第三节。

3．3．1 日面中心观测

1998 年 4 月 14 日，我们对日面中心进行了一系列的光球和色球磁场观测。观测光球磁场时，磁像仪的波段设在离 Fe5324 谱线线心-0.075 埃处。观测色球磁场时，磁像仪的波段设在离 H_β谱线线心-0.24 埃处。在观测过程中，我们每观测一幅 4 分钟的光球磁图，随后观测 10 幅 4 分钟的色球磁图。如此循环，形成一个系列。这样使我们超深积分后的光球和色球磁图既保持了准同时性又能保持色球磁图和光球磁图的信噪比的大致相当。

图 3.2 即为我们观测到的日面中心光球（图 a）和色球（图 b）的超深积分磁图。图 a 叠加了 5 幅 4 分钟积分的磁图，因此其有效积分时间为 20 分钟。图 b 叠加了 50 幅 4 分钟积分的磁图，因此其有效积分时间为 200 分

钟。磁图的空间分辨率为 2″×2″。

1998 年 9 月 15 日，我们又对日面中心进行了系列的光球和色球磁场观测。与 4 月 14 日的观测不同的是，在观测色球磁场时，磁像仪的波段设在离 H_β谱线线心-0.16 埃处。与 4 月 14 日的观测相同，在观测过程中，我们每观测一幅 4 分钟的光球磁图，随后观测 10 幅 4 分钟的色球磁图。如此循环，形成一个系列，以使我们超深积分后的光球和色球磁图既能保持准同时性又能保持色球磁图和光球磁图的信噪比的大致相当。

图 3.3 为我们 9 月 15 日观测到的太阳日面中心光球（图 a）和色球（图 b）的超深积分磁图。图 a 叠加了 7 幅 4 分钟积分的磁图，因此其有效积分时间为 28 分钟。图 b 叠加了 70 幅 4 分钟积分的磁图，因此其有效积分时间为 280 分钟。磁图的空间分辨率为 2″×2″。积分后的光球磁图的躁声为 2 高斯，色球磁图的躁声为 5 高斯。

3．3．2 中心到边缘观测

1998 年 5 月 30 日，我们对从太阳日面中心到西边缘的三个区域进行了系列的光球和色球磁场观测。观测的区域位置见图 2.1。对于每一个区，我们先观测一幅 4 分钟的光球磁图，随后观测 20 幅 4 分钟的色球磁图，然后再观测一幅 4 分钟的光球磁图。

图 3.4 为我们观测到的区域 A 的光球（图 3a）和色球（图 3b）的超深积分磁图。图 a 叠加了 2 幅 4 分钟积分的磁图，因此其有效积分时间为 8 分钟。图 b 叠加了 20 幅 4 分钟积分的磁图，因此其有效积分时间为 80 分钟。磁图的空间分辨率为 2″×2″。 图 3.5 和 3.6 分别为观测到的区域 B 和区域 C 的光球(图 a)和色球(图 b)的超深积分磁图。积分时间和分辨率与图 3.4 中的相同。

3．3．3 定标

对光球磁场的定标，我们采用的是艾国祥等[1]1982 年理论定标的结果。对于色球磁场的定标，我们采用了使日面中心对应磁元的光球和色球磁通量相等的方法来定标。值得指出的是，用这两种方法定标的结果都与王同江博士[2]1996 年对 Fe5324 和 H_β谱线进行观测定标的结果一致。

3．4 结果分析与讨论

3．4．1 色球层上观测到的最小磁元

从图 3.2 上我们可以看到，一些出现在光球磁图上的内网络磁元也出现在色球磁图上。此处我们采用汪景秀等[3]1995 年对网络磁元和内网络磁元的定义，即认为网络磁元是那些磁通量密度大于 40 高斯的宁静区磁元，而内网络磁元是那些磁通量密度小于 40 高斯的宁静区磁元。

根据一些理论模型的计算[4-5]，内网络磁元将不能升到太阳高层大气，因此，在色球层上寻找内网络磁元将对检验这种模型具有意义。

图 3.2 中的磁元 A、B、C 和 D 就是四个同时出现在光球和色球磁图上的可能内网络磁元。在光球磁图上，磁元 A 和 B 的磁通量密度分别为 23 和 14 高斯，磁通量分别为 5.2×10^{18}Mx 和 2.0×10^{18}Mx。磁元 C 和 D 在光球磁图上的磁通量密度分别为 9 和 8 高斯，磁通量分别为 6.6×10^{17}Mx 和 5.1×10^{17}Mx。

应当指出的是，对内网络磁元磁通量密度的测量受诸多因素的影响，以下因素可能使我们将一些网络磁元划分为内网络磁元：1、磁场测量和定标的准确性无疑将影响那些磁通量密度在 40 高斯附近的磁元的划分。2、由于内网络磁元在光球表面上运动的速度比网络磁元大[6]，因此我们长时间积分的效果无疑将使一些内网络磁元看起来比实际的大。长时间积分还可能会将一些网络磁元平滑到低磁通量密度而被划分为内网络磁元，磁元 A 和 B 就有可能属于这种情况。虽然磁元 A 和 B 的磁通量密度都小于 40 高斯，但它们的磁通量大小都落在网络磁元磁通量大小的范围内[3]。

但同时一些因素又可能使我们低估了在色球磁图上观测到的最小磁通量的值：1、我们此处观测到的内网络磁元都是那些寿命相对长的内网络磁元。我们可能错过了许多寿命相对较短的内网络磁元，而这些磁元正好是那些磁通量较小的磁元[7]。2、虽然我们已经努力降低了色球磁图的躁声水平，但色球磁图的躁声水平仍然比光球磁图高，从而可能使一些低磁通量密度的磁元没有被观测到。3、由于长时间积分降低了空间分辨率，使得积分磁图上的一个内网络磁元有可能是由几个内网络磁元组成的，从而使实际每个内网络磁元的磁通量比观测的小。如磁元 A 和 B 就可能属于这种情

况，它们可能是由几个内网络磁元组成的，而每个内网络磁元的磁通量都小到落在内网络磁元磁通量大小的范围[3]。

对色球磁场进一步的高时间分辨率、高空间分辨率以及低躁声水平的测量无疑将是十分必要的。

3．4．2 光球磁元与色球磁元的演化

为了研究磁场的演化，我们将 1998 年 4 月 14 日的观测资料分成两组分别进行叠加。如图 3.7 即为叠加了从 02:07 UT 到 04:15 UT 期间观测的深积分光球（7a）和色球（7b）磁图。图 3.8 为叠加了从 04:20 UT 到 06:40 UT 期间观测的深积分光球（8a）和色球（8b）磁图。图 3.7 和图 3.8 中，积分光球磁图分别叠加了 3 幅 4 分钟积分的光球磁图，积分色球磁图分别叠加了 30 幅 4 分钟积分的色球磁图。

通过比较图 7a 和图 8a，我们可以发现一些光球层上的磁场演化。A1、A2、A3、A4 和 A5 为一些光球层上的磁对消特征，在图 7a 上出现的极性相反的磁元在图 8a 上消失或减弱了。B1 和 B2 反映了磁合并的特征，在图 8a 上出现了一些在图 7a 中没有的磁元。C1 和 C2 则反映出一些磁元的磁通量密度变化，在图 8a 中磁元变的比在图 7a 中更强。在 C3 处，一个磁元分成了两个磁元。在 C4 处，两个磁元合成了一个磁元。

以上这些光球层上的磁场变化都是已知的光球层上的磁场演化特征，但值得注意的是，我们在色球磁图上也发现了与光球磁图一一对应的演化特征。这种结果暗示着，色球上的磁对消率可能与光球上的相当。如果色球层上小尺度磁元有相当高的磁对消率，而且如果这种磁对消被认为是一种磁重联，则这将意味着宁静区的小尺度磁重联将对色球及日冕加热起着一定的作用。目前，小尺度磁场对日冕加热的贡献已越来越受到太阳物理学家们的重视[8]。

3．4．3 磁元从光球到色球的扩展程度

从图 3.2 可以看出，太阳宁静区光球和色球的磁结构非常相似。磁流管从光球到色球似乎并没有扩展多少。为了进一步证实这一点，我们选择了磁图中光球和色球磁元对中较强的 37 对，将它们归一化的磁通量密度轮

廓显示在图 3.9 中。从图 3.9 可以看出，光球磁元和色球磁元的磁通量密度轮廓十分相似。我们计算了这 37 对磁元从磁元中心扩展到磁场强度为磁元中心磁场强度一半时的宽度（定义为半强宽）。在计算中，我们假设了磁元的轮廓是接近球对称的。这样的假设当然会带来一定的误差，但在统计意义上却是可靠的。计算表明，光球磁元和色球磁元的半强宽的中位数都位于 2.5"。我们还计算了每对磁元的光球半强宽与色球半强宽的比值，这些比值显示在图 3.10 中。这些比值位于 0.84 到 1.10 之间，中位值为 0.96。

从图 3.3 可以看到同样的太阳宁静区光球和色球的相似磁结构。我们选择了磁图 3.3 中光球和色球磁元对中较强的 23 对，将它们归一化的磁通量密度轮廓显示在图 3.11 中。我们同样计算了这 23 对磁元从磁元中心扩展到磁场强度为磁元中心磁场强度一半时的宽度（半强宽）。计算表明，光球磁元的半强宽从 2.2"到 2.9"，中位数位于 2.6"。色球磁元的半强宽从 2.3"到 3.6"，中位数位于 2.8"。每对磁元的光球半强宽与色球半强宽的比值显示在图 3.12 中。这些比值位于 0.77 到 1.04 之间，中位值为 0.89。

日面中心到边缘的光球和色球磁场也显示出相似的磁结构特征（3.4-3.6）。图 3.13 分别显示了区域 A、B 和 C 中较强磁元对的归一化磁通量密度轮廓。从图 3.13 同样可以看出，光球和色球磁元的磁通量密度轮廓相似，虽然这其中有一些比较宽的磁元和一些形状不太规则的磁元。这些磁元可能是那些形状偏离球对称的磁元或者实际上是由几个未完全分开的磁元组成的磁元。表 3.1 显示了 A、B、C 三个区中光球和色球对应磁元的半强宽值。图 3.14 显示了所有这些磁元的光球半强宽与色球半强宽的比值。这些比值位于 0.67 到 1.27 之间，中位值为 0.93。

表 3.1　A、B、C 三个区中光球和色球对应磁元的半强宽值

	区域 A		区域 B		区域 C	
	中位值	范围	中位值	范围	中位值	范围
光球	2.20	1.87-2.92	2.28	1.83-5.19	2.28	1.69-4.04
色球	2.37	1.82-3.23	2.47	1.82-4.36	2.54	1.99-3.18

从以上的半宽分析，我们可以看到，在我们的观测分辨率下，宁静磁

元从光球到色球的扩散程度不大。这说明，如果坚持伞盖模型，则磁流管只能在更小的尺度上或更高的层次上散开。

同时，从我们的分析亦可看出，在离 H_β谱线线心-0.16 埃处观测的色球磁场似乎比在离 H_β谱线线心-0.24 埃处观测的色球磁场更扩散一些。如果我们仔细比较离 H_β谱线线心不同波段处的磁图，并结合 H_β谱线形成的计算（参见第五章），将使我们有可能对不同的伞盖模型作出一些判断（参见第六章）。

3．4．4 色球层上磁元的水平分量

日面边缘的纵向磁图实际上反映了磁场的水平分量。若磁流管真的如伞盖模型预言的那样膨胀，则应在日面边缘的纵向磁图上看到极性反转对。尤其在色球层，应该看到比光球层更扩展更强的极性反转对。

然而，第二章的讨论已经发现，在光球层大多数磁元并没有呈现极性反转对现象。从图 3.6 可以看出，在色球层上同样没有观测到大量的极性反转对，这说明大多数宁静区磁元在光球和色球层都没有观测到水平分量。而仅有的一对极性反转磁元（图中α和β），与第二章的讨论类似，也有可能只是两个靠的很近的极性相反的磁元，因为他们的磁结构特征不完全符合由一个磁流管扩张而呈现的极性反转对的特征（参见 Zirin 书[15]）。

3．5 总结

通过对色球宁静区磁场的观测与分析，我们发现：

1. 一些内网络磁元升到了色球层 H_β谱线形成处。
2. 色球磁元具有与光球磁元一一对应的磁场变化。
3. 色球磁元具有与光球磁元相似的磁场结构。在现有观测分辨率下，磁元从光球到色球的扩散程度不大。
4. 日面边缘的色球纵向磁图反映出宁静磁元在色球层的水平分量亦不大。

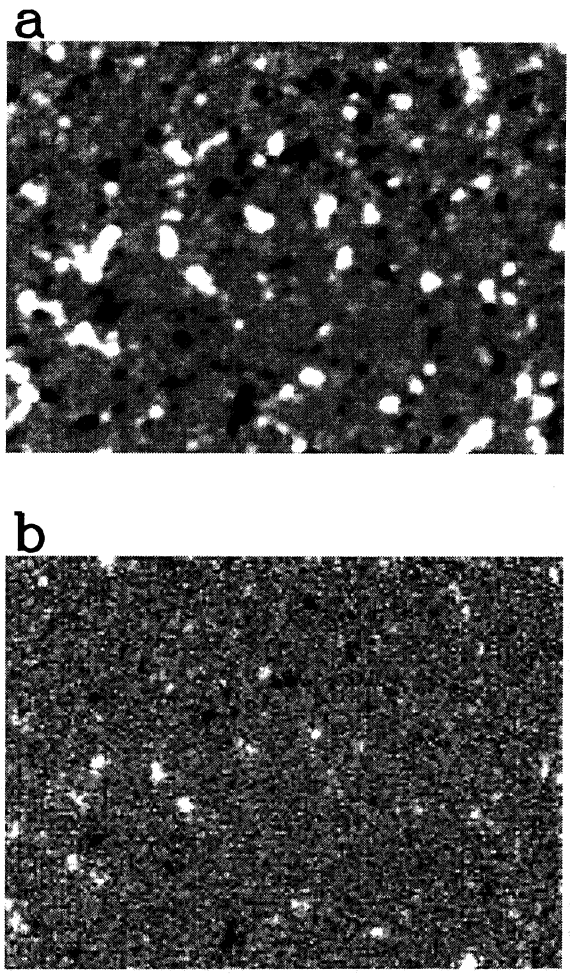

Fig.3.1 A photospheric magnetogram (a) and a chromospheric magnetogram (b) of the field observed on 14 April 1998.

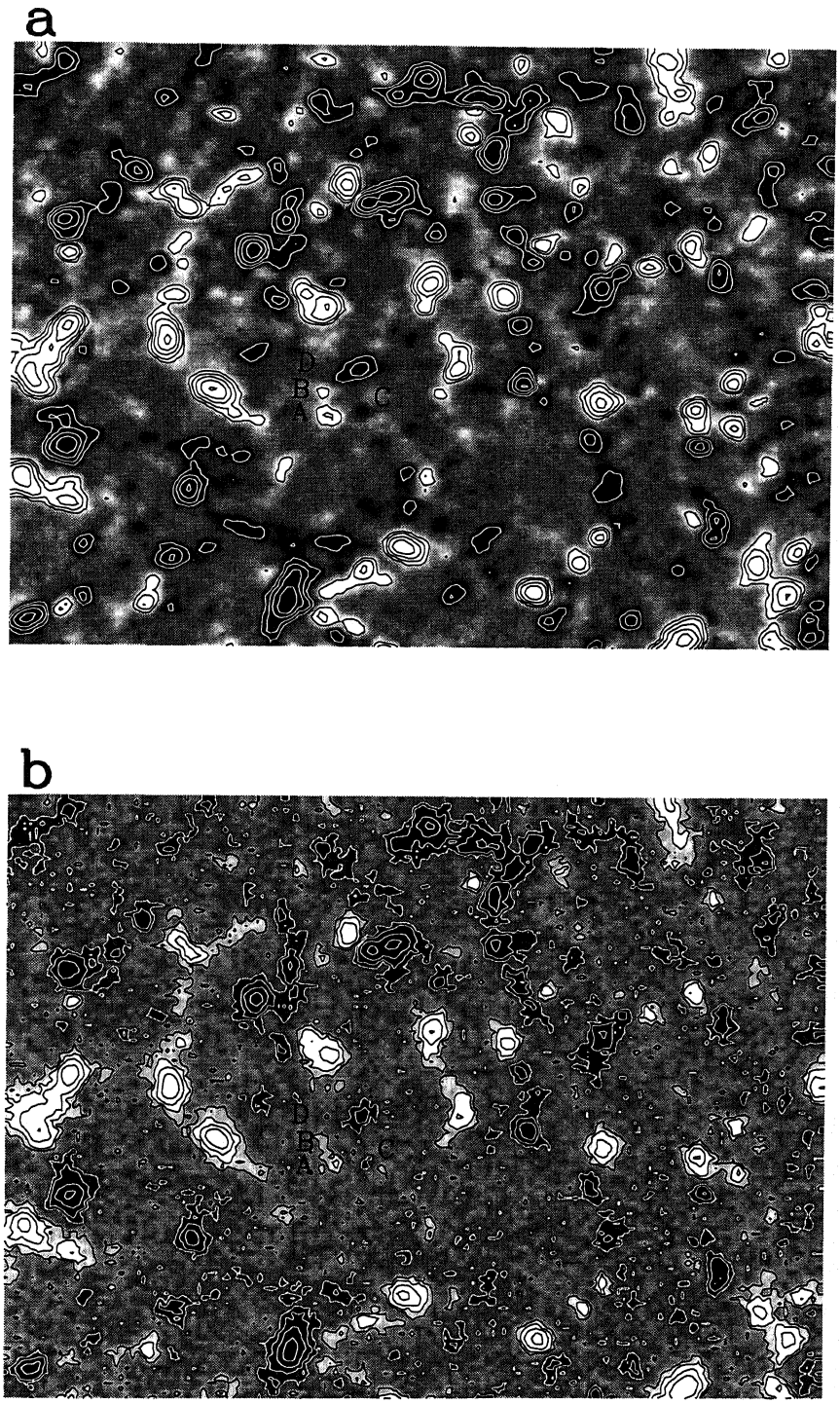

Fig.3.2. The photospheric magnetogram (a) and chromospheric magnetogram (b) in a quiet–Sun region near the disk center. The observation duration is from 02:07 to 06:00 on 14 April 1998. The field of view is 4.6'*3.4'. Bright (dark) structures correspond to positive (negative) polarities. Black (white) contours correspond to positive (negative) fields of 10, 20, 40, 80, 160 Guass.

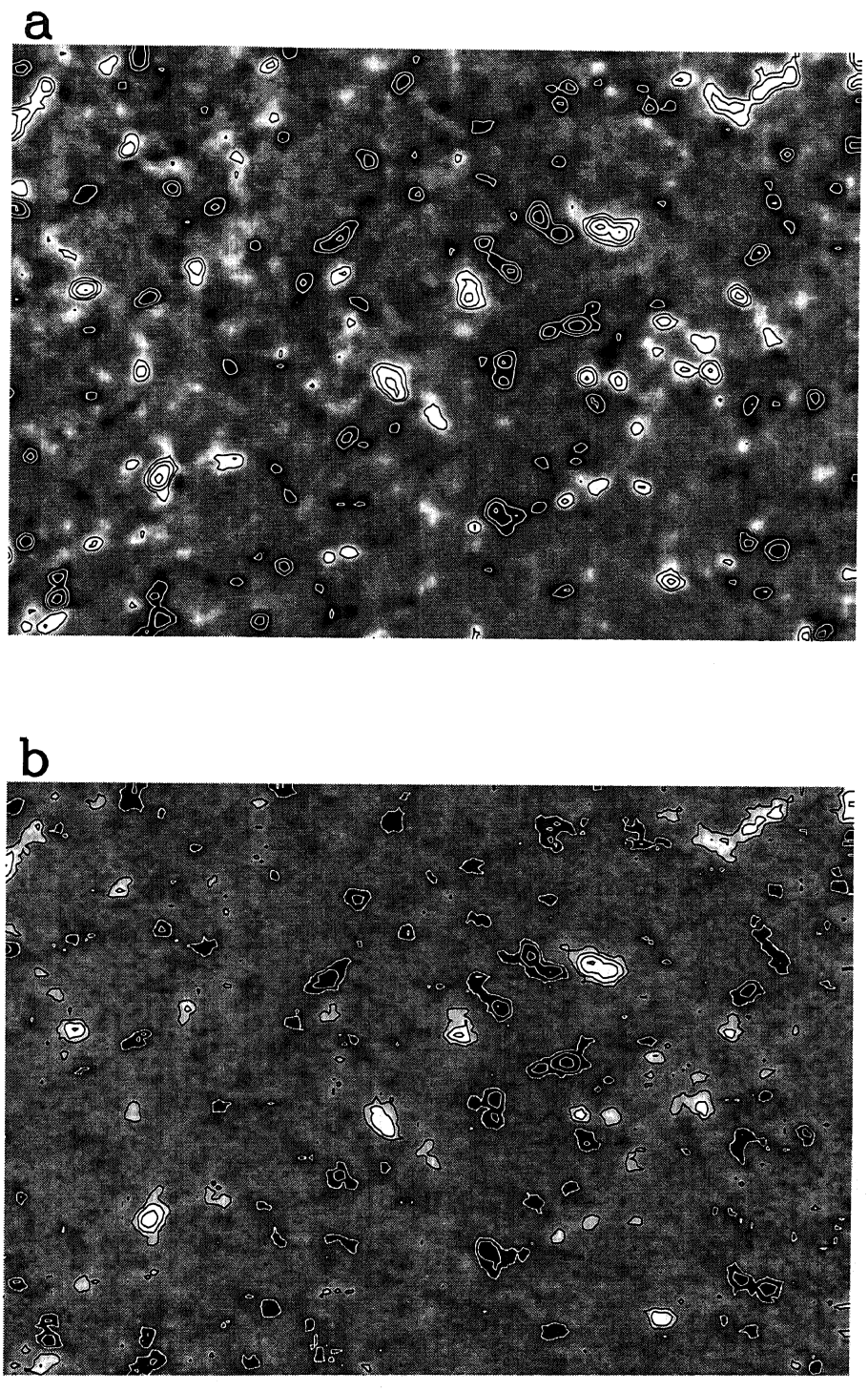

Fig.3.3 Observed integrated photospheric (a) and chromospheric (b) magnetograms of field A on 30 May 1998. The field of view is 4.9'*3.4'. Bright (dark) structures correspond to positive (negative) polarities. Black (white) contours correspond to positive (negative) fields of 20, 40, 80, 160 Guass.

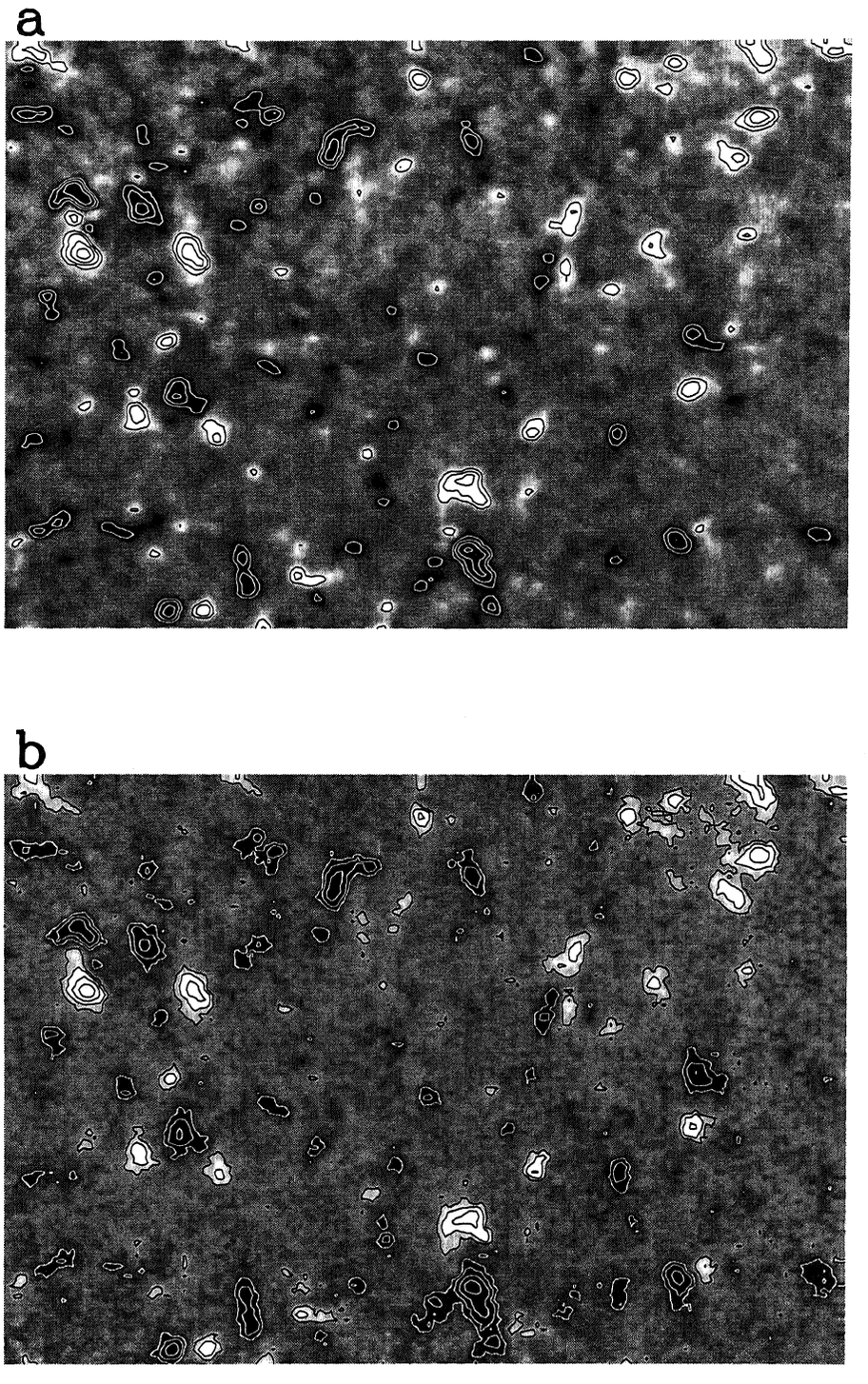

Fig.3.4 Observed integrated photospheric (a) and chromospheric (b) magnetograms of field B on 30 May 1998. The field of view is 4.9'*3.4'. Bright (dark) structures correspond to positive (negative) polarities. Black (white) contours correspond to positive (negative) fields of 20, 40, 80, 160 Guass.

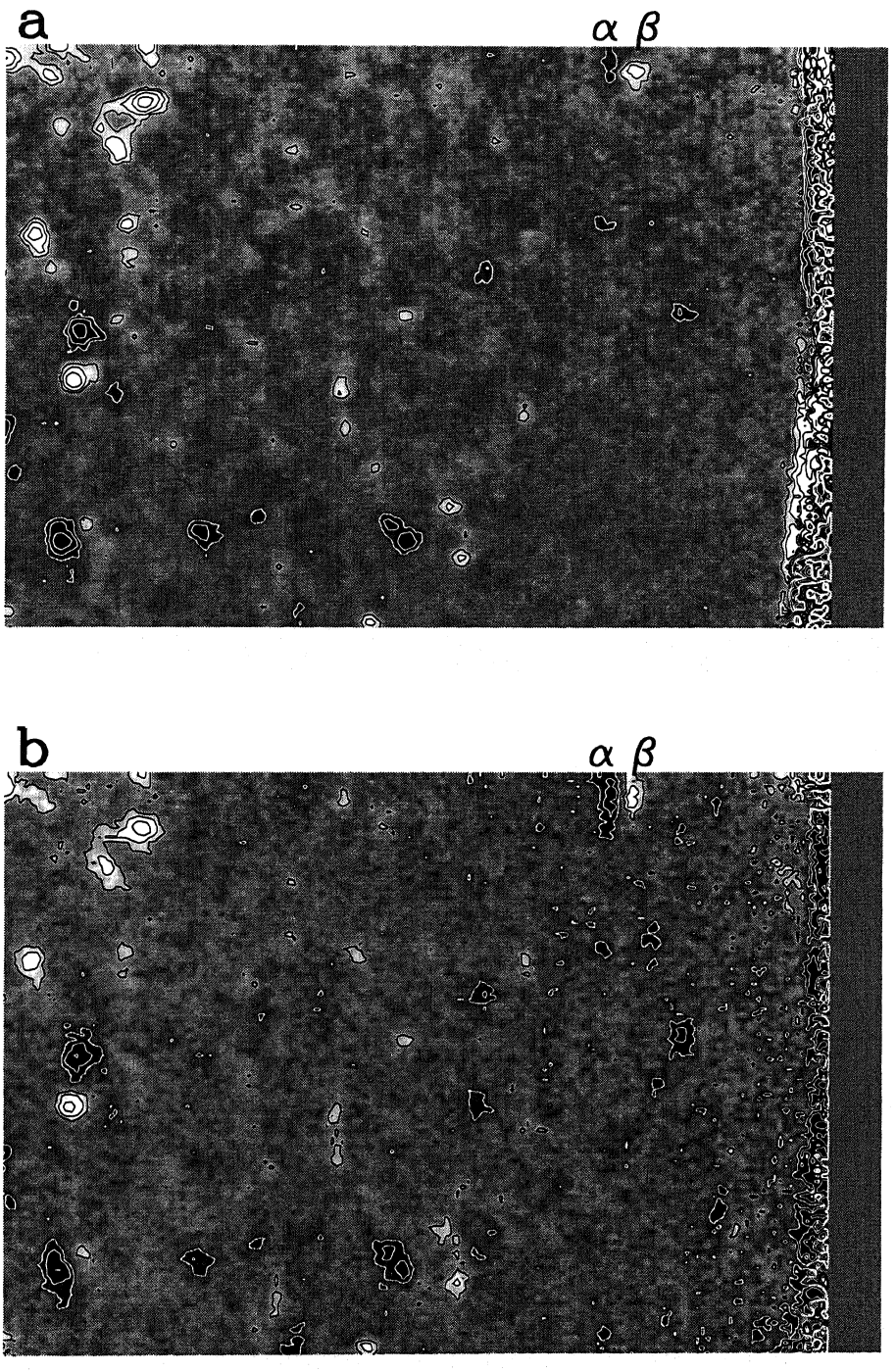

Fig.3.5 Observed integrated photospheric (a) and chromospheric (b) magnetograms of field C on 30 May 1998. The field of view is 4.9'*3.3'. Bright (dark) structures correspond to positive (negative) polarities. Black (white) contours correspond to positive (negative) fields of 10, 20, 40, 80 Guass for Figure a and 20, 40, 80, 160 for Figure b.

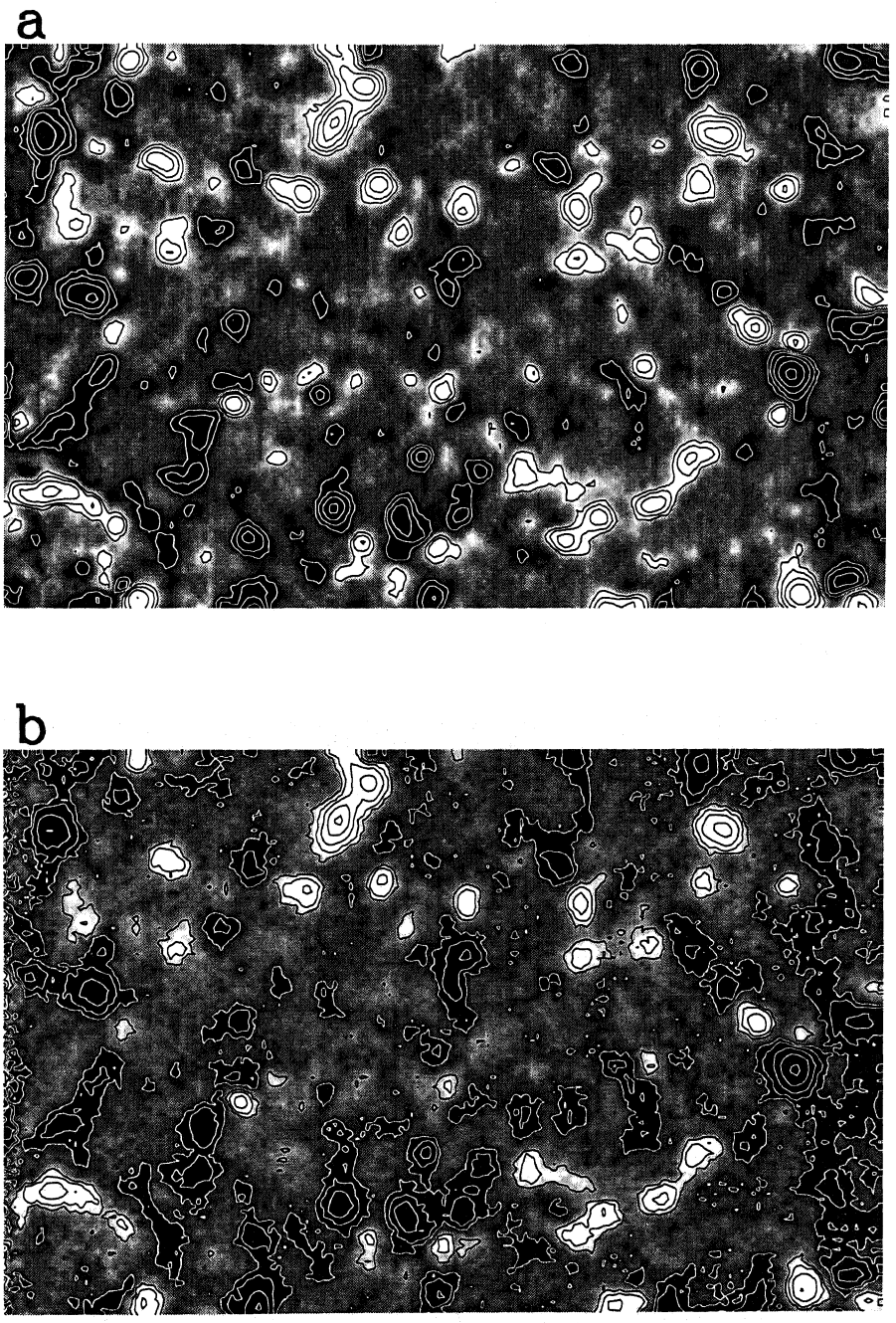

Fig.3.6 Observed integrated photospheric (a) and chromospheric (b) magnetograms in a quiet−Sun region near the disk center. The observation duration is from 01:45 UT to 06:45 UT on 15 September 1998. The field of view is 4.9′*3.1′. Bright(dark) structures correspond to positive (negative) polarities. Black (white) contours correspond to positive (negative) fields of 10, 20, 40, 80, 160 Guass.

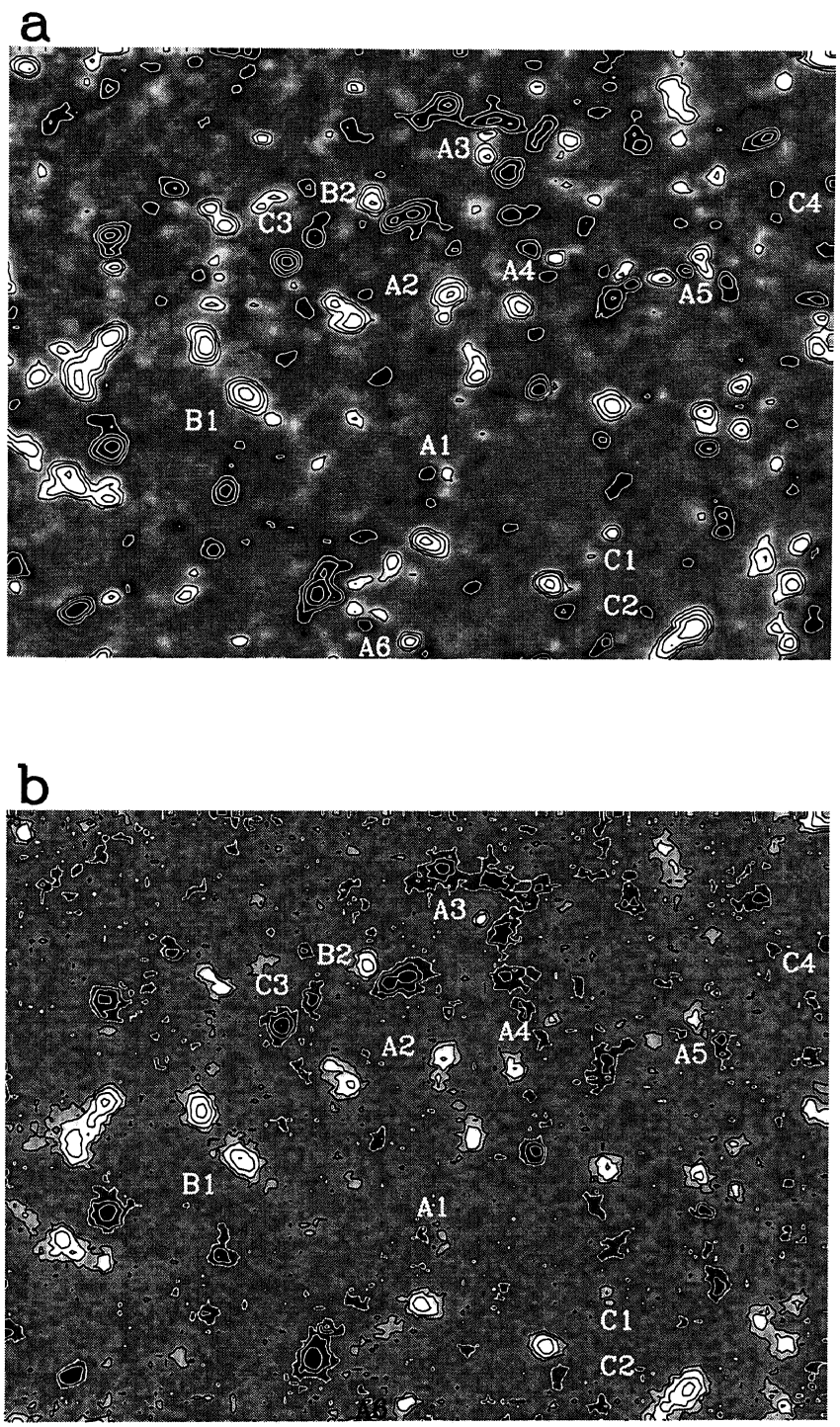

Fig.3.7 The photospheric (a) and chromospheric (b) magnetograms for duration from 02:07 UT to 04:15 UT in the quiet-Sun region near the disk center observed on 14 April 1998. The field of view is 4.6′*3.4′. Bright (dark) structures correspond to positive (negative) polarities. Black (white) contours correspond to positive (negative) fields of 15, 30, 60, 120 Guass.

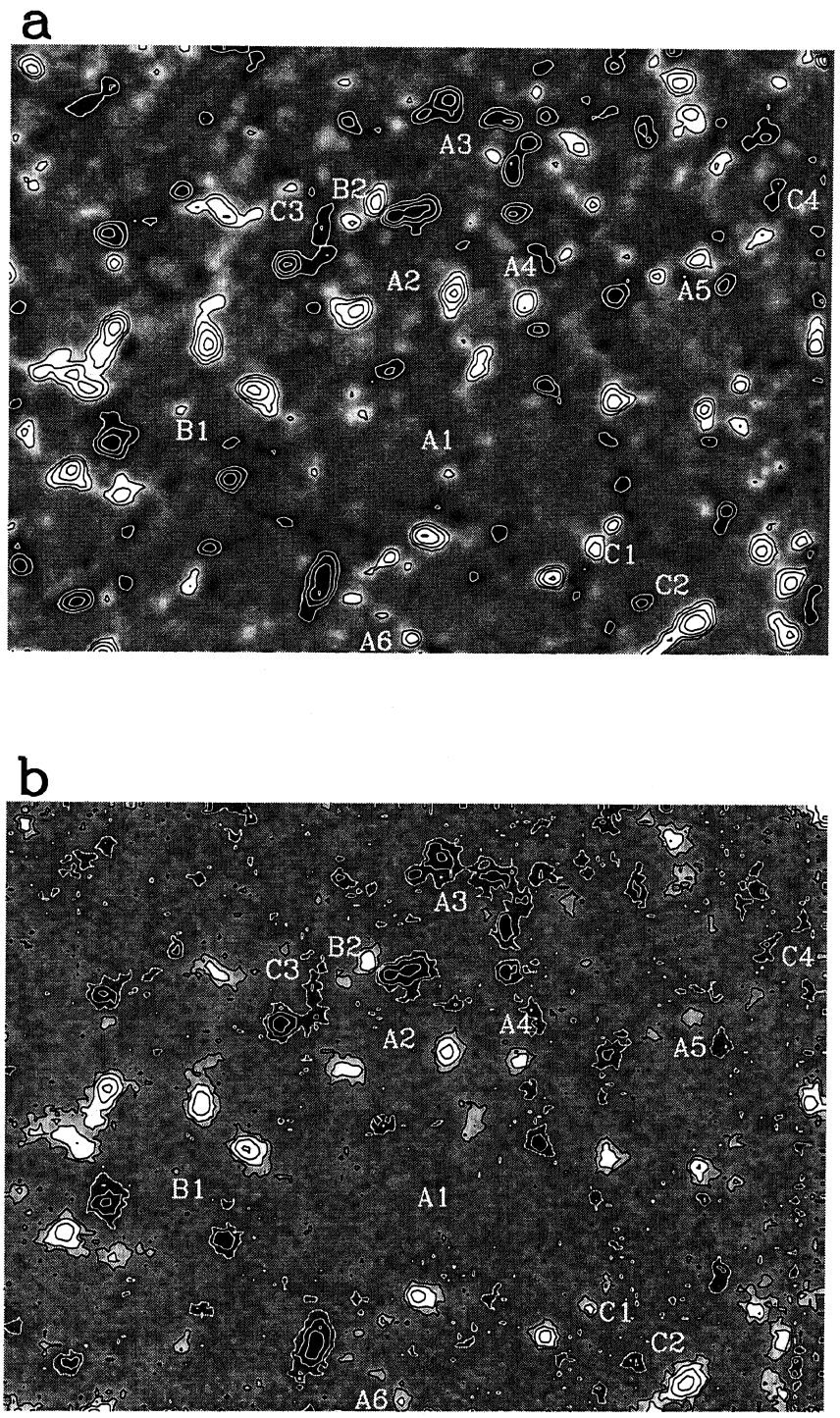

Fig.3.8 The photospheric (a) and chromospheric (b) magnetograms for duration from 04:20 UT to 06:40 UT in the quiet-Sun region near the disk center observed on 14 April 1998. The field of view is 4.6′*3.4′. Bright (dark) structures correspond to positive (negative) polarities. Black (white) contours correspond to positive (negative) fields of 15, 30, 60, 120 Guass.

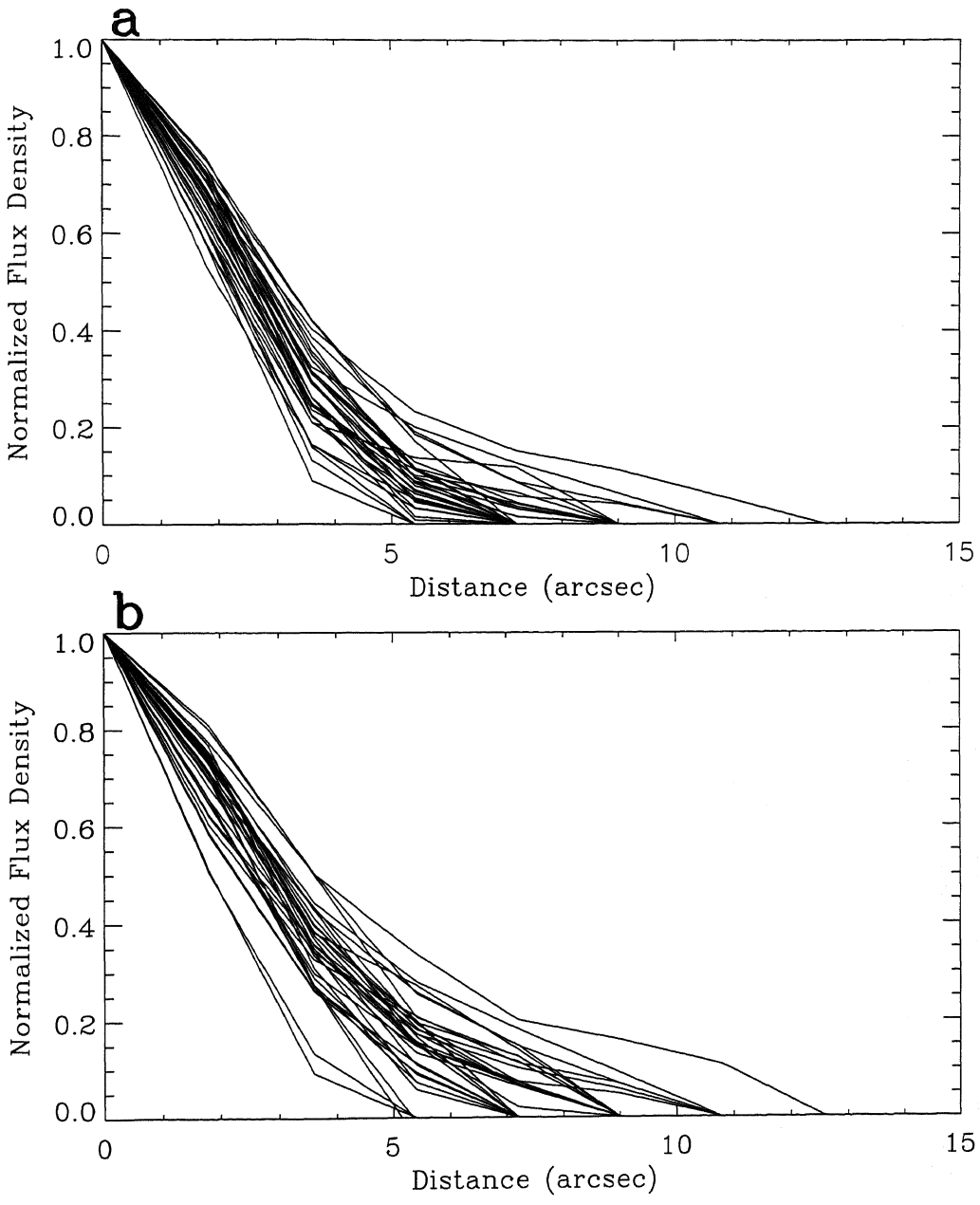

Fig.3.9 The normalized flux density profiles of the strongest 37 identical magnetic elements in the field observed on 14 April 1998. The X-axis is the angle distances from the centers of magnetic elements to their edges. The Y-axis is the normalized flux densities at different positions from the centers of magnetic elements.

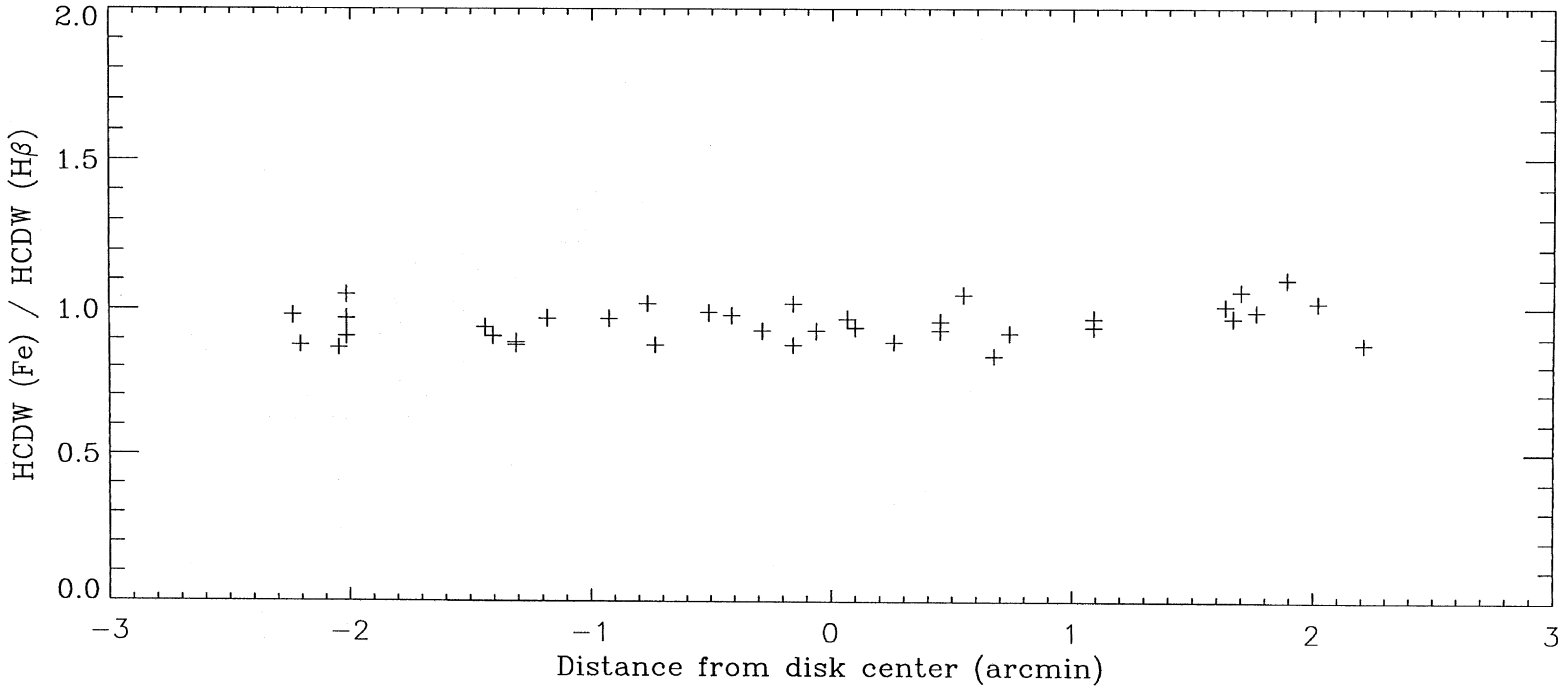

Fig.3.10 Diagram of the ratios between the photospheric HCDWs and corresponding chromospheric HCDWs of 37 identical networks observed on 14 April 1998. X−axis is the distances from disk center of identical elements. Y−axis is the ratios of HCDWs between the photospheric magnetic elements and corresponding chromospheric magnetic elements.

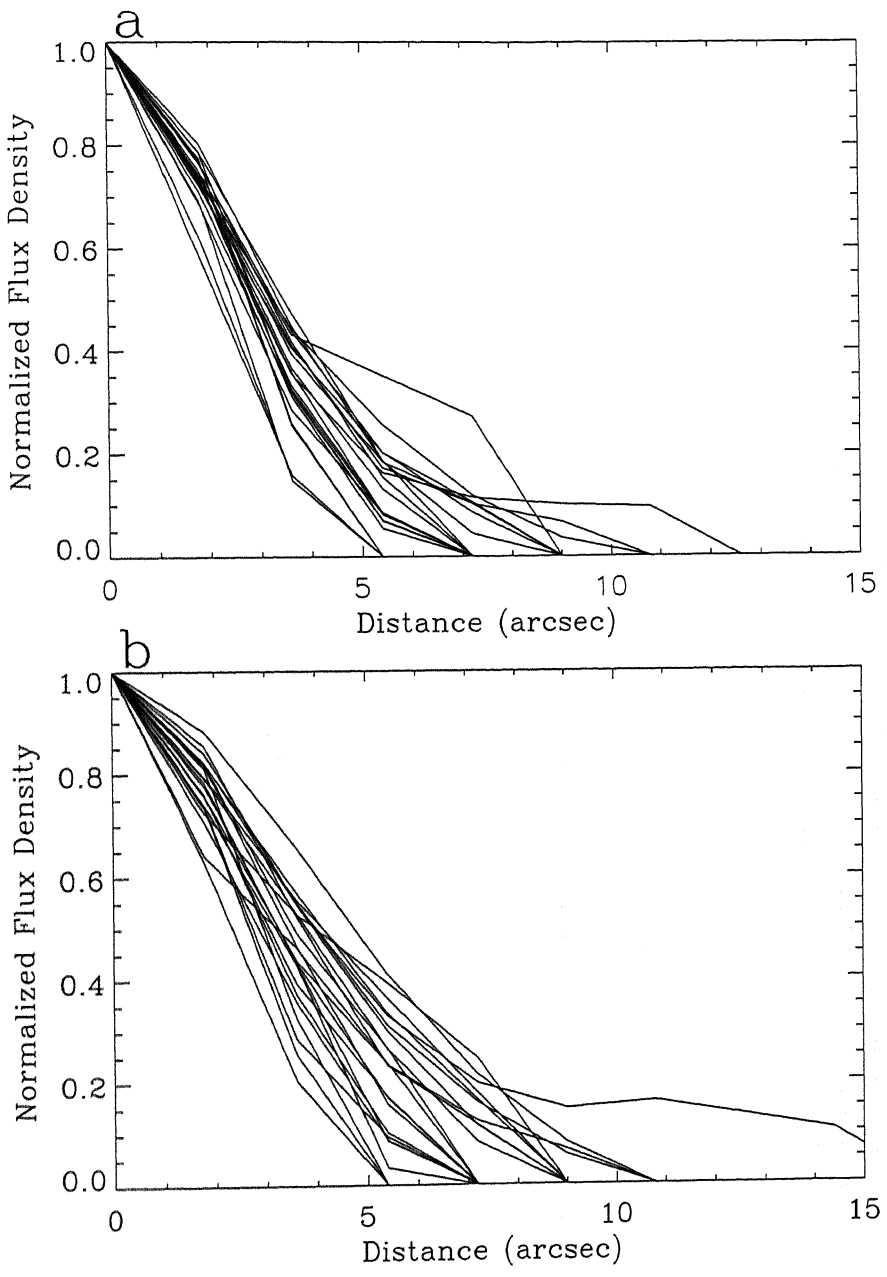

Fig.3.11 Normalized magnetic flux density profiles of 23 identical magnetic elements observed on 15 September 1998. The X-axis is the angle distances from the centers of magnetic elements to their edges. The Y-axis is the normalized magnetic flux densities at different positions from the centers of magnetic elements to their edges.

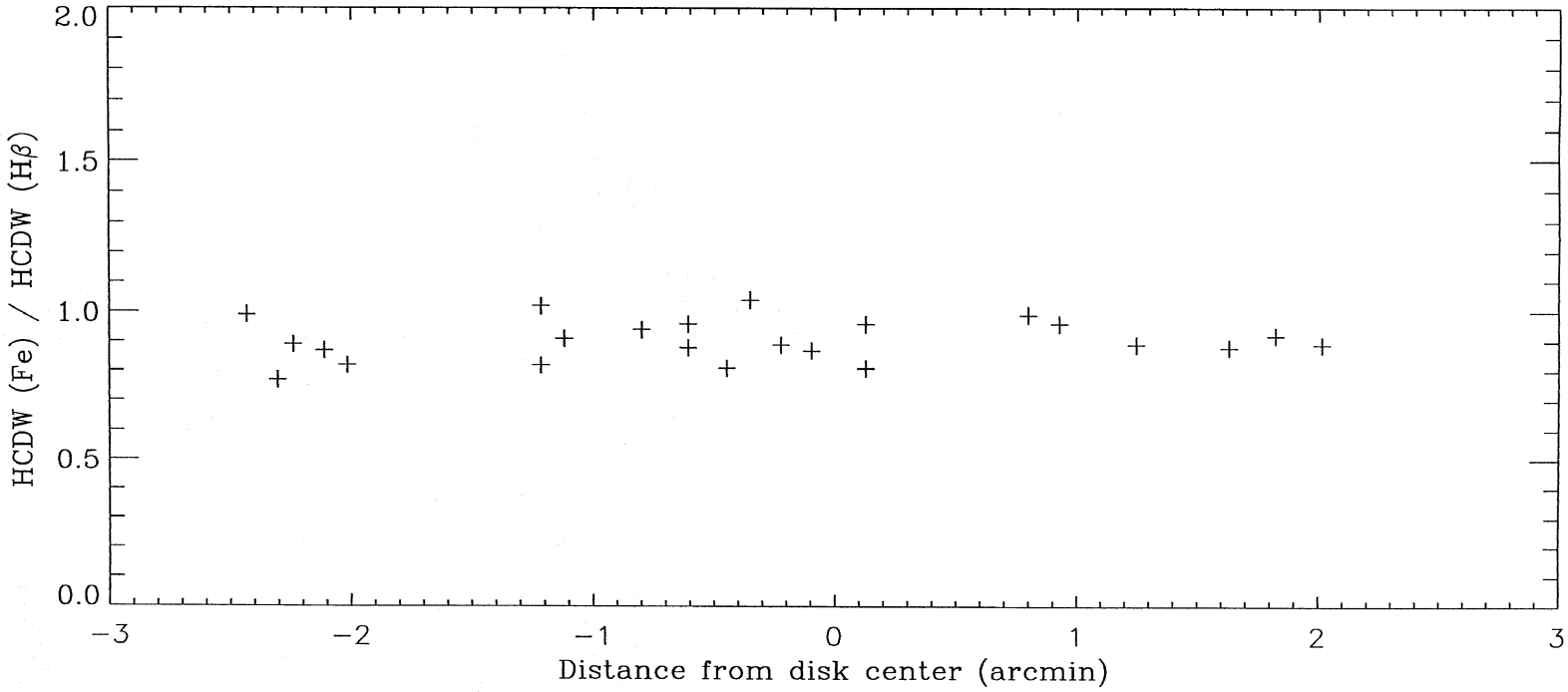

Fig.3.12 The ratios of HCDWs between photospheric magnetic elements and corresponding chromospheric elements observed on 15 September 1998. X−axis is the distances from disk center of identical magnetic elements. Y−axis is the ratios of HCDWs between the photospheric magnetic elements and corresponding chromospheric magnetic elements.

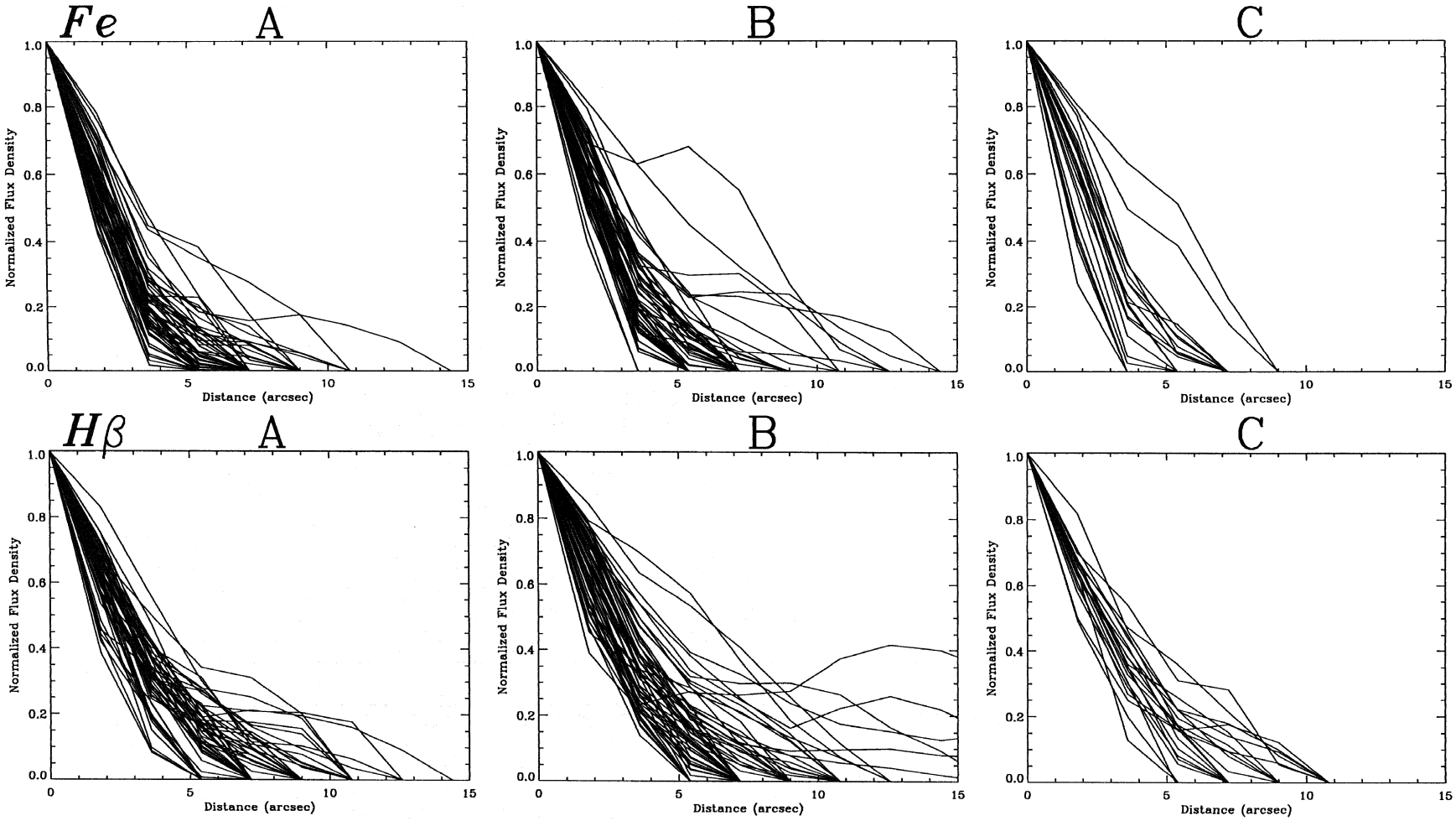

Fig.3.13 Normalized flux density profiles of identical network elements in regions A, B and C observed on 30 May 1998. The X−axis is the angle distances from the centers of magnetic elements to their edges. The Y−axis is the normalized flux densities at different positions from the centers of magnetic elements to their edges.

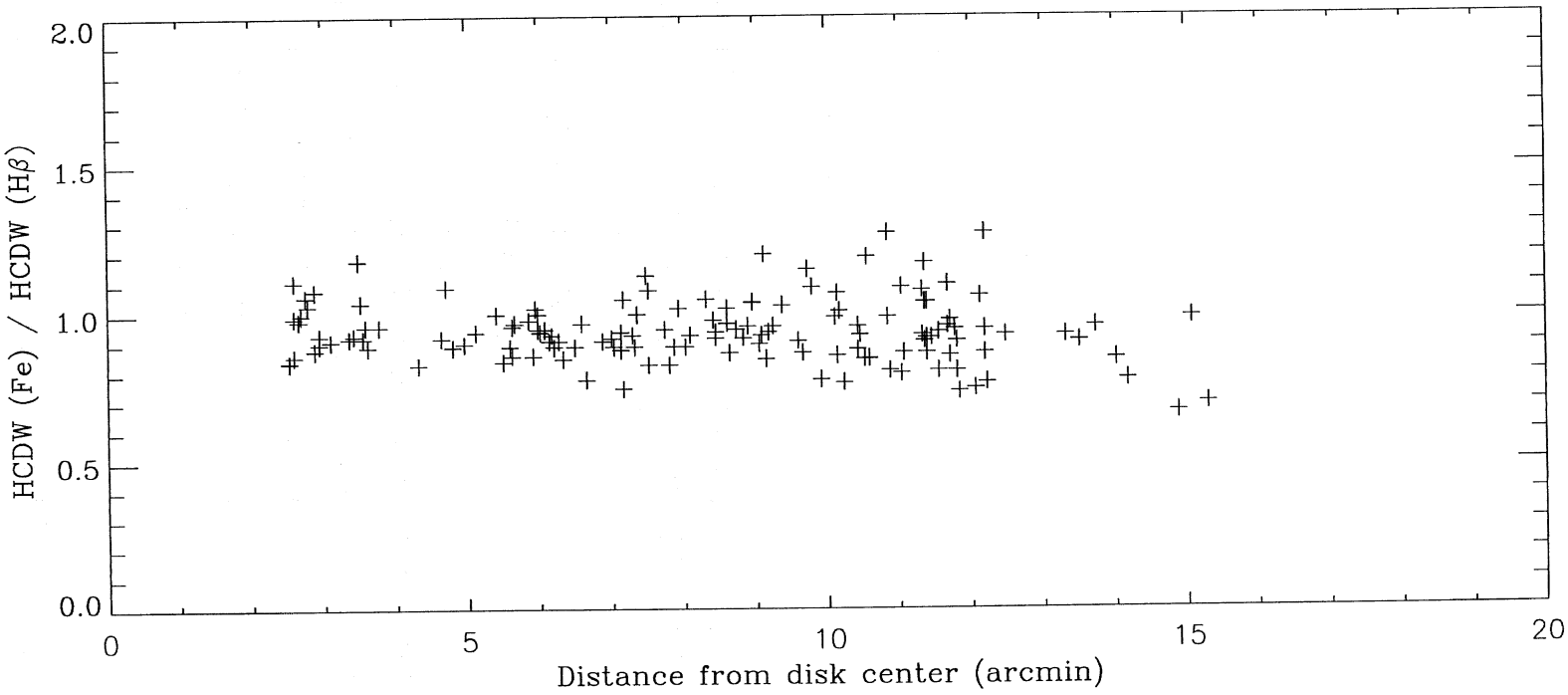

Fig.3.14 Diagram of the ratios between the photospheric HCDWs and corresponding chromospheric HCDWs of identical networks observed on 30 May 1998. X-axis is distances from disk center of identical elements. Y-axis is the ratios of HCDWs between the photospheric magnetic elements and corresponding chromospheric magnetic elements.

第四章　伞盖模型的理论分析

从第一章的讨论我们了解到，对于伞盖模型中的伞盖高度，理论和观测上一直存在着分歧。由于理论模型主要是从宁静区物理条件推出的，而以往观测主要在活动区进行，所以我们在上面的第二、三章中对宁静区光球和色球磁场进行了测量。观测发现，在宁静区似乎没有形成在活动区观测到的低伞盖结构。怎样解释这些现象和分歧呢？在这一章中，我们将对伞盖模型的理论模型进行一些分析和探讨。

4．1 模型

4．1．1 模型描述

为了进一步分析太阳宁静区磁流管的可能扩展形式，我们使用Athay(1981)[1]中采纳的伞盖模型的数学表达形式对磁流管的空间结构进行了分析。

这种模型假设了磁场为势场，因此有：

$$B = -\nabla\varphi$$

$$\nabla^2\varphi = 0$$

上述方程被用来在二维空间中求解。这个二维空间的长度取为 1，高度取为 b。长度和高度都以一个超米粒圆胞的大小（15000 公里）为归一化单位。磁场在左右两边及上边缘都被假设为是垂直的。在下边缘，纵向磁场被假设为是一个阶梯函数：

$B_z = B_0$ ，$0 \le x \le a$

$B_z = 0$ ，$x > a$

在上述边条件下，取 B_0=1 时，解出的磁场具有以下形式：

$$B_x(x,z) = \sum_{n=1}^{\infty} C_n \sin n\pi x \sinh n\pi(b-z)$$

$$B_z(x,z) = 1 + \sum_{n=1}^{\infty} C_n \cos n\pi x \cosh n\pi(b-z)$$

其中 $C_n = (2/n\pi a)*(\sin n\pi a / \cosh n\pi b)$

4．1．2 模型的局限性及与其他模型的关系

在以下的章节中，我们将用上述模型来描述伞盖状的磁流管的磁场结构。我们承认，对于一个真实的磁流管来说，这种模型也许过于简单化了。但是，也正是由于它的简单，使这个模型避开了对影响磁流管结构的各种物理过程的细节讨论，而只用两个自由参数（a 和 b）来描述各种可能的不同磁流管结构。可以粗略地认为，不同作者[2-5]在考虑不同物理条件下得出的不同磁流管结构,对应于此模型中不同参数（a 和 b）下的不同磁流管结构。当然，我们承认这种对应可能相当粗略，并且仔细研究控制磁流管结构的各种物理过程及其大小对精确地描述磁流管结构无疑是十分必要的。

4．2 磁流管的形状

4．2．1 参数 b 对磁流管形状的影响

对于不同的自由参数 a 和 b，磁流管将具有不同的形状。图 4.1 显示了四组参数下的磁流管形状（磁力线轮廓）。自由参数 a=0.1 相当于磁流管在光球底层（z=0）的大小为 1500 公里，与实际观测的光球磁图中的磁元大小相当。b=1.0 对应于磁流管中磁场在高于光球底层(z=0)15000 公里处变成完全垂直于光球，而 b=0.5、0.1、0.05 分别对应于磁流管中磁场在高于光球底层(z=0)7500、1500 和 750 公里处变成完全垂直于光球。

从图 4.1 可以看出，当 b 较大时（如 b=1.0 时），磁流管会膨胀到充满整个日面空间；而当 b 较小时，磁流管将不会膨胀到充满整个日面空间。如当 a=0.1(1500 公里)，b=0.1(1500 公里)时，磁流管只从 x=0.1(1500 公里)膨胀到 x=0.27(4050 公里)，而不会膨胀到 x=1.0(15000 公里)。

4．2．1 参数 a 对磁流管形状的影响

图 4.2 显示了另外四组参数下的磁流管形状（磁力线轮廓）。此处，自由参数 a 从 a=0.1 到 a=0.01 的变化模拟了光球磁元可能具有的不同填充因子（filling factor）的状况。从图 4.2 可以看出，在同一 b 值下，参数 a 的变化对磁流管的影响不大，这说明，这种模型对参数 a 的依赖不太敏感。

4．2．3 讨论

通过分析不同参数组合(a,b)下的磁场位形，我们发现：并不是所有这种模型所描述的磁流管都会膨胀到充满整个空间。只有在 b 较大时（如 b=15000 公里时），磁流管才会膨胀到充满整个空间。这说明不同的参数组合将给出不同形状的磁流管，亦即磁流管的结构可能存在着多样性。

4．3 磁流管中垂直磁场分量的结构特征

4．3．1 高层大气中磁场的结构特征

对于这个模型所描述的任何一组参数下的磁场，其垂直磁场在下边缘（z=0）都是一个阶梯函数。在接近下边缘处，磁场具有水平分量。这些水平分量使磁流管不断膨胀，直到磁场在上边缘(z=b)处变成完全垂直。

虽然磁流管内的磁场在上边缘（z=b）都是垂直的，但并不是所有的磁流管内的垂直分量在上边缘处都会变成均匀磁场。如图 4.3 即显示了四组参数下的磁流管内的垂直磁场的轮廓分布。从图 4.3 可以看出，只有那些 b 较大（如 b=15000 公里）的磁流管，其内部磁场最终才会变成均匀磁场。而那些 b 较小的磁流管，即使在上边缘，其内部磁场也是非常不均匀的。结合上面对磁流管形状的讨论，说明磁流管的结构可能存在着多样性，并不是所有的磁流管都会发展成为垂直均匀且充满整个空间的磁场。

4．3．2 低层大气中磁场的结构特征

从图 4.3 还可以看出，无论 b 大还是 b 小，磁流管在低于 1500 公里以下时，其内部垂直磁场都是非常不均匀的。这意味着这种模型预言磁场在色球层是不均匀的，应存在着孤立结构。

4．4 磁流管中水平磁场分量的结构特征

此模型所描述的磁流管在接近下边缘（z=0）时都存在水平分量，此水平分量使磁流管不断膨胀。随着磁流管的膨胀，此水平分量不断减小，直至最后磁场变成完全垂直（在 z=b 处）。因此，对于 b>0.1（1500 公里）的磁流管，我们应能在低于 1500 公里的高度上观测到水平磁场分量。

水平磁场分量可以通过观测日面边缘的纵向磁场得到。如图 4.4 即显示了此模型预言的在离日面中心 70°处的离光球底层（z=0）100 公里处应观测到的纵向磁图。图 4.5 显示了此模型预言的在离日面中心 70°处的离光球底层（z=0）200 公里处应观测到的纵向磁图。图 4.6 显示了此模型预言的在离日面中心 70°处的离光球底层（z=0）500 公里处应观测到的纵向磁图。图 4.7 显示了此模型预言的在离日面中心 70°处的离光球底层（z=0）1000 公里处应观测到的纵向磁图。在计算这些磁图时，我们将模型预言的磁场卷积了一个半宽σ = 2″的高斯函数（$g=e^{-x2/\sigma2}$），同时，我们还根据 Hayard(1987)[6]和 Venkataktrishman 等(1988)[7]中的方法将计算出的日球坐标(heliographic coordinates)磁场转化到了观测平面坐标(observational image planes)中。

从图 4.4—4.7 可以看出，在 b 较大的情况下，在日面边缘的各个层次（100 公里、200 公里、500 公里、1000 公里处），我们都应该能看到由两个不同极性组成的反映了磁场水平分量的极性反转对。当 b 较小时，我们也应该在低层次（100 公里、200 公里、500 公里处）看到极性反转对。这些极性反转对是磁流管存在水平分量的必然反映。值得一提的是，我们的宁静区日面西边缘的观测却没有观测到这样的极性反转对，这在第六章还将讨论。

4．5 关于伞盖高度的讨论

4．5．1 四种伞盖高度的定义

不同的作者在讨论伞盖模型时，经常会提到伞盖高度的计算。通过分析我们发现，在实际应用中存在着四种不同的对伞盖高度的定义。它们是：

第一种：磁流管内磁场变得完全垂直的高度，以 Z_A 表示。
第二种：磁流管内磁场变得几乎均匀的高度，以 Z_B 表示。此处我们将此高度估计为磁流管内磁通量密度变化小于 50%处。
第三种：两个相邻磁流管相碰的高度，以 Z_C 表示。一些作者将此高度定义为磁流管扩张到它最大大小的 80%处的高度，而另一些作者将此高度定义为磁流管扩张到充满 80%空间处的高度。这两者都是理论天文学家常常用来作为伞盖高度的定义。
第四种：磁场较为水平的高度，以 Z_D 表示。

4．5．2 同一磁流管中的四种伞盖高度

通过分析我们发现：即使对于同一个磁流管，上述四种伞盖高度的值亦各不相同。如图 4.8 即为一个参数 a=0.1（1500 公里），b=1.0（15000 公里）模型描述的磁流管。这也是人们普遍采用的一种磁流管模型。实线表示磁流管从光球开始向上膨胀的形状。虚线代表着磁流管内部磁场的等倾角线。这里的倾角是指磁场相对于光球的倾角，即 $tg\theta=B_y/B_x$。

计算表明，第一种高度（Z_A），即磁流管内磁场变得完全垂直的高度，为 15000 公里。第二种高度（Z_B），即磁流管内磁场变得几乎均匀的高度，为 8500 公里。第三种高度（Z_C），即两个相邻磁流管相碰的高度，在 2800 - 4200 公里之间。前者（2800 公里）为磁流管扩张到它最大大小的 80%处的高度。后者（4200 公里）为磁流管扩张到充满 80%空间处的高度。第四种高度(Z_D)，为磁场较为水平的高度。在图 4.7 中可估计为$\theta=20^0$等轮廓线处。可以看出，此高度较低，在 0 - 1500 公里之间。而实际上，这也是大量观测者发现低伞盖处。

4．5．3 讨论

从以上分析可以看出：即使对于同一参数模型下描述的同一磁流管，在接近光球处磁流管内的磁场较接近水平，在中等高度处相邻的磁流管互相相碰，而磁流管内的磁场要到较高处才变得均匀或垂直。因此，以往那种认为在伞盖高度处磁场是水平的而过了伞盖高度磁场就一下子变得均匀且垂直的模型，显然是过于简单化了。因此，我们一定要注意区分我们定

义的不同伞盖高度。同时，这也可能是理论天文学家和观测天文学家对伞盖高度分歧的部分来源。

4. 6 总结

通过对 Athay(1981)[1]模型的分析,我们发现:

1. 并不是所有这种模型所描述的磁流管都会膨胀到充满整个空间。只有在 b 较大时（如 b=15000 公里时），磁流管才会膨胀到充满整个空间。这说明不同的参数组合将给出不同形状的磁流管，亦即磁流管的结构可能存在着多样性。
2. 并不是所有这种模型所描述的磁流管内的磁场都会膨胀到成为均匀磁场。亦只有在 b 较大时，磁流管内的磁场才会膨胀到变成均匀磁场。
3. 磁流管的磁场在低于 1500 公里以下时是非常不均匀的。
4. 在 b 较大的情况下，在日面边缘的各个层次（100 公里、200 公里、500 公里、1000 公里处），我们都应该能看到由两个不同极性组成的反映了磁场水平分量的极性反转对。当 b 较小时，我们也应该在低层次（100 公里、200 公里、500 公里处）看到极性反转对。
5. 伞盖模型中的伞盖高度会因定义的不同而产生估计值上的不同。即使对于同一参数模型下描述的同一磁流管，在接近光球处磁流管内的磁场较接近水平，在中等高度处相邻的磁流管互相相碰，而磁流管内的磁场要到较高处才变得均匀或垂直。

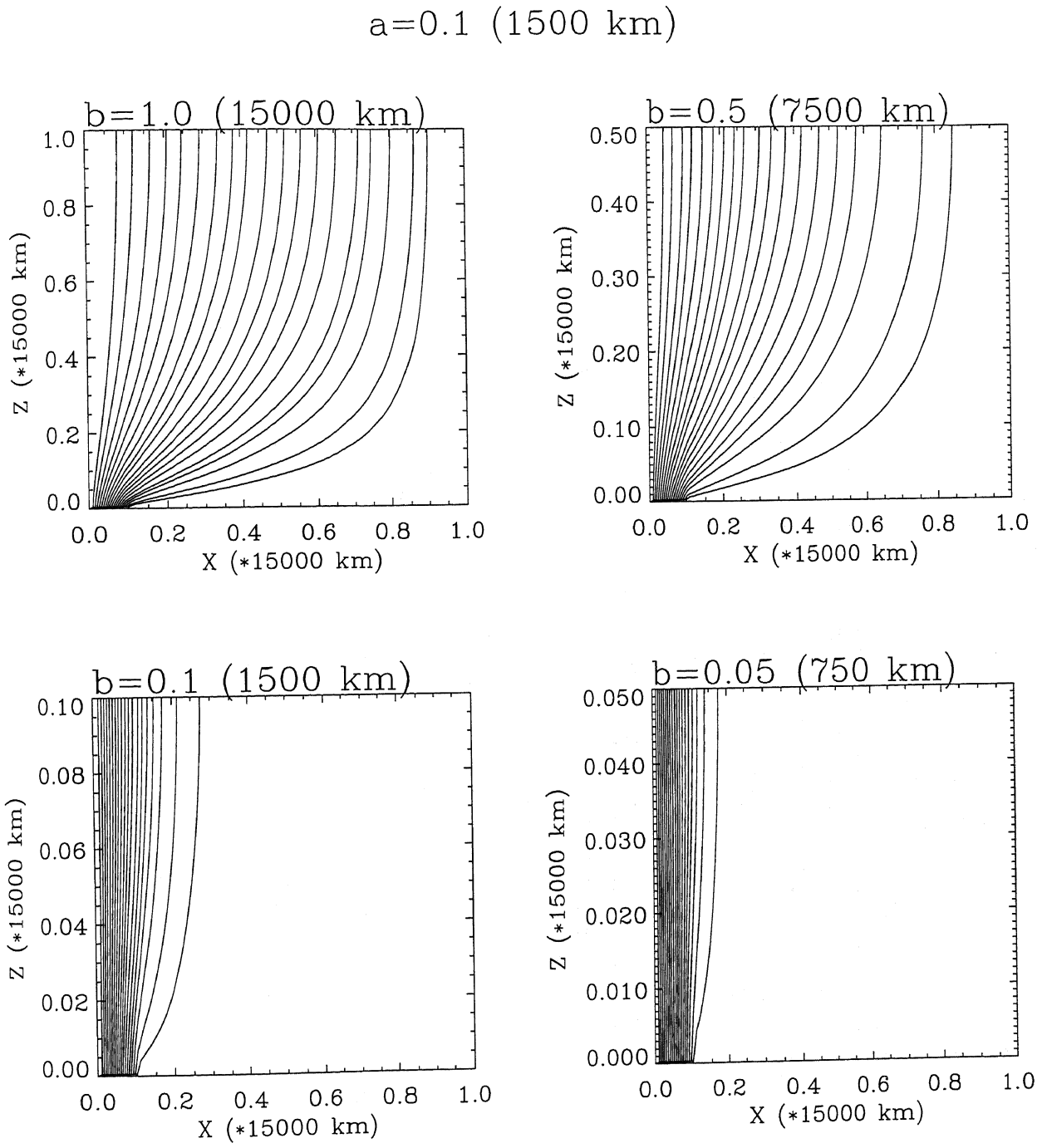

Fig.4.1 Magnetic field configurations (magnetic field lines) for four magnetic parameter series (a=0.1,b=1.0), (a=0.1,b=0.5), (a=0.1,b=0.1) and (a=0.1,b=0.05). The X-axis is the distance from the center of a network segment (x=0) in the unit of 15000 km. The Y-axis is the height from the solar photosphere (z=0) to higher atmosphere (z=b) in the unit of 15000 km.

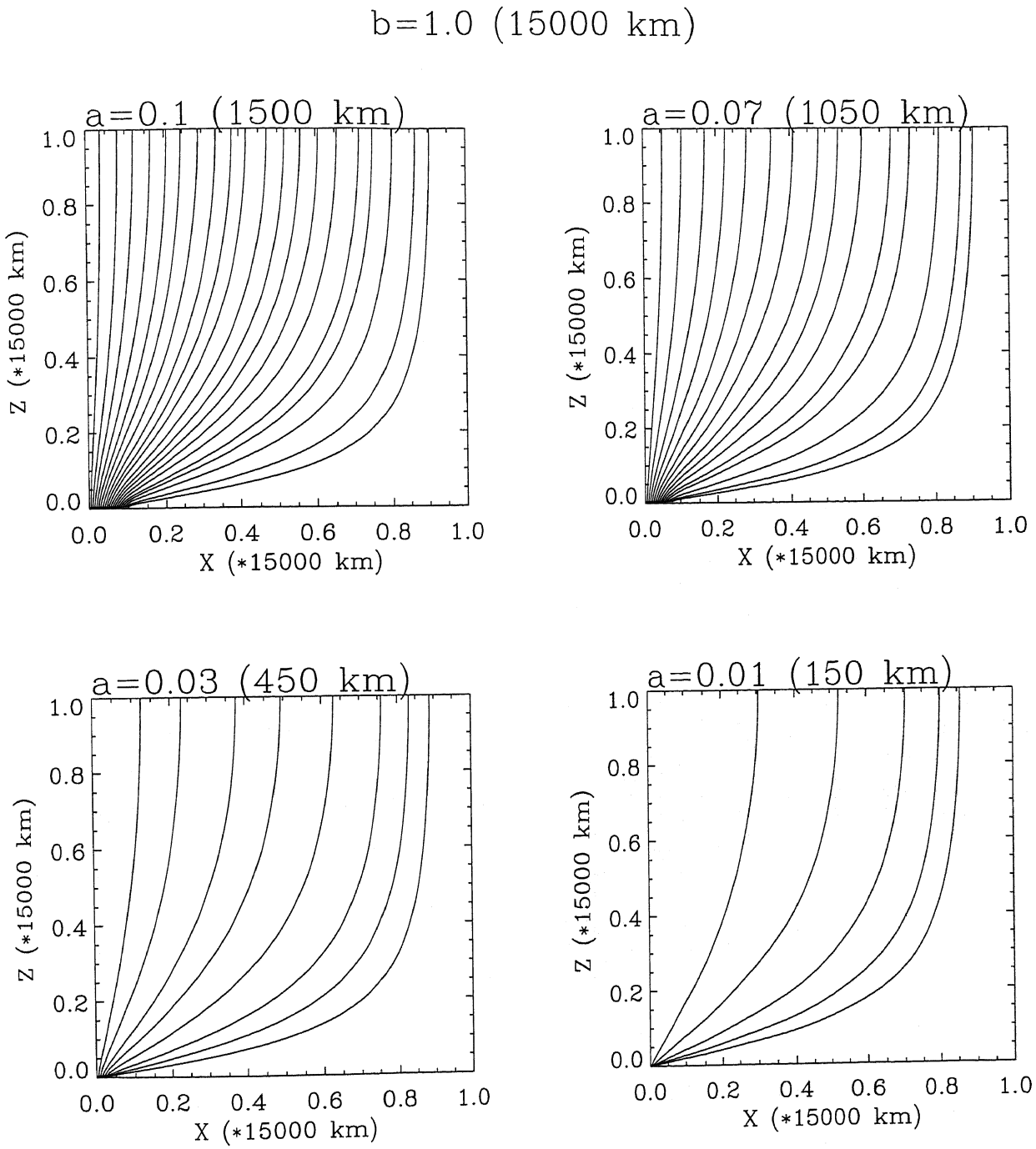

Fig.4.2 Magnetic field configurations (magnetic field lines) for four magnetic parameter series (a=0.1,b=1.0), (a=0.07,b=1.0), (a=0.03,b=1.0) and (a=0.01,b=1.0). The X-axis is the distance from the center of a network segment (x=0) in the unit of 15000 km. The Y-axis is the height from the solar photosphere (z=0) to higher atmosphere (z=b) in the unit of 15000 km.

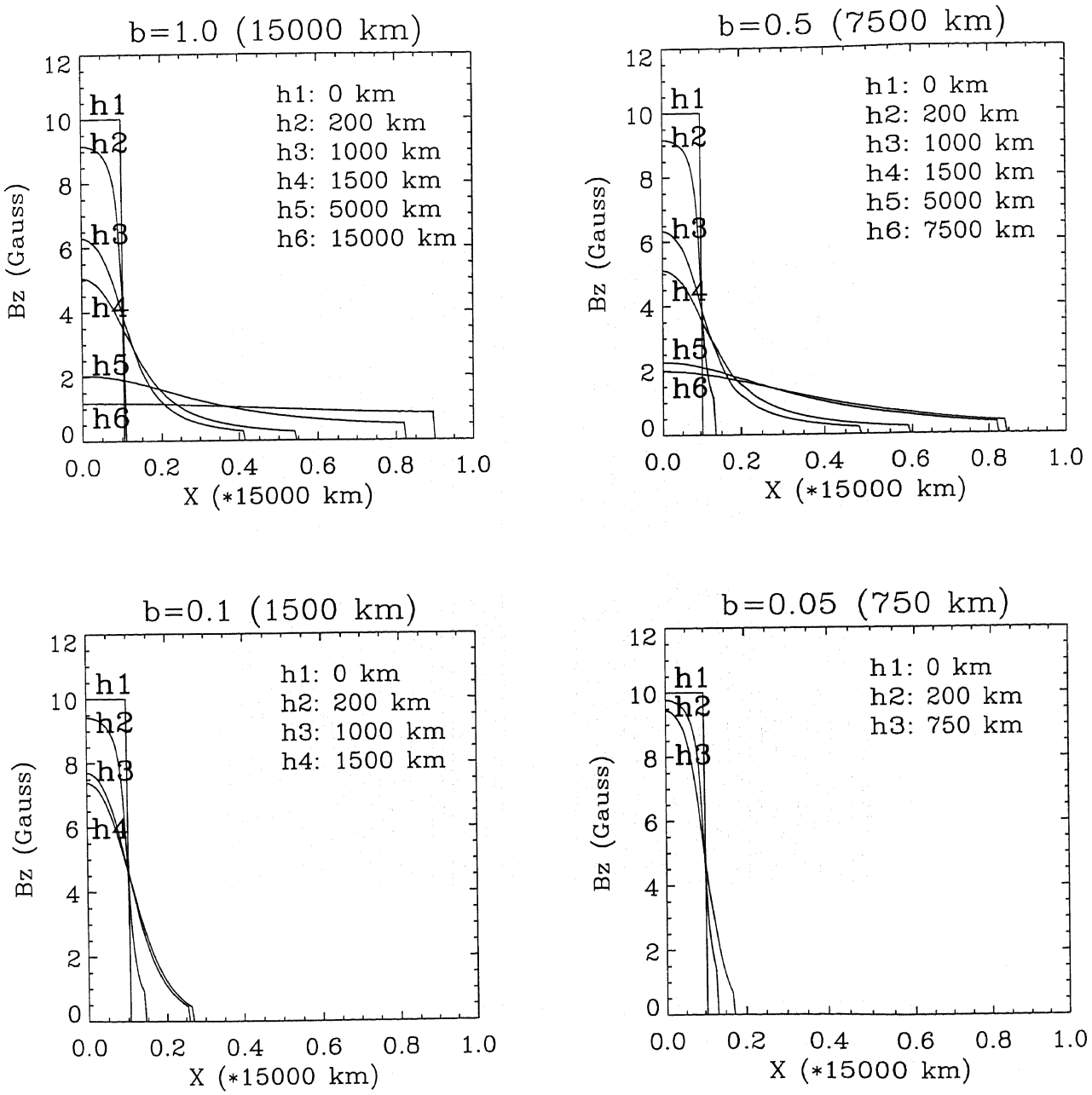

Fig.4.3 Vertical magnetic flux density profiles at different heights for four magnetic parameter series (a=0.1,b=1.0), (a=0.5,b=1.0), (a=0.1,b=0.1) and (a=0.1,b=0.05). The X-axis is the distance from the center of a network segment (x=0) in the unit of 15000 km. The Y-axis is the vertical magnetic flux densities in the unit of Gauss by assuming B_o=1.0 Gauss. (See text)

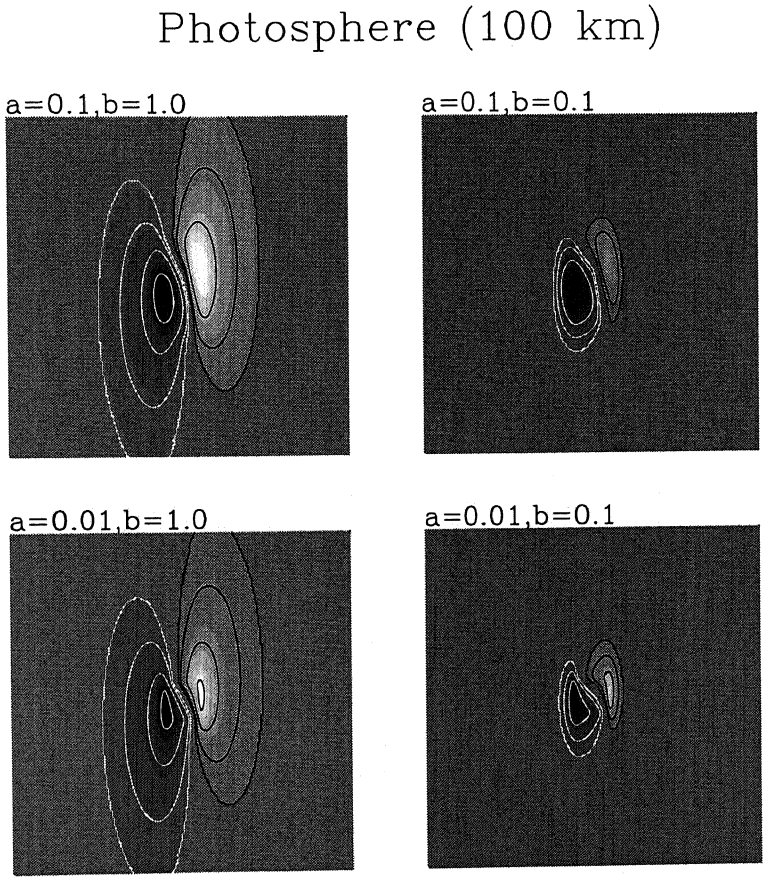

Fig.4.4 Model-predicated photospheric (100 km) magnetograms near the solar limb (70° away from the disk center) for four magnetic parameter series (a=0.1,b=1.0), (a=0.1,b=0.1), (a=0.01,b=1.0) and (a=0.01,b=0.1).

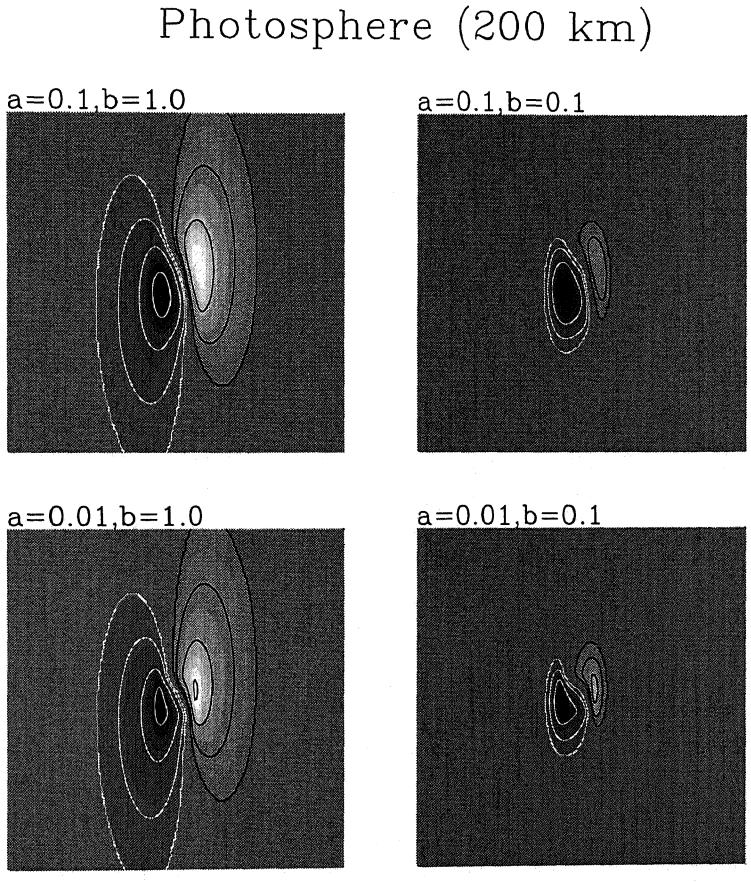

Fig.4.5 Model-predicated photospheric (200 km) magnetograms near the solar limb (70° away from the disk center) for four magnetic parameter series (a=0.1,b=1.0), (a=0.1,b=0.1), (a=0.01,b=1.0) and (a=0.01,b=0.1).

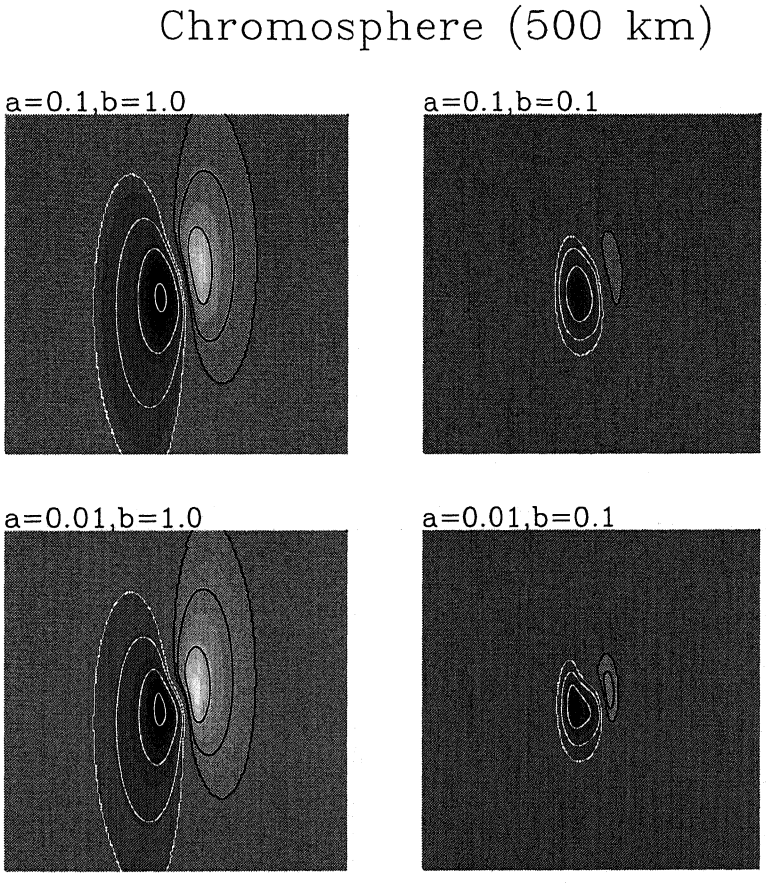

Fig.4.6 Model-predicated low-chromospheric (500 km) magnetograms near the solar limb (70° away from the disk center) for four magnetic parameter series (a=0.1,b=1.0), (a=0.1,b=0.1), (a=0.01,b=1.0) and (a=0.01,b=0.1).

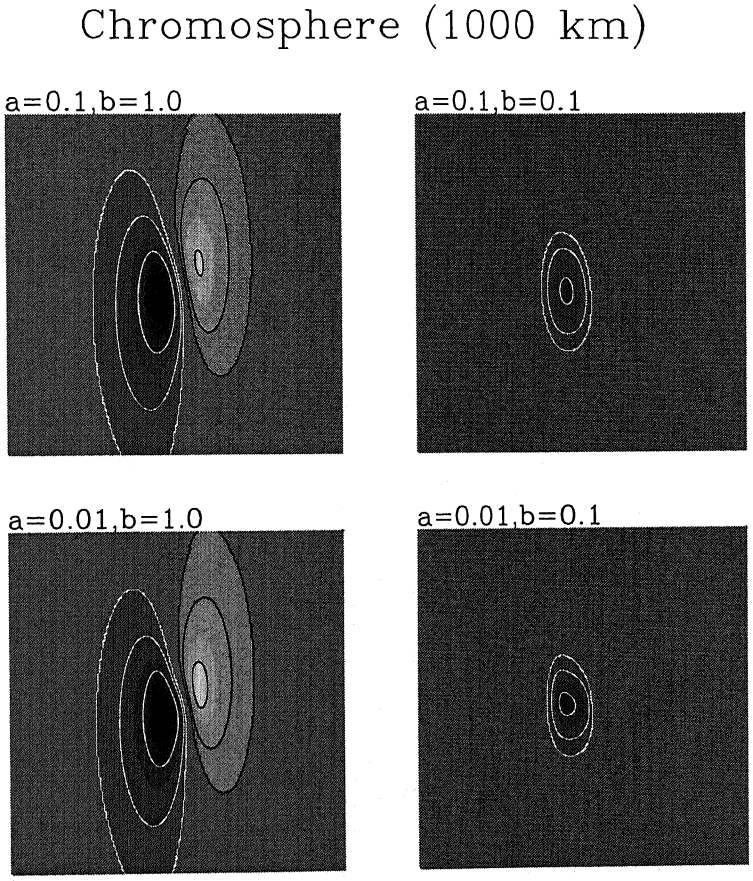

Fig.4.7 Model-predicated chromospheric (1000 km) magnetograms near the solar limb (70° away from the disk center) for four magnetic parameter series (a=0.1,b=1.0), (a=0.1,b=0.1), (a=0.01,b=1.0) and (a=0.01,b=0.1).

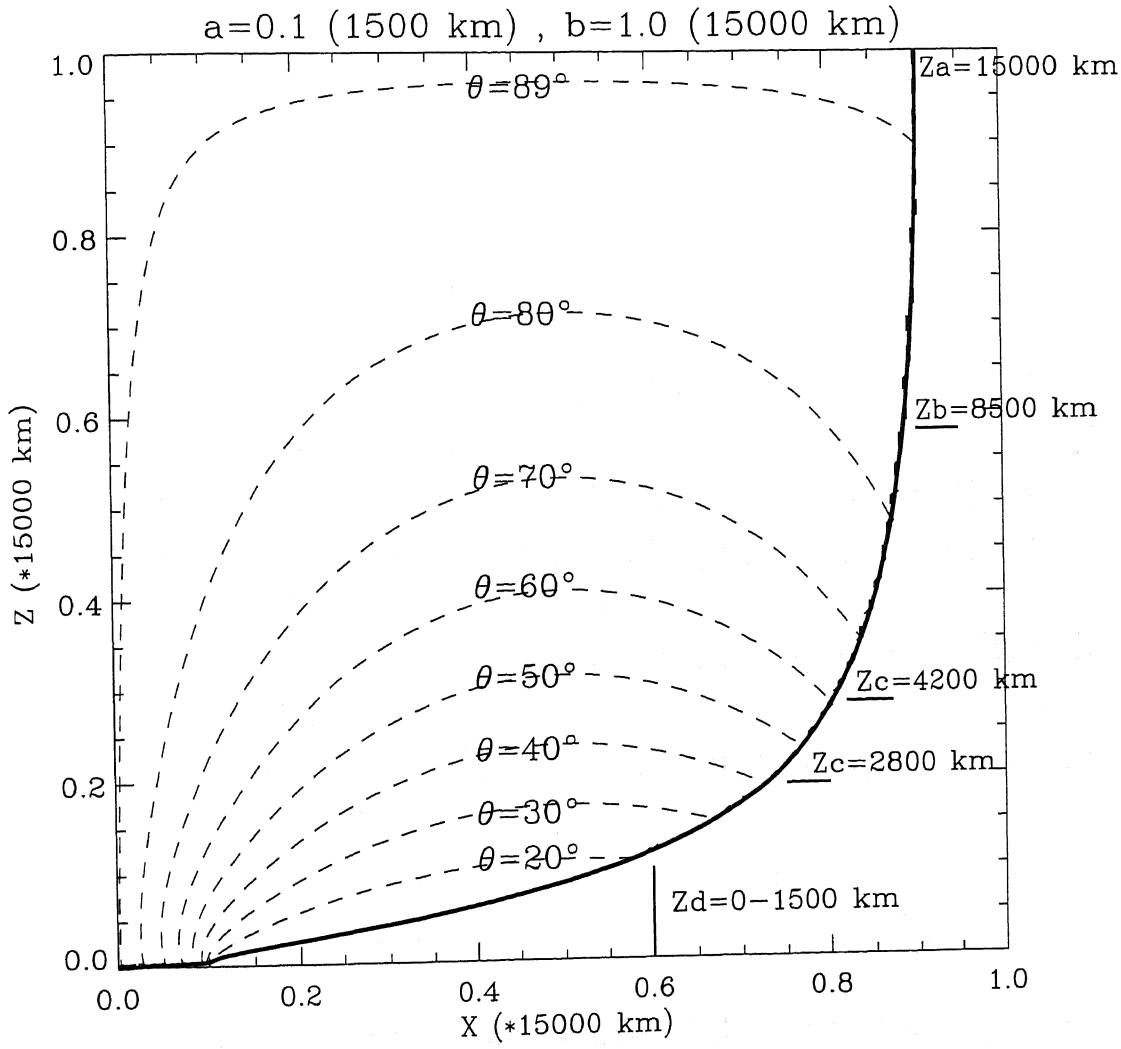

Fig.4.8 The field configuration for magnetic parameters a=0.1 and b=1.0. The solid line is the out-most magnetic field line that outlines the tube shape. The dashed lines are contours of magnetic field angles (θ) within the tube. Za, Zb, Zc and Zd show the four canopy heights of this magnetic tube.

第五章 谱线形成深度的探讨

从第一章的介绍可以看到，怀柔太阳磁场望远镜[1]是利用 FeI5324.19 埃谱线和 H_β4861.24 埃谱线来进行太阳光球和色球磁场观测的。对观测结果的深入理解与解释，无疑依赖于对这两条谱线形成深度的探讨。为此，在这一章中，作者集中了一些不同作者对这两条谱线形成深度的探讨，并在结合这些探讨的基础上提出了对这些问题的一些看法。

5．1 FeI5324 谱线的形成深度

1．艾国祥等(1982)[2]以及张洪起(1986)[3]都对 FeI5324.19 埃谱线的形成进行了计算。张洪起(1986)[3]用 Unno-Rachkovsky 方程计算了光球和黑子本影磁场内 FeI5324.19 埃谱线的形成过程。计算表明，当对日面中心观测、在滤光器调至线心时，I 形成在日面中心光球层以上 100 公里左右，在偏离线心 0.15 埃时 V 分量形成高度亦是如此。

2．林元章等(1996)[4]通过计算确定 FeI5324 谱线在日面边缘形成在 τ_{5000}=1 以上大约 180 公里处。

3．刘扬等（1996）[5]论述了 FeI5324 谱线形成在τ_{5000}=1 以上大约 100 公里处（引用张洪起(1986)[3]结果)。

5．2 H_β谱线的形成深度

1．张洪起等(1986)[6]以及张洪起和张枚(1998)[7]都对 H_β4861.24 埃谱线的形成进行了探讨。张洪起和张枚(1998)[7]计算了 H_β谱线的形成。计算表明，H_β谱线形成在温度极小区两边的光球和色球两个层次上(图 5.1)。在离 H_β谱线线心 0.25 埃处，H_β谱线的平均形成深度为 $\ln\tau_c$=-5，其中τ_c为 5000 埃处连续谱光学深度。与 VAL 大气模型比较表明，此形成深度大约对应于高出光球 1500-1600 公里。

2．Allen 在《天体和天体物理量》[8]一书中论述了 H_β谱线线心的形成高度为 1900 公里。

3. 林元章等(1996)[4]论述了离 H_β谱线线心-0.24 埃处的谱线形成在色球底（T_{min}）之上 1000-1500 公里，相当于τ_{5000}=1 以上大约 1500-2000 公里处。

4. 刘扬等(1996)[5]论述了离 H_β谱线线心-0.24 埃处的谱线形成在τ_{5000}=1 以上大约 1600 公里处。

5. Vernazza 等(1973)[9]在计算标准宁静太阳大气模型时确定 H_β谱线形成在τ_{5000}=1 以上大约 100-400 公里处。

5．2．1 H_β谱线相对于 FeI5324 谱线的观测形成深度

利用日面边缘活动区的观测，我们可以粗略地估计 H_β谱线在偏离线心-0.24 埃处的形成深度。如图 5.2 即为 1991 年 6 月 4 日观测的一个活动区的光球（Fe5324 谱线）和色球（H_β谱线）的单色像。图 5.3 为色球单色像（黑白像）和光球单色像（轮廓）以强度中心为基准点叠加后的图。从图 5.2 和 5.3 都可以看出，色球日球比光球日球大。这种区别可以用来估计色球 H_β谱线的形成高度。从图 5.2 和 5.3 中，估计 H_β谱线在日面边缘形成层的厚度在 Fe5324 谱线形成层以上约 3000-4000 公里处。

5．3 几点思考

从以上的总结可以看出，人们对 Fe5324 谱线形成深度的认识基本一致，认为它形成在高出τ_{5000}=1 以上 100-200 公里处。而对 H_β谱线形成深度的认识，Vernazza 等人的结论则与其他人的相差甚远。如何解释这一现象，则有待于进一步的对 H_β谱线形成的深入研究。

5．3．1 从对 H_α谱线形成深度的估计看 H_β谱线形成深度

H_α谱线与 H_β谱线相似，同属于氢的巴耳末线系。由于国际上采用 H_α谱线进行色球观测的仪器较多，因此对 H_α谱线形成的探讨相对较多一些。不同作者对 H_α谱线的形成的认识亦存在着不同。以下列举几种不同的观点：

1. Allen 在《天体和天体物理量》[8]一书中论述了 H_α谱线线心的形成高度为 3000 公里。

2. Vernazza 等在 ApJ(1973)[9]一文中论述了 H_α谱线形成在τ_{5000}=1 以上大约 300-1600 公里处。
3. White 等[10]利用日面边缘光谱观测测量 H_α谱线形成深度，测量结果显示 H_α谱线形成在 2500±700 公里处。

从以上对 H_α谱线形成深度的讨论可以看出，Vernazza 等人对 H_α谱线形成深度的计算结果亦低于其他两组。如果我们认为 White 等基于观测的结果（1800-3200 公里）较为可靠，Vernazza 等的估计值（300-1600 公里）则相差大约 1500 公里。如果我们认为 Vernazza 等对 H_β谱线形成深度的估计亦相差约 1500 公里，则 H_β谱线的形成深度应改为 1600-2000 公里，而与其他作者的估计接近。

5．3．2 利用 H_β谱线进行的观测研究

一些作者利用怀柔 H_β谱线进行的色球磁场研究从另一方面旁证了 H_β谱线应形成在光球以上的一定高度：

1．刘扬等(1996)[5]在假定 H_β谱线形成在τ_{5000}=1 以上 1600 公里的前提下，推出的活动区磁场的纵向梯度与从$\nabla\bullet B=0$ 出发推出的纵向磁场梯度值相符，从另一个角度说明了认为 H_β谱线形成在τ_{5000}=1 以上 1600 公里的前提的合理性。

2．张洪起[12]在 H_β谱线线翼不同波段处测得的色球磁场显示，在偏离 H_β谱线线心很远的线翼处，测得的磁场结构与光球磁场相似。而当观测波段向线心靠近时，测得的磁场显示出不同程度地逐步向外扩展的结构。这说明从 H_β谱线线翼到线心，逐步反映了越来越高的色球磁场结构。

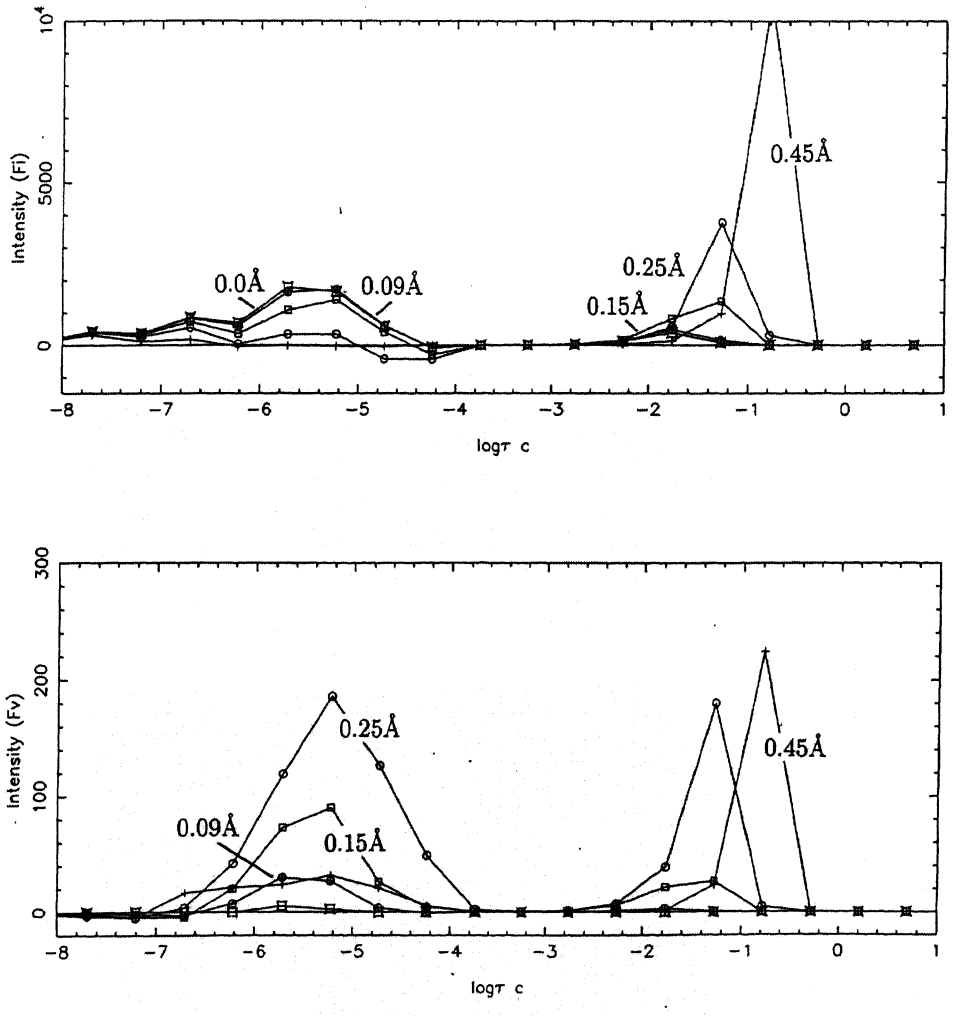

Fig.5.1 Contribution function of Stokes parameter I (top) and V (bottom) of the H_β line at the wavelengths $\Delta\lambda$=0.45,0.25,0.15,0.09 and 0.0 A from the line center. τ_C is the continuum optical depth at 5000A. The strength of the magnetic field B=1000 Gauss with inclination ψ=30°, azimuth φ=22.5° and μ=1 (from Zhang and Zhang (1998)[7]).

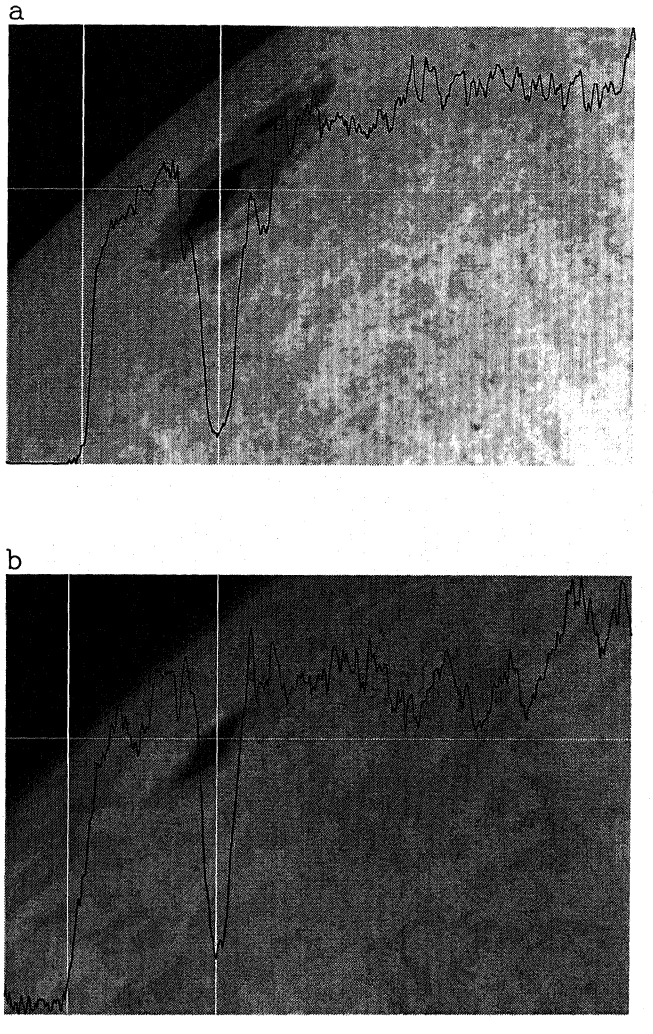

Fig.5.2 The photospheric (Fe5324) filtergram (a)
and the chromospheric (Hβ) filtergram (b).

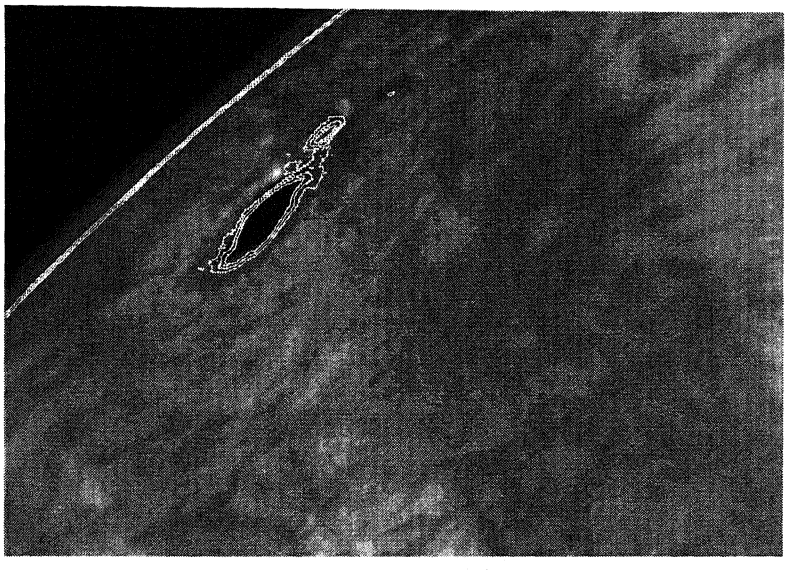

Fig.5.3 The photospheric (Fe5324) filtergram (contours) overlayed on the chromospheric (Hβ) filtergram.

第六章 观测对理论模型的可能限制

在这一章中，我们将在总结前几章观测和理论分析的基础上,对观测对理论模型的可能限制作出分析。

6．1 日面中心观测结果与理论的比较

6．1．1 观测结果

色球磁元具有与光球磁元相似的磁场结构。在现有观测分辨率下，磁元从光球到色球的扩散程度不大（第三章结论 3）。

比较利用 Fe5324 谱线观测的光球磁图和利用 H_β谱线（离线心-0.24 埃处）观测的色球磁图，我们发现，光球磁元和色球磁元的半强宽（磁元中心扩展到磁场强度为磁元中心磁场强度一半时的宽度）的中位数都位于 2.5″。每对磁元的光球半强宽与色球半强宽的比值位于 0.84 到 1.10 之间，中位值为 0.96。

比较利用 Fe5324 谱线观测的光球磁图和利用 H_β谱线（离线心-0.16 埃处）观测的色球磁图发现，光球磁元的半强宽从 2.2″到 2.9″，中位数位于 2.6″；色球磁元的半强宽从 2.3″到 3.6″，中位数位于 2.8″。每对磁元的光球半强宽与色球半强宽的比值位于 0.77 到 1.04 之间，中位值为 0.89。

6．1．2 理论预计

1．Athay(1981)[1]模型预言，磁流管的磁场在低于 1500 公里以下时是非常不均匀的（第四章结论 3）。

2．Athay(1981)[1]模型亦预言了磁流管在不同高度处应有的半强宽值。

如图 6.1 即为计算所得的在 a=0.1 情况下 Athay(1981)[1]模型预言的在不同高度处应有的半强宽值（虚线）以及在 200 公里处的半强宽与在其他高度处半强宽值的比值（实线）。图中是实线 a 代表在 200 公里处的半强宽值与在 500 公里处的半强宽值的比值。实线 b 代表在 200 公里处的半强宽

值与在 1000 公里处的半强宽值的比值。实线 c 代表在 200 公里处的半强宽值与在 1500 公里处的半强宽值的比值。在计算中，我们将理论计算的磁场卷积了一个高斯函数（$g=e^{-x2/\sigma2}$）以模拟大气抖动效应(seeing effect)。我们计算了四种大气抖动状况，即：σ=1.6″, 2.0″, 2.6″和 3.0″。图 6.2 与图 6.1 类似，只不过 a=0.01。

从图 6.1 和 6.2 可以看出，在 a=0.1 和 0.01 两种情况下，不同的 seeing 和 b 值都会改变模型预言的半强宽值，但半强宽的比值（图中实线 a，b 和 c）则表现出一定的稳定性。在 a=0.1 情况下，对于不同的 seeing 和大多数 b 值，200km/500km 的比值(a)多数在 0.92 附近，200km/1000km 的比值(b)多数在 0.81 附近，200km/1500km 的比值(c)多数在 0.72 附近。在 a=0.01 情况下，对于不同的 seeing 和大多数 b 值，200km/500km 的比值(a)多数在 0.90 附近，200km/1000km 的比值(b)多数在 0.70-0.80 之间，200km/1500km 的比值(c)多数在 0.60-0.70 之间。

6．1．3 观测与理论的比较

将日面中心观测给出的光球和色球磁元半强宽的值与理论模型计算给出的半强宽值进行比较发现：只有假设 H_β形成在很低层次（小于 500 公里）时，观测的光球和色球半强宽比值才有可能符合理论预言的值；当 H_β形成在一定高度（1000 公里）以上时，此模型下任何一组参数(a,b)预言的光球和色球磁元半强宽值都无法同时符合观测的光球磁元和色球磁元半强宽值，理论计算的光球磁元半强宽与色球磁元半强宽之比总是小于观测值。

6．2 日面边缘观测结果与理论的比较

6．2．1 观测结果

1．大部分日面边缘的光球宁静区磁元没有表现出极性反转对结构，这说明宁静区磁流管并没有较强的水平分量（第二章结论 1）。

2．日面边缘的色球纵向磁图反映出宁静磁元在色球层的水平分量亦不大（第三章结论 4）。

6．2．2 理论预计

Athay(1981)[1]模型预言：在 b 较大的情况下，在日面边缘的各个层次（z=0 以上 100 公里、200 公里、500 公里、1000 公里处），我们都应该能看到由两个不同极性组成的反映了磁场水平分量的极性反转对。当 b 较小时，我们也应该在低层次（z=0 以上 100 公里、200 公里、500 公里处）看到极性反转对（第四章结论 4）。

6．2．3 观测与理论的比较

理论预言我们将在光球层（z=0 以上 100 公里、200 公里处）看到极性反转对；当 b 较大时，在色球层（z=0 以上 1000 公里处）也应看到极性反转对。而在日面西边缘的观测却表明，在光球和色球层都极少发现极性反转对。这说明在我们观测的日面西边缘，实际的磁流管并没有表现出理论预言的磁流管扩张而应表现出的磁场水平分量。

6．3 总结

1．日面中心观测对理论模型的限制依赖于对 H_β谱线形成高度的估计。当 H_β谱线形成在 1000 公里以上时，观测将对理论模型形成一定的冲击。
2．在日面西边缘没有观测到理论模型预言的极性反转对。

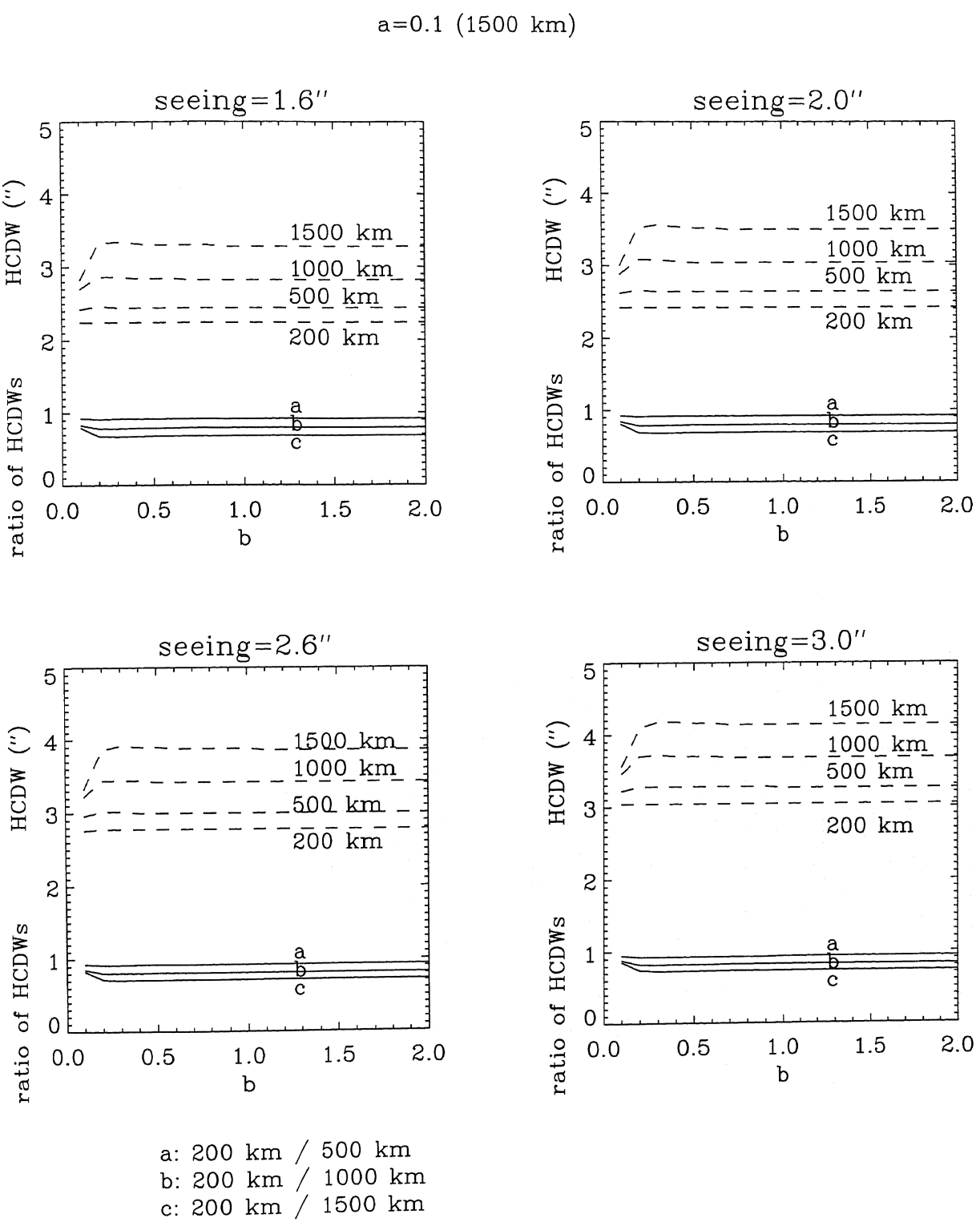

Fig.6.1 Calculated HCDWs (dashed lines) and ratios of HCDWs (solid lines) under four different seeing conditions for magnetic parameter a=0.1. The X-axis is the value of magnetic parameter b. The Y-axis is the calculated HCDWs in unit of arcsec (dashed lines) and ratios of HCDWs (solid lines) respectively.

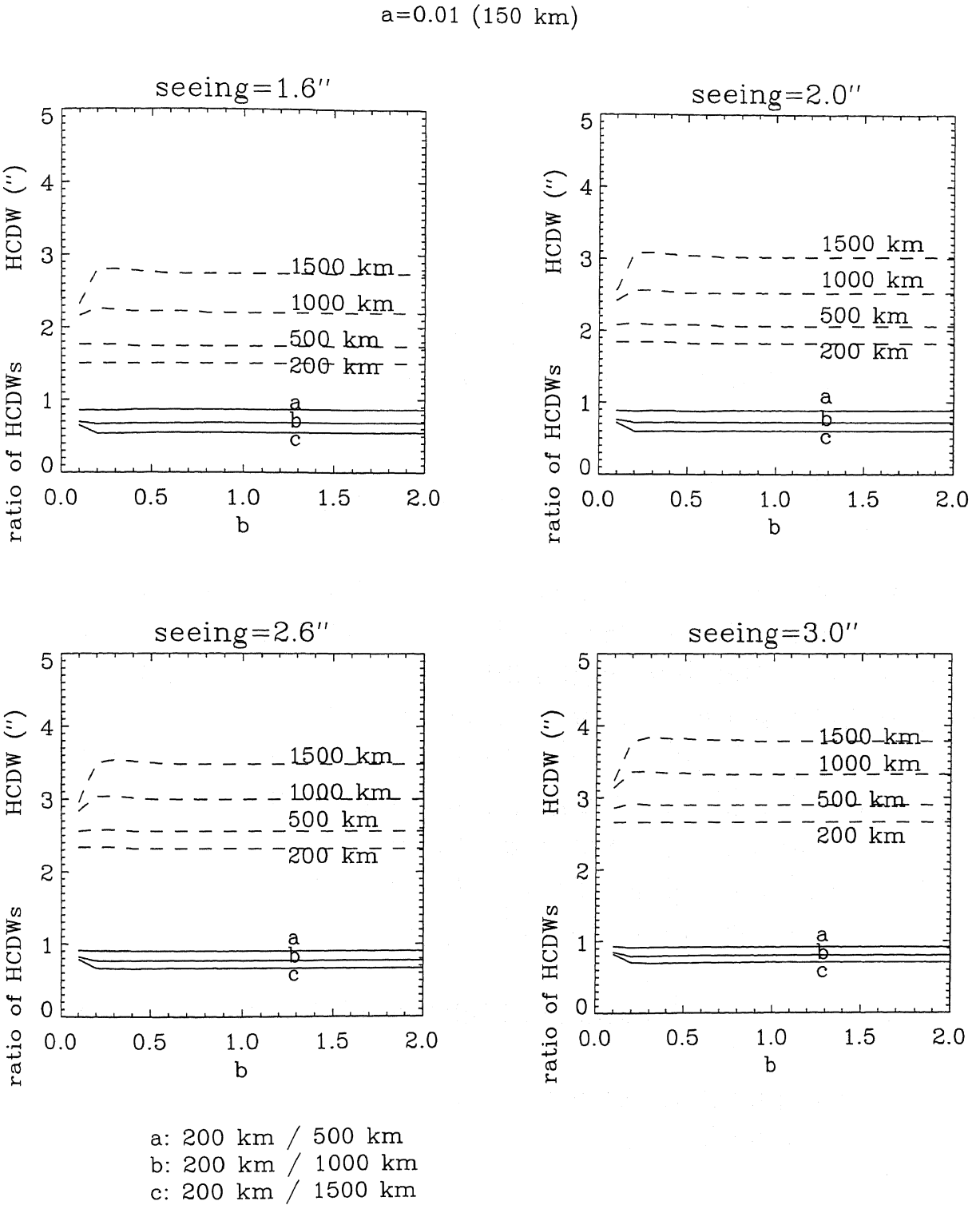

Fig.6.2 Calculated HCDWs (dashed lines) and ratios of HCDWs (solid lines) under four different seeing conditions for magnetic parameter a=0.01. The X-axis is the value of magnetic parameter b. The Y-axis is the calculated HCDWs in unit of arcsec (dashed lines) and ratios of HCDWs (solid lines) respectively.

第七章 日冕及过渡区磁场的可能形式

7.1 紫外及软X射线像与日冕及过渡区磁场的关系

由于磁冻结效应，太阳日冕及过渡区中的热等离子体被认为基本上是冻结在磁场中的。因此，太阳日冕及过渡区的软 X 射线和远紫外像通常被认为反映了太阳磁场在日冕及过渡区的结构。从光球磁场外推而得的日冕磁场结构与日冕软 X 射线像符合得很好的事实也从另一方面证实了这种假设的合理性[1]。

7.2 太阳过渡区及日冕的紫外观测

1998 年 4 月，美国发射了主要用于太阳过渡区及日冕观测的 TRACE 卫星。它通过对一系列谱线进行同时观测，力图了解日冕及过渡区物理。

在这些谱线中，利用 FeIX171A 谱线拍摄的照片首次得到了高分辨率的太阳过渡区及日冕的远紫外像。这些照片清晰地反映出太阳高层大气中存在着极为精细的结构，而并非如理论预言的那样是均匀的一片。这种精细结构几乎反映在所有的这个波段的照片中。如图 7.1-7.6 即为 TRACE 卫星在 1998 年 9 月 11 日—16 日对怀柔编号为 127 的活动区进行的不同日面处的观测。虽然在几天的演化中，活动区上空的日冕结构的整体形态发生了很大变化，但太阳高层大气中存在着精细结构这一特征却始终未变。

7.3 紫外观测与怀柔光球磁场观测的比较研究

我们将 1998 年 9 月 15 日 TRACE 卫星 FeIX 171 埃波段拍摄的怀柔编号为 127 的活动区上空的远紫外像与同一时刻怀柔太阳磁场望远镜拍摄的太阳光球磁图进行了比较。图 7.7 即为 TRACE 卫星 171 埃波段拍摄的紫外像（黑白图）与怀柔太阳磁场望远镜拍摄的太阳光球磁图（轮廓图）比较的结果。黑色十字显示了怀柔光球磁图中磁元的中心位置。由于 TRACE 远紫外像的视场为 512″×512″，而怀柔光球磁图的视场为 300″×200″，所以只有

部分远紫外像有对应的光球磁场观测。

如果我们认为远紫外像中的亮结构基本上反映了磁场在太阳高层大气中的磁结构，则从图 7.7 可以看出，太阳磁场在太阳高层大气中基本上是由宽度不大变化的细纤维组成的。如图 7.8b 中的细纤维 A 即为图 7.8a 中方框所示位置处的一条细纤维。图 7.8c 显示了此纤维不同处（从 1 到 13，位置显示在图 7.8b 中）的强度轮廓。从这些轮廓中可以看出，细纤维的结构基本没变，其宽度亦基本保持不变。

这些细纤维在光球层上的足点与怀柔磁图观测到的光球磁元位置对应的很好，亦说明这些细纤维确实可能反映了磁流管从光球向高空扩展的状况。因此，远紫外像中细纤维的宽度不变，则可能反映了磁场在小磁流管中扩展不大。虽然由于这些细纤维相对于太阳表面的倾角各异，而使得活动区上空的太阳磁场从整体上看起来好象在扩展,但实际上组成整体磁场的各个细纤维（我们认为代表组成整体磁场的小磁流管）的宽度基本不变。

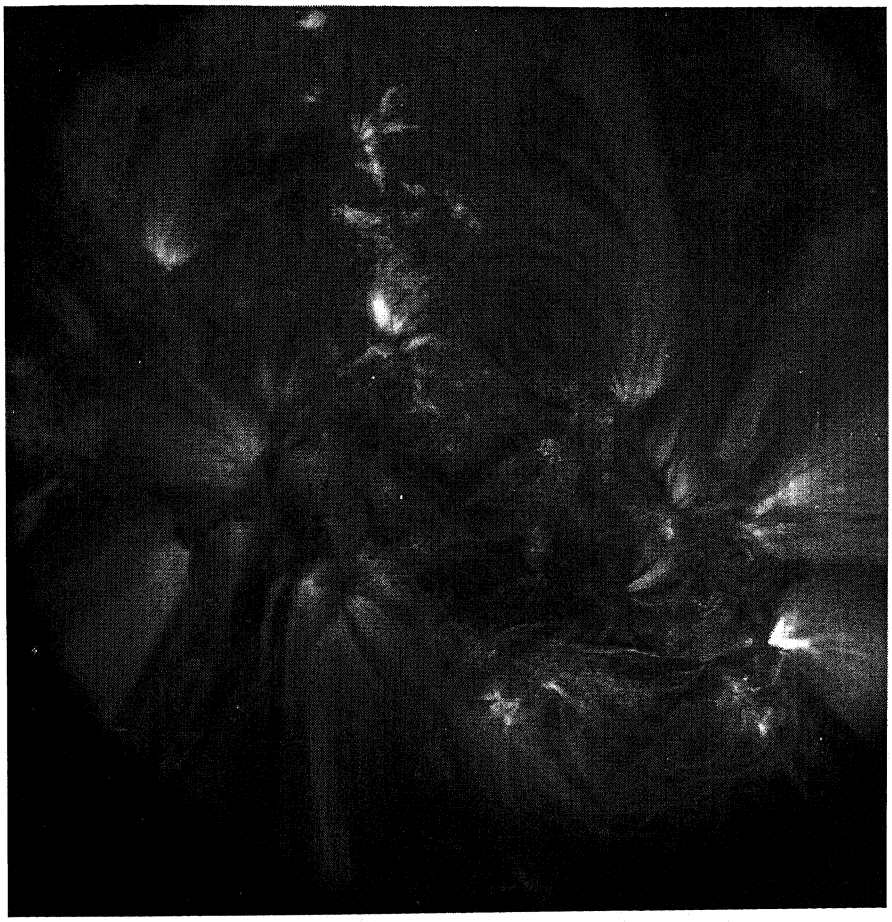

Fig.7.1 Ultraviolet image (in a narrow wavelength band around the FeIX171 line) of the solar corona from TRACE satellite, taken upon the active region (Huairou number 127) on September 11 1998.

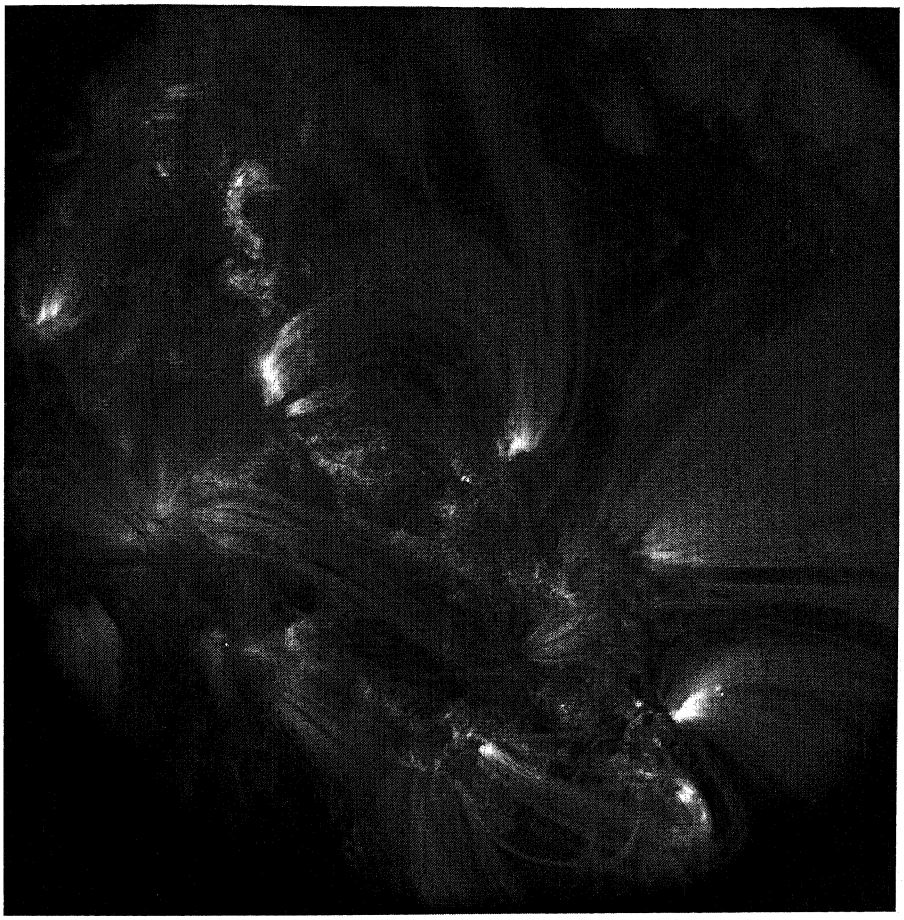

Fig.7.2 Ultraviolet image (in a narrow wavelength band around the FeIX171 line) of the solar corona from TRACE satellite, taken upon the active region (Huairou number 127) on September 12 1998.

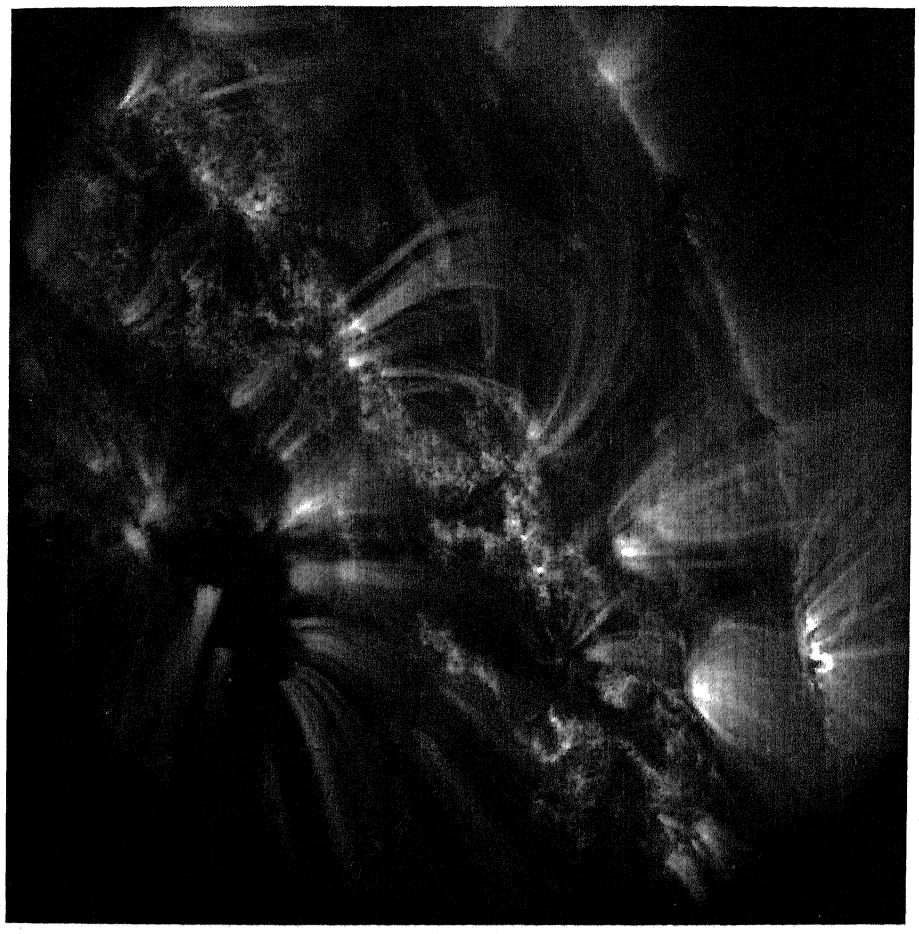

Fig.7.3 Ultraviolet image (in a narrow wavelength band around the FeIX171 line) of the solar corona from TRACE satellite, taken upon the active region (Huairou number 127) on September 13 1998.

Fig.7.4 Ultraviolet image (in a narrow wavelength band around the FeIX171 line) of the solar corona from TRACE satellite, taken upon the active region (Huairou number 127) on September 14 1998.

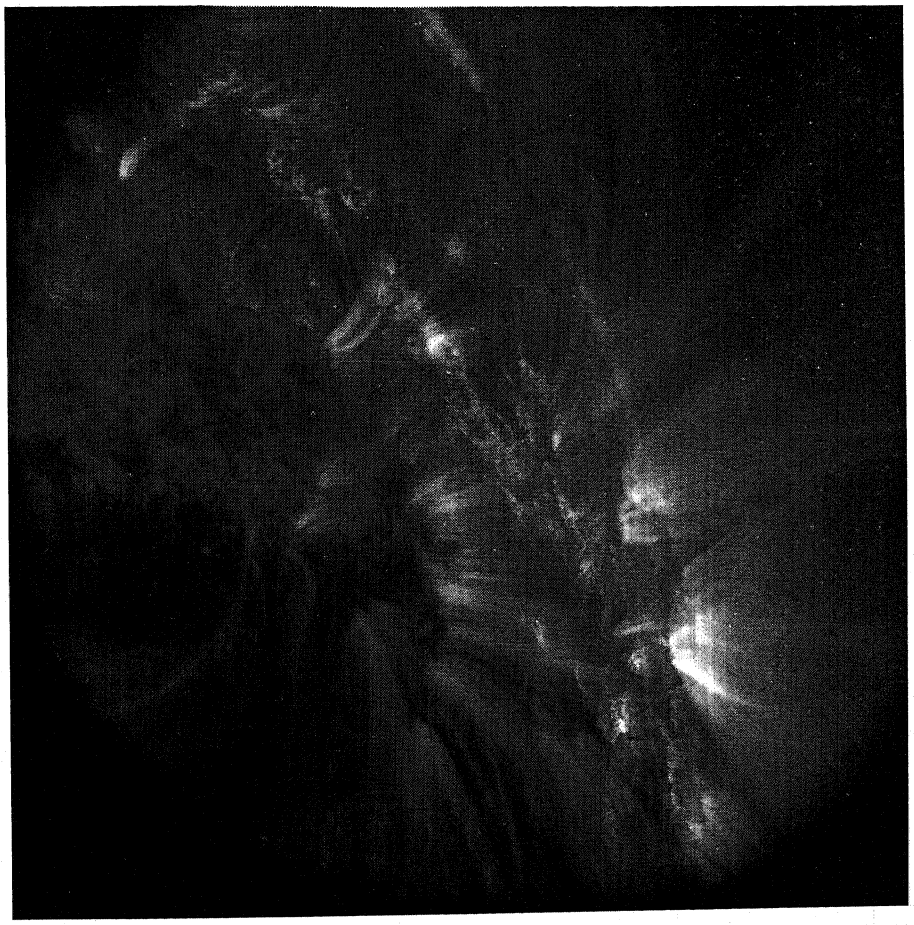

Fig.7.5 Ultraviolet image (in a narrow wavelength band around the FeIX171 line) of the solar corona from TRACE satellite, taken upon the active region (Huairou number 127) on September 15 1998.

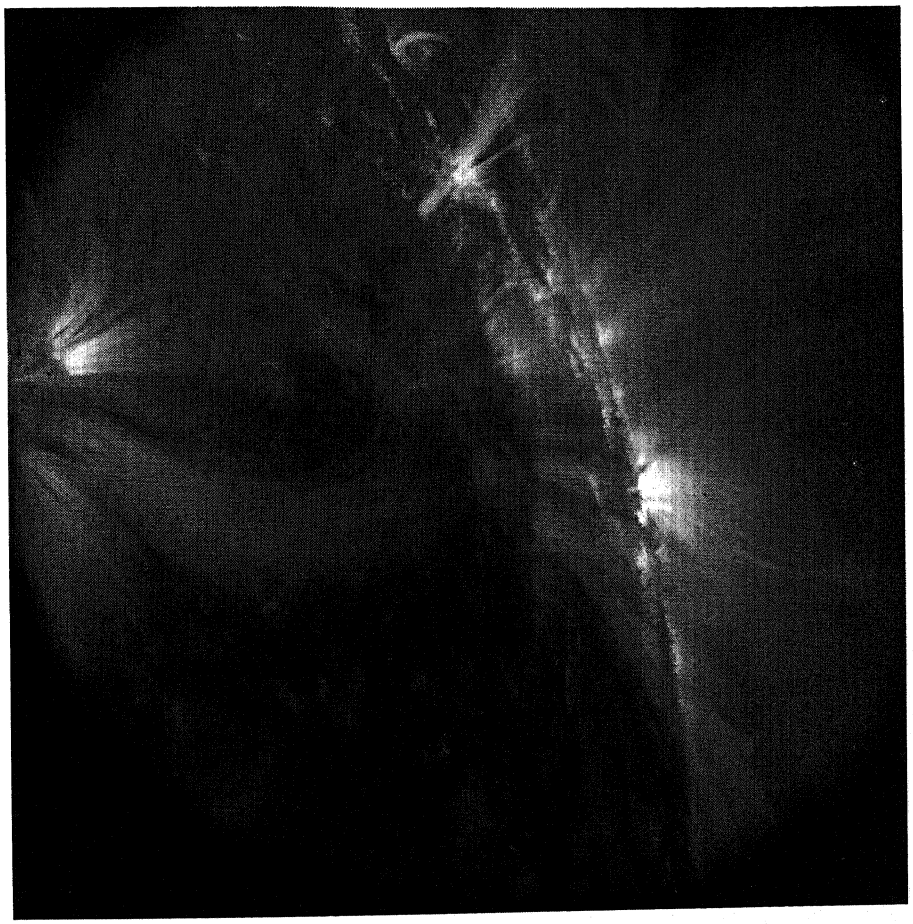

Fig.7.6 Ultraviolet image (in a narrow wavelength band around the FeIX171 line) of the solar corona from TRACE satellite, taken upon the active region (Huairou number 127) on September 16 1998.

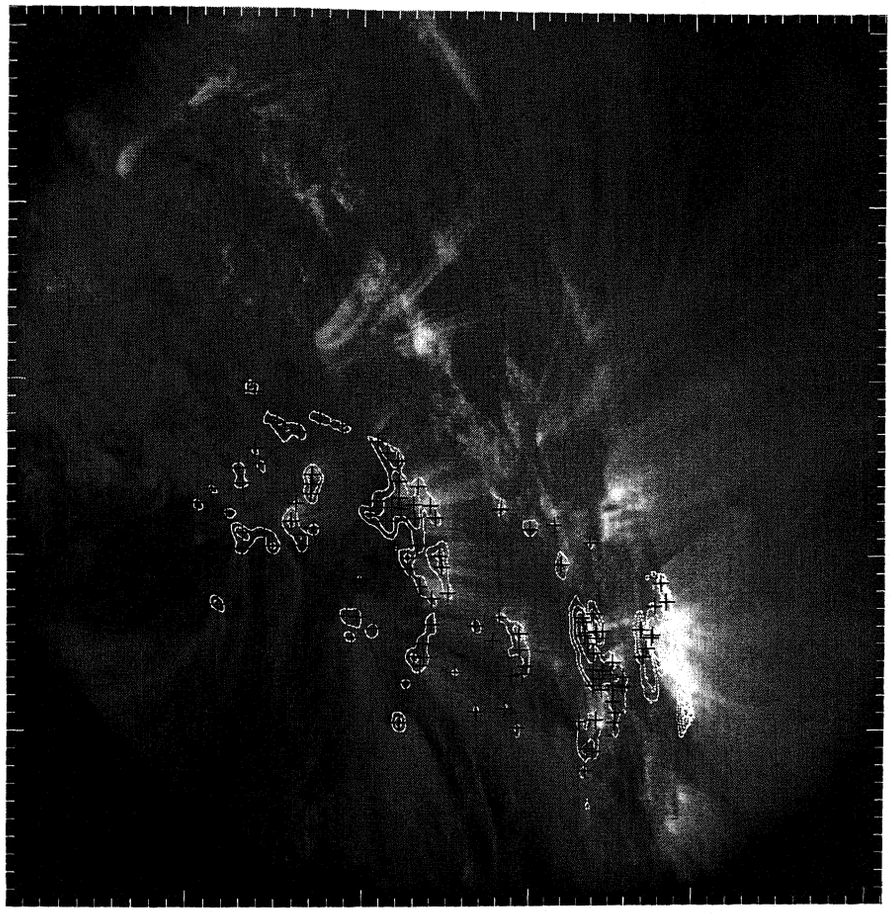

Fig.7.7 Utravoilet image of the solar corona from TRACE satellite with the Huairou solar photospheric magnetogram (contours), taken upon the active region (Huairou number 127) on September 15 1998.

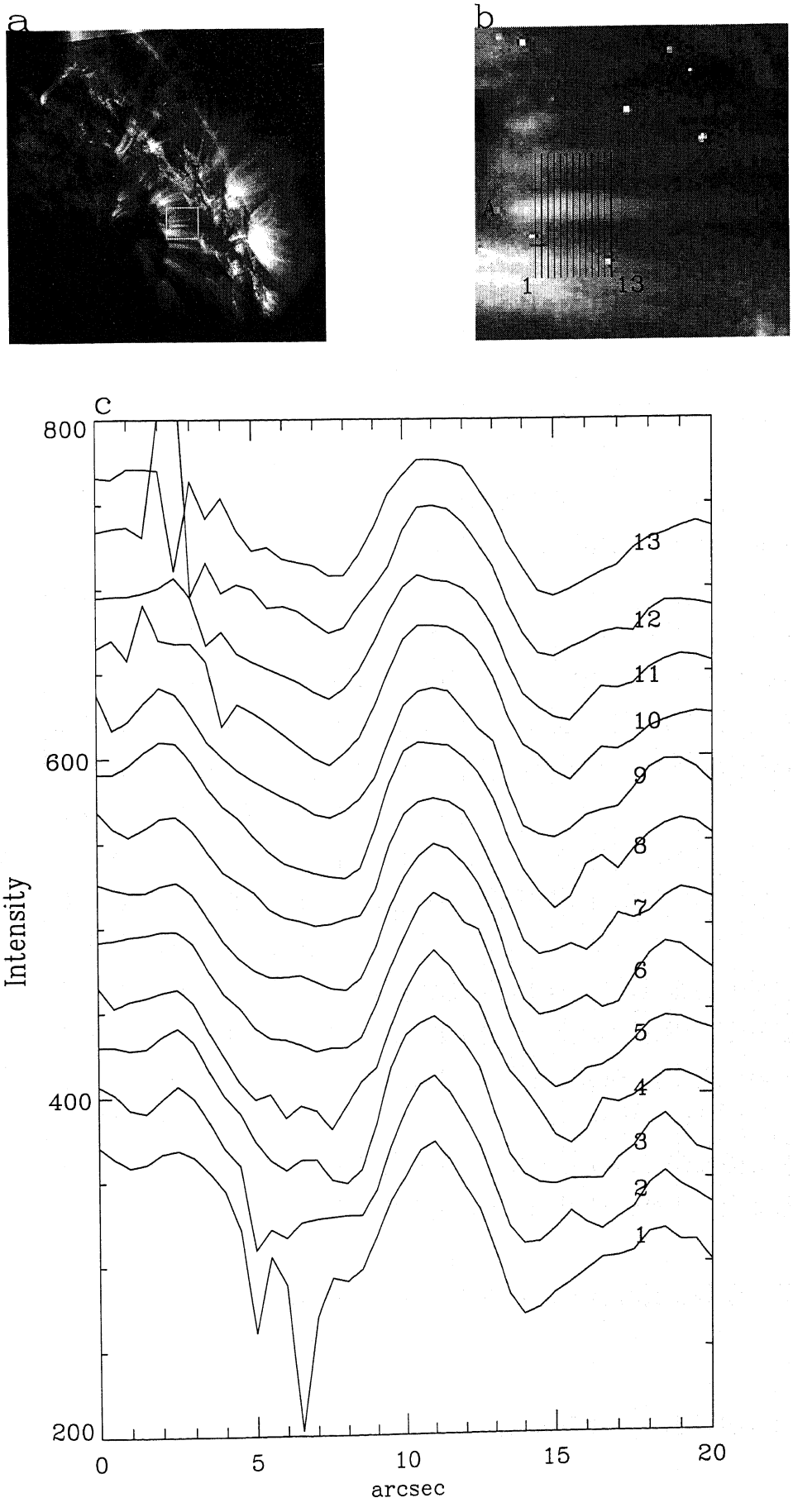
a
b
1
13
c
800
600
400
200
Intensity
0
5
10
15
20
arcsec
13
12
11
10
9
8
7
6
5
4
3
2
1

Fig.7.8.

第八章 太 阳 磁 场 结 构 的 纤 维 树 模 型

8.1 太阳磁场结构的纤维树模型

综合以上观测事实和理论分析，我们发现，磁场的三维空间结构存在着以下的难以用伞盖模型，特别是低伞盖高度的伞盖模型来描述的特征：

1．从日面中心到边缘的宁静区光球磁场观测表明，宁静区磁元在光球层的水平分量很小,没有形成在活动区附近观测到的伞盖结构。

2．采用超深积分方法得到的高信躁比的色球宁静区磁图表明，色球层磁元与光球层磁元的结构非常相似，宁静区磁元在色球层的水平分量亦很小。

3．将太阳过渡区及日冕的紫外观测与怀柔光球磁图的比较发现，紫外像中亮丝结构的根部位于光球磁元中心，紫外像中亮纤维结构的宽度不变可能反映了磁场在从光球向日冕发展过程中扩散不大。最近 Thomas 在 Nature 上发表的文章也提到了日冕磁场呈现精细结构这一现象[1]。

4．张洪起[2]在活动区色球磁场中也发现了类似的细纤维结构。他发现活动区附近的太阳磁场在从光球向色球延伸的过程中，是以连续向外延伸的纤维形式向外扩展的。

5．从光球磁场外推而得的日冕磁场结构与日冕软 X 射线像符合得很好的事实证实了这种外推方法的合理性[3]，而这种外推方法却发现太阳日冕磁场结构存在着多样性，在日冕磁场中既存在着高环又存在着低环[4]。

6．对日面边缘的光球磁场的观测亦发现宁静区的太阳磁场结构也存在着多样性。太阳赤道附近宁静区磁元的水平分量较小，而南北极附近磁元则存在着一定的水平分量。

7．利用色球谱线对色球磁场进行的光谱诊断亦发现观测结果难以用伞盖型磁场结构来解释[5]。

因此，我们提出了一种不同于伞盖模型的描述太阳大气中磁场结构的

模型——太阳大气中磁场结构的纤维树模型。我们认为，不仅在光球层，在太阳高层大气中，磁场也是不均匀的。磁流管在从太阳大气低层（光球层）向高层（日冕）扩展时，单个磁流管的磁通量结构变化不大。宁静区和活动区的区别在于：在宁静区，由于每个磁流管基本上垂直于日面，从而形成如森林耸立的纤维树结构。在活动区，由于每个磁流管相对于日面的倾角不同，而且单个磁流管相对于日面的倾角在向高空扩展中可能发生变化，从而使得活动区上空的太阳磁场从整体上看好象在扩展而形成开放状的纤维树结构。

8.2 对日冕及色球加热的意义

如果磁流管的大小在扩展过程中确实变化不大，则这些磁流管将对色球和日冕的加热意义重大。Fawzy[6]等人的工作表明，横截面不变的磁流管将被十分有效地加热，从而对色球及日冕的加热作出贡献。

参 考 文 献

第一章

[1] Parker, 1955, ApJ, 122, 293.

[2] Spruit, H.C., 1981, In: Jordan S. (eds) The Sun as a Star, p.385

[3] Gabriel, A.H., A magnetic model of the solar transition region, 1976, Phil. Trans. R. Soc. London, A281, 339.

[4] Parker, E.N., Hydraulic concentration of magnetic fields in the solar photosphere VI. Adiabatic cooling and concentration in downflows, 1978, ApJ, 221, 368.

[5] Athay, R.G., Chromosphere-corona transition region models with magnetic field and fluid flow, 1981, ApJ, 249, 340.

[6] Athay, R.G., Responses of transition region models to magnetic field geometry and downflow velocities, 1982, ApJ, 263, 982.

[7] Giovanelli, R.G., An exploratory two-dimensional study of the coarse structure of network magnetic fields, 1980, Solar Physics, 68, 49.

[8] Giovanelli, R.G., Sunspots geometry and pressure balance, 1982, Solar Physics, 80, 21.

[9] Giovanelli, R.G. & Jones, H.P., The three-dimensional structures of atmospheric magnetic fields in two active regions, 1982, Solar Physics, 79, 267.

[10] Jones, H.P. & Giovanelli, R.G., Magnetograph response to canopy-type fields, 1982, Solar Physics, 79, 247.

[11] Jones, H.P. & Giovanelli, R.G., Magnetic canopies in unipolar regions, 1983, Solar Physics, 87, 37.

[12] Johns H.P., Magnetic canopies and models of the solar chromosphere, 1985, In: Lites B.W. (eds) Chromospheric Diagnostics and Modelling, National Solar Obs., Sacramento Peak, New Mexico, p.175.

[13] Solanki, S. K., Montavon, C. A. P. & Livingston, W., Infrared

lines as probes of solar magnetic features VII. On the nature of the Evershed effect in sunspots, 1994, A&A., 283, 221.
[14] Keppens, R. & Pillet, V.M., The magnetic structures of pores and sunspots derived from Advanced Stokes Polarimeter data, 1996, A&A, 316, 229.
[15] Adams, M., Solanki, S.K., Hagyard, M. & Moore, R.L., A search for sunspot canopies using a vector magnetograph, 1993, Solar Physics, 148, 201.
[16] Solanki, S.K., Ruedi, I. & Livingston, W., Infrared lines as probes of solar magnetic features V. The magnetic structure of a simple sunspot and its canopy, 1992, A&A, 263, 339.
[17] Solanki, S.K. & Steiner, O., How magnetic is the solar chromosphere?, 1990, A&A, 234, 519.
[18] Azer, U. & Galloway, D.J., A model for the magnetic field above supergranules, 1983, MNRAS, 203, 637.
[19] Fiedler, R.A.S. & Cally, P.S., Force and energy balance in the transition region network, 1990, Solar Physics, 126, 69.
[20] Pneuman, G.W., Solanki, S.K. & Stenflo, J.O., Structure and merging of solar magnetic fluxtubes, 1986, A&A, 154, 231.
[21] 艾国祥、胡岳风，太阳磁场望远镜的工作原理，1986，天文学报，27，173.
[22] 艾国祥、李威、张洪起，FeIλ5324.19A 在磁场中的形成和太阳磁场望远镜的理论定标，1982，天文学报，23，39.
[23] Wang, T.J., Ai, G.X. & Deng, Y.Y., Calibration of nine-channel solar magnetic field telescope. I. The methods of the observational calibration, 1996, 北京天文台台刊, 28, 31.
[24] Deng, Y.Y., Ai, G.X., Wang, J.S., Song, G.F., Zhang, B. & Ye, X.M., Report on test observations with the multi-channel solar telescope, 1997, Solar Physics, 173, 207.

第二章

[1] Zirin, H., Astrophysics of the Sun, Cambridge University Press,

1988, 128 页.
[2] Homann, T., Kneer, F. & Makarov, V.Z., Spectro-polarimetry of polar faculae, 1997, Solar Physics, 175, 81.
[3] Zhang, L.D., Zirin, H. & Marquette, W.H., Comparison of polar and equatorial magnetic fields near sunspot minimum, 1997, Solar Physics, 175, 59.

第三章

[1] 艾国祥、李威、张洪起, FeIλ5324.19A 在磁场中的形成和太阳磁场望远镜的理论定标, 1982, 天文学报, 23, 39.
[2] Wang, T.J., Ai, G.X. & Deng, Y.Y., Calibration of nine-channel solar magnetic field telescope. I. The methods of the observational calibration, 1996, 北京天文台台刊, 28, 31.
[3] Wang, J., Wang, H., Tang, F., Lee, J.W. & Zirin, H., Flux distribution of solar intranetwork magnetic fields, 1995, Solar Physics, 160, 277.
[4] Durney, B.R., Young, D.S. & Roxburgh, I.W., 1993, Solar Phyics., 145, 207.
[5] Petrovay, K. & Szakaly, G., 1993, A&A, 274, 543.
[6] Wang, H., Tang, F., Zirin, H. & Wang, J., The velocities of intranetwork and network magnetic fields, 1996, Solar Physics, 165, 223.
[7] Zhang, J., Lin, G.H., Wang, J., Wang, H. & Zirin, H., Lifetime of intranetwork magnetic elements, 1998, Solar Physics, 178, 245.
[8] Schrijver, C.J., Title, A.M., et al., Large-scale coronal heating by the small-scale magnetic field of the Sun, 1998, Nature, 394, 152.
[9] Zirin, H., Astrophysics of the Sun, Cambridge University Press, 1988, 128 页.

第四章

[1] Athay, R.G., Chromosphere-corona transition region models with magnetic field and fluid flow, 1981, ApJ, 249, 340.
[2] Solanki, S.K. & Steiner, O., How magnetic is the solar chromosphere?,

1990, A&A, 234, 519.
[3] Azer, U. & Galloway, D. J., A model for the magnetic field above supergranules, 1983, MNRAS, 203, 637.
[4] Fiedler, R. A. S. & Cally, P. S., Force and energy balance in the transition region network, 1990, Solar Physics, 126, 69.
[5] Pneuman, G. W., Solanki, S. K. & Stenflo, J. O., Structure and merging of solar magnetic fluxtubes, 1986, A&A, 154, 231.
[6] Hagyard, M. J., Changes in measured vector magnetic fields when transformed into heliographic coordinates, 1987, Solar Physics, 107, 239.
[7] Venkatakrishnan, P., Hagyard, M. J. & Hathaway, D. H., Elimination of projection effects from vector magnetograms: The pre-flare configuration of active region AR4474, 1988, Solar Physics, 115, 125.

第五章

[1] 艾国祥、胡岳风，太阳磁场望远镜的工作原理，1986，天文学报，27，173.
[2] 艾国祥、李威、张洪起，FeIλ5324.19A 在磁场中的形成和太阳磁场望远镜的理论定标，1982，天文学报，23，39.
[3] 张洪起，在太阳磁场大气中 FeI5324.19A 谱线的形成深度，1986，天体物理学报，6，295.
[4] Lin, Y. Z., Zhang, H. Q. & Zhang, W. J., A solar flare in the FeI5324 line on 24 June 1993, 1996, Solar Physics, 168, 135.
[5] Liu, Y., Wang, J. X., Yan, Y. H. & Ai, G. X., Gradients of the line-of-sight magnetic fields in active region NOAA6659, 1996, Solar Physics, 169, 79.
[6] 张洪起、艾国祥，氢 H_β 谱线在色球磁场大气中的形成，1986，天文学报，27，217.
[7] Zhang, H. Q. & Zhang, M., The chromospheric evidence of magnetic flux model in the quiet Sun, 北京天文台台刊(增刊, 1998, No. 4), p. 6.
[8] Allen, C. W., Astrophysical Quantitues, 1963, London:Athlone Press.

[9] Vernazza, J. E., Avrett, E. H. & Loeser, R., Structure of the solar chromosphere I. Basic computations and summary of the results, 1973, ApJ, 184, 605.
[10] White, O. R. & Wilson, P. R., On the height of formation of H_alpha in the solar chromosphere, 1966, ApJ, 146, 250.
[11] Vernazza, J. E., Avrett, E. H. & Loeser, R., Structure of the solar chromosphere III. Models of the EUV brightness components of the quiet Sun, 1981, ApJ. Suppl., 45, 635.
[12] Zhang, H. Q., Magnetic configuration of a sunspot region using H_β line, 1996, A&A Suppl, 119, 205.

第六章

[1] Athay, R. G., Chromosphere-corona transition region models with magnetic field and fluid flow, 1981, ApJ, 249, 340.

第七章

[1] Wang, H. N., Sakurai, T. & Yan, Y. H., Enhanced coronal heating and 3D solar magnetic fields in AR7321, 1998, Advances in Space Research, in press.

第八章

[1] Thomas, T. H., The Sun at the small scales, 1998, Nature, 396, 114.
[2] Zhang, H. Q., Magnetic configuration of a sunspot region using H_β line, 1996, A&A Suppl, 119, 205.
[3] Wang, H. N., Sakurai, T. & Yan, Y. H., Enhanced coronal heating and 3D solar magnetic fields in AR7321, 1998, Advances in Space Research, in press.
[4] Wang, T. J., Wang, H. N. & Qiu, J., Two dimensional sigular points in an observed transverse field in solar active region NOAA7321, 1999, A&A, 342, 854.
[5] Degl'innocenti, Evidence against turbulent and canopy-like magnetic fields in the solar chromosphere, 1998, Nature, 392, 256.

[6] Fawzy, D. E, Ulmschneider, P. & Cuntz, M., The heating of solar magnetic flux tubes I. Adiabatic longitudinal tube waves, 1998, A&A, 336, 1029.

其它：

[1] 汪景秀，博士论文：太阳表面小尺度磁场的观测特性，1985.
[2] 王华宁，博士论文：太阳活动区磁场非势性与分形特征，1994.
[3] 刘扬，博士论文：太阳大气中三维磁场结构的研究，1996.
[4] 邓元勇，博士论文：High Resolution observations with multi-channel solar telescope, 1997.
[5] 王同江，博士论文：太阳活动区磁场的观测研究，1998.
[6] 包曙东，博士论文：太阳活动区光球电流螺度的观测研究，1998.
[7] 张军，博士论文：网络内磁场的研究，1998.

致 谢

在此论文即将完成之际，我首先要感谢我的导师张洪起教授。他富于悟性的思维方式给了我很大的启发。也许，多年的科研训练使我具备了一些数据处理的技巧，但张洪起教授的对事物物理本质的直觉把握却使我对科研的理解又上了一个层次。

我还要感谢艾国祥院士和怀柔集团的全体工作人员。是艾国祥院士一手发展起来的太阳磁场望远镜给了我用武之地。是艾国祥院士带出的怀柔集团的学术风气给了我不少有益的熏陶。在共同的讨论中，不少同事给我提出了很好的意见和建议，帮我出谋划策。怀柔基地的观测助手和行政人员在我攻读学位期间也给了我不少帮助。

我对我母亲的感激之情是难以用文字表达的。如果不是她几年来帮助我照料年幼的儿子和分担了大部分家务，我的博士学位攻读计划也许早就流产了。从更长远的角度说，是她在那个重男轻女思想尚很严重的时代，就在我幼小的心灵里种下了自强不息的种子。

我还要感谢那些知名和不知名的批评者们。他们的批评正是推动我工作不断向前的动力。如本论文的第五章就是针对“H_β的形成深度到底是多少？能否对伞盖模型作出判断？”的思考。而本论文的第六章就是针对“半宽比较是否能对伞盖模型作出判断？也许伞盖模型的散只是边缘散而中心不散呢？”的批评而作出的探讨。本论文的第七章是针对“即使在色球层不散，到日冕层会不会散呢？”的问题作出的估计。可以说，我们的工作从最开始的日面中心和边缘深积分光球和色球观测，发展到现在的从理论探讨到观测分析、从地面观测到空间资料分析的多方位的探讨，是一步步地在各种意见的推动下进行的。虽然我相信，我的工作还会存在着漏洞，还会有各种疑问意见以给我们继续发展的空间，但毕竟我对问题的理解比以前深入多了。不同学术观点的争鸣可能正是通向科学发现的入口，为此，我要特别感谢批评者们对我的帮助和推动。

我还要感谢陈建生院士。虽然我在 BATC 这块土地上的耕耘尚未结出应

该收获的果实，但在 BATC 课题的几年里，我对天文仪器和天文观测方法的理解有了一定的提高，我的数据处理能力得到了系统的发展。这一切都为我今后的发展打下了基础。在此特别感谢陈建生院士给我的指导和锻炼。

我还要感谢林元章教授在我论文写作方面给予的帮助。他细致入微的审阅帮我纠正了许多用法的不规范。

附录一：发表文章目录

太阳物理：

1. 题目：Different magnetic features between solar polar and equatorial magnetic fields
   作者： Zhang Mei & Zhang Hongqi
   刊物： Astro.Astrophys., 1999, accepted。

2. 题目：A comparison between photospheric and chromospheric quiet-Sun magnetograms
   作者：Zhang Mei & Zhang Hongqi
   刊物：Solar Physics, 1999, accepted。

3. 题目：Can different canopy height values consistent?
   作者： Zhang Mei & Zhang Hongqi
   刊物： Solar Physics, 1999, submitted。

4. 题目：A study of structure of small-scale magnetic flux tubes (I) Solar disk center observation
   作者： Zhang Mei & Zhang Hongqi
   刊物： Proceeding of the sixth workshop on solar magnetic and velocity field, 1998, p.85。

5. 题目：A study of structure of small-scale magnetic flux tubes (II) Solar center-to-limb observation
   作者： Zhang Mei & Zhang Hongqi
   刊物： Publ. Beijing Astronomical Observatory, 1999, in press.

6. 题目：太阳宁静区磁场空间结构
   作者：张枚、张洪起
   刊物：《太阳 23 周峰年研讨会会议文集》，1999，在印刷。

7. 题目：太阳宁静区色球磁场观测
作者：张枚、张洪起
刊物：空间科学学报,1999, 已接收。

8. 题目：The chromospheric evidence of magnetic flux model in the quiet Sun
作者：Zhang Hongqi & Zhang Mei
刊物：Proceeding of the sixth workshop on solar magnetic and velocity field, 1998, p.6。

9. 题目：A survey of flares and current helicity in active regions
作者：Bao Shudong, Zhang Hongqi, Ai Guoxiang & Zhang Mei
刊物：Astro.Astrophy.Suppl.Ser., 1999, accepted。

10. 题目：1997年3月9日漠河日全食期间的太阳磁场观测
作者：张洪起、张枚等
刊物：《太阳与近地环境》,1999，在印刷。

观测宇宙学：

1. 题目：用多色测光方法发现红移 z=3.3 类星体
作者：张枚、陈建生等
刊物：《自然科学进展》(中英文)，1998，第8卷，243页。

2. 题目：A calibration method for wide field multicolor photometer systems
作者：Xu Zhou, Chen Jiansheng, Xu Wen & Zhang Mei
刊物：PASJ, 1999, in press.

3. 题目：星族综合模型与星系的颜色演化,
作者：徐璧、俞允强、张枚、周旭、陈建生
刊物：《天体物理学报》,1997，第17卷，第一期，135页。

4. 题目：广角测光系统的一种色定标方法
作者：周旭、徐璧、张枚、陈建生
刊物：《北京天文台台刊》,1997，第二期，142页。

射电观测：

1. 题目：Faint radio sources with peaked spectra I. VLA observations of a new sample with intermediate flux-densities
   作者： I.A.U. Snellen, Zhang Mei, et al.
   刊物： Astro.Astrophys., 1995, Vol. 300, p.359。

星系形成和演化：

1. 题目：球状星团的金属丰度特征与其恒星形成史
   作者：张枚、马耳
   刊物：《天体物理学报》, 1992, 第 12 卷, 第四期，349 页。

2. 题目：Globular clusters' metallicity and their star formation history,
   作者：Zhang Mei & Ma Er
   刊物：Proceeding of 3rd DAEC meeting on The feedback of chemical evolution on stellar content of galaxies, 1992, p.283。

3. 题目：球状星团的致密度及其演化
   作者：张枚、马耳
   刊物：《天体物理学报》, 1991, 第 11 卷, 第二期，128 页。

4. 题目：Metallicity of disk stars and a possible scenario of initial enrichment
   作者：Zhang Mei & Ma Er
   刊物：Proceeding of Beijing workshop on supernovae and their remnants, 1991, p.143。

5. 题目：球状星团的性质和演化(II): 球状星团的动力学和形成过程
   作者：马耳、张枚
   刊物：《天文学进展》, 1991, 第 9 卷, 第一期，22 页。

6. 题目：球状星团的性质和演化(I): 球状星团的年龄、分布和运动
   作者：马耳、张枚
   刊物：《天文学进展》, 1990, 第 8 卷, 第四期，317 页。

7. 题目：狐狸座 BW 星的周期分析
   作者：蒋世仰、张枚
   刊物：《天体物理学报》, 1989, 第 9 卷, 第四期，341 页。

附录二：部分文章全文

此处收录作者在攻读博士学位期间发表的部分文章全文。其中 2 篇为没有被收入本论文内容的、其他两方面工作的代表作，以作为对作者在攻读博士学位期间在其他两方面工作的说明。

1. Different magnetic features between solar polar and equatorial magnetic fields, Zhang Mei & Zhang Hongqi, Astro.Astrophys., 1999, accepted。

2. A comparison between photospheric and chromospheric quiet-Sun magnetograms, Zhang Mei & Zhang Hongqi, Solar Physics, 1999, accepted。

3. 用多色测光方法发现红移 z=3.3 类星体，张枚、陈建生等，《自然科学进展》（中英文），1998，第 8 卷，243 页。

4. Faint radio sources with peaked spectra I. VLA observations of a new sample with intermediate flux-densities, I.A.U. Snellen, Zhang Mei, et al., Astro.Astrophys., 1995, Vol. 300, p.359。

A&A manuscript no.
(will be inserted by hand later)

Your thesaurus codes are:
09 (06.13.1; 06.16.2)

ASTRONOM
AND
ASTROPHYS
August 1, 1999

Different magnetic features between solar polar and equatorial magnetic fields

M. Zhang and H.Q. Zhang

Beijing Astronomical Observatory, Chinese Academy of Sciences, Beijing 100080, China;
National Astronomical Observatories, Chinese Academy of Sciences, Beijing 100012, China

Received / Accepted

Abstract. Solar polar and equatorial photospheric (FeIλ5324.19Å line) magnetic fields have been observed using the vector video magnetograph at Huairou Solar Observing Station of Beijing Astronomical Observatory.

It is found from our observation that the magnetic fields of small-scale magnetic features near the solar poles are stronger than in quiet equatorial regions near the limb and that strong polar magnetic elements appear to have the same magnetic polarity as the general large-scale polar magnetic field, which is in agreement with previous results by Homann et al. (1997) and Zhang et al. (1997). It is also found from our observation that there are more opposite polarity magnetic pairs near the solar poles than in quiet equatorial regions near the limb.

Key words: Sun: magnetic fields – Sun: photosphere

1. Introduction

Recent studies show that polar magnetic fields differ from quiet equatorial magnetic fields near the limb in several ways. Zhang et al. (1997) found that polar fields are stronger than quiet equatorial fields, but no greater than equatorial limb data containing unipolar regions. Homann et al. (1997) found that polar faculae appear to have same magnetic polarity as the general polar magnetic field, while the equatorial faculae show both magnetic polarities. They also found that the sizes of polar faculae are larger than the sizes of equatorial faculae.

In this paper, we present our study on this kind of comparison. Observation is described in Section 2. Results and discussion are presented in Section 3. Conclusion is presented in Section 4.

2. Observation

The tunable birefringent filter of the solar telescope magnetograph at Beijing Astronomical Observatory can be aimed at different passbands for different observation & Hu 1986). For photospheric observations, the pass of the filter is set at -0.075Å from the FeIλ5324.19Å center for the measurement of longitudinal magnetic The equivalent width of FeIλ5324.19Å line is 0.344Å FWHM of the filter passband is 0.15Å.

Solar polar (southern and northern poles) and e torial (eastern and western limbs) photospheric mag fields have been observed on 11 July 1993. The fie view is about 6′ × 4′ for each field. The pixel resol of the CCD is about 0.7″ × 0.5″. The spatial resoluti each magnetogram is actually 2″ × 2″ after a smoo average of 3 × 4 pixels. The temporal resolution of magnetogram is 3 minutes.

3. Results and discussion

Photospheric longitudinal magnetograms near solar and equatorial limbs observed on 11 July 1993 are sented in Figure 1. The calibration of FeIλ5324.19Å in the magnetic field was made by Ai et al. (1982) estimating standard deviations (rms) of Stokes parar V in blank fields, the noise level is estimated as 3 C for each field.

To study these magnetograms quantitatively, w lected to study those magnetic elements whose peak tions are within a distance of 80" to each limb in each netogram. Magnetic elements are detected for those whose absolute peak flux densities are greater 10 C (> 3 × noise level). 215 magnetic elements are det in the described region near solar northern pole. 232 and 76 magnetic elements are detected respectively i described regions near solar southern pole, easterr western limbs. Peak positions of these magnetic eler are shown in Figure 2 by plus symbols over-plotte contour maps of each region. Some elements with absolute peak flux densities greater than 10 gauss (: noise level) are too small to have contours in the co maps (Figure 2), but these elements can be seen i black-white magnetograms (Figure 1).

Send offprint requests to: M.Zhang
Correspondence to: zhm@sun10.bao.ac.cn

3.1. Field strength

It is found that the magnetic elements near solar poles are stronger than in quiet equatorial regions near the limb and strong polar magnetic elements appear to have same magnetic polarity as the general large-scale polar magnetic field.

Numbers and ratios of magnetic elements with peak flux densities (B) in different ranges are archived in the four regions (northern pole, southern pole, eastern limb and western limb) and are listed in Table 1. Table 1a lists the number and ratio of magnetic elements whose peak flux densities are greater than 40 Gauss or smaller than -40 Gauss respectively in each region. Table 1b lists the number and ratio of magnetic elements whose peak flux densities are greater than 20 Gauss or smaller than -20 Gauss respectively in each region. Table 1c lists the number and ratio of magnetic elements whose peak flux densities are greater than 10 Gauss or smaller than -10 Gauss respectively in each region.

The ratio here is defined as the number in each number column divided by the total number of magnetic elements detected in that region. For example, there are totally 215 magnetic elements detected in the northern polar region. 3 magnetic elements in this region have their peak flux densities greater than 40 Gauss. This number corresponds to $3/215 = 1.4\%$ of magnetic elements in this region.

Table.1a Numbers and ratios of magnetic elements in different flux density ranges

	$B > 40$ Gauss		$B < -40$ Gauss	
	Number	Ratio	Number	Ratio
Northern pole	3	1.4%	0	0
Southern pole	0	0	6	2.6%
Eastern limb	0	0	2	1.2%
Western limb	0	0	0	0

Table.1b Numbers and ratios of magnetic elements in different flux density ranges

	$B > 20$ Gauss		$B < -20$ Gauss	
	Number	Ratio	Number	Ratio
Northern pole	22	10%	3	1%
Southern pole	11	5%	25	11%
Eastern limb	5	3%	13	8%
Western limb	1	1%	1	1%

Table.1c Numbers and ratios of magnetic elements in different flux density ranges

	$B > 10$ Gauss		$B < -10$ Gauss	
	Number	Ratio	Number	Ratio
Northern pole	128	60%	87	40%
Southern pole	117	50%	115	50%
Eastern limb	74	44%	96	56%
Western limb	50	66%	26	34%

From Table 1a we can find that: for those strong magnetic elements whose absolute peak flux densities are greater than 40 Gauss, the northern polar region is dominant for positive magnetic elements and the southern polar region is dominant for negative ones. This trend is also obvious in Table 1b. This is in agreement with Homann et al. (1997)'s conclusion that polar faculae appear to have same magnetic polarity as the general polar magnetic field.

Table 1a and 1b also show that the magnetic elements near solar poles are stronger than in quiet equatorial regions near the limb. The numbers and ratios of strong magnetic elements in polar regions are greater than in quiet equatorial region (western limb) and is in agreement with Zhang et al. (1997)'s conclusion.

The eastern limb region, which has an unipolar region nearby in the right side of the magnetogram of Figure 1c, shows a stronger field than the quiet western limb region. It has a field almost as strong as northern polar field although it is still weaker than the field near southern pole. This partially supports Zhang et al. (1997)'s conclusion that polar fields are not greater than equatorial fields containing unipolar regions. Our data show that one of polar fields (northern pole) is not evidently greater than equatorial field containing unipolar regions, although another polar field (southern pole) is.

Homann et al. (1997) found that the equatorial faculae show both magnetic polarities. This can also find evidence from our data. Our data show more balanced numbers of positive and negative magnetic elements among weak elements. Since quiet equatorial fields lack strong magnetic elements, they show more balanced numbers of positive and negative magnetic elements as a whole.

3.2. Opposite polarity magnetic pairs

It is also found that there are more opposite polarity magnetic pairs near solar poles than in equatorial regions near the limb.

Opposite polarity magnetic pairs are defined as those magnetic elements which have an opposite magnetic element nearby with the distance between these two elements less than 6". Numbers and ratios of magnetic elements with a paired opposite polarity magnetic element are presented in Table 2. The ratio definition is the same as in Table 1.

Table.2 Numbers and ratios of magnetic elements with a paired opposite polarity magnetic element

	$\mid B \mid \geq 20$ Gauss		$\mid B \mid \geq 10$ Gauss	
	Number	Ratio	Number	Ratio
Northern pole	9	4%	50	23%
Southern pole	23	10%	78	34%
Eastern limb	4	2%	21	12%
Western limb	0	0	4	5%

From Table 2, we can find that the numbers and ratios of magnetic elements with a paired opposite polarity magnetic element are greater in solar polar regions than in equatorial regions near the limb. This is different from the

finding of Homann et al. (1997). Presumably, it is because the sensitivity of the observations of these authors was lower than in our measurements, especially for detecting those close-by pairs as we detected here. There are also more opposite polarity magnetic pairs near the northern pole than near the eastern limb, even though the field strength near the northern pole is not so evidently greater than that near the eastern limb as discussed before. If we explain these opposite polarity magnetic pairs as evidences of horizontal components of the magnetic field, then this imply that magnetic elements in polar fields have greater horizontal components than those in equatorial fields.

4. Conclusion

From our observation and analysis, we find that:

1. The magnetic elements near solar poles are stronger than in quiet equatorial regions near the limb and strong polar magnetic elements appear to have same magnetic polarity as the general large-scale polar magnetic field, which are in agreement with previous results by Homann et al. (1997) and Zhang et al. (1997).

2. There are more opposite polarity magnetic pairs in solar southern and northern polar regions than in equatorial regions near eastern and western limbs, which disagree with the findings by Homann et al. (1997), possibly due to the higher sensitivity of our observations than those of these authors.

Acknowledgements. The authors would like to thank Prof. F. Kneer for his critical and helpful comments. Thanks our colleague Dr. Y.Y. Deng for his helpful discussion to promote this work. This research was supported by Chinese Academy of Sciences and National Science Foundation of China.

References

Ai G., Li W., Zhang H., 1982, Chinese Astronomy and Astrophysics, 6, 129

Ai G., Hu Y., 1986, Acta Astron. Sin, 27, 173

Homann T., Kneer F., Makarov V.I., 1997, Solar Physics, 175, 81

Zhang L.D., Zirin H., Marquette W.H., 1997, Solar Physics, 175, 59

Figure caption:

Fig.1. Photospheric longitudinal magnetograms near solar poles (Fig1a: northern pole; Fig1b: southern pole) and equatorial limbs (Fig1c: eastern limb; Fig1d: western limb) observed on 11 July 1993. The field of view is 330″ × 220″ for each field. Bright (dark) structures correspond to positive (negative) polarities.

Fig.2. Contours of photospheric magnetograms near solar poles (Fig2a: northern pole; Fig2b: southern pole) and equatorial limbs (Fig2c: eastern limb; Fig2d: western limb) observed on 11 July 1993. The field of view is 330″ × 220″ for each field. Solid (dashed) contours correspond to positive (negative) fields of 10,20,40,80,160 Gauss. Plus symbols indicate peak positions of magnetic elements in areas within 80" to each limb.

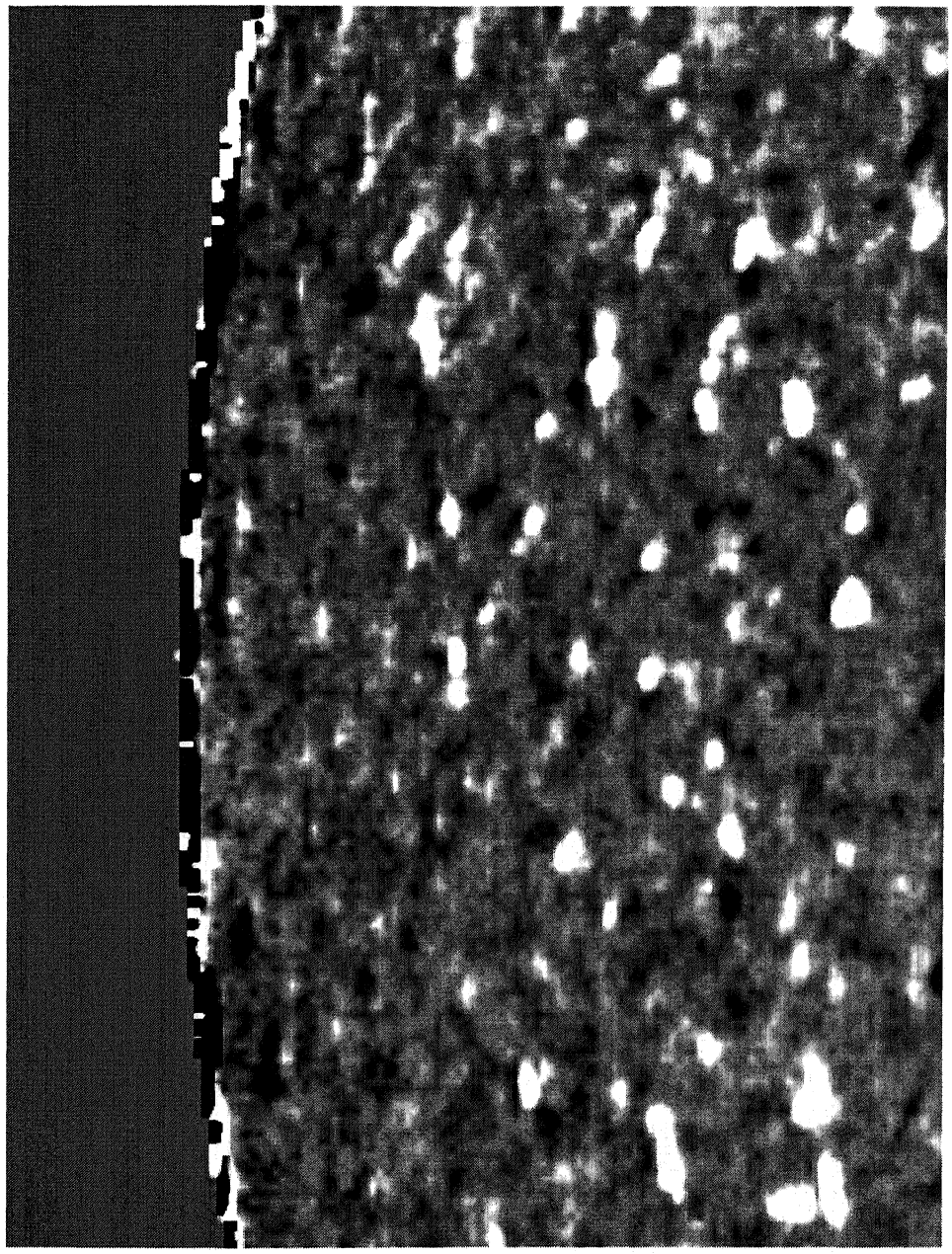

Fig.1a

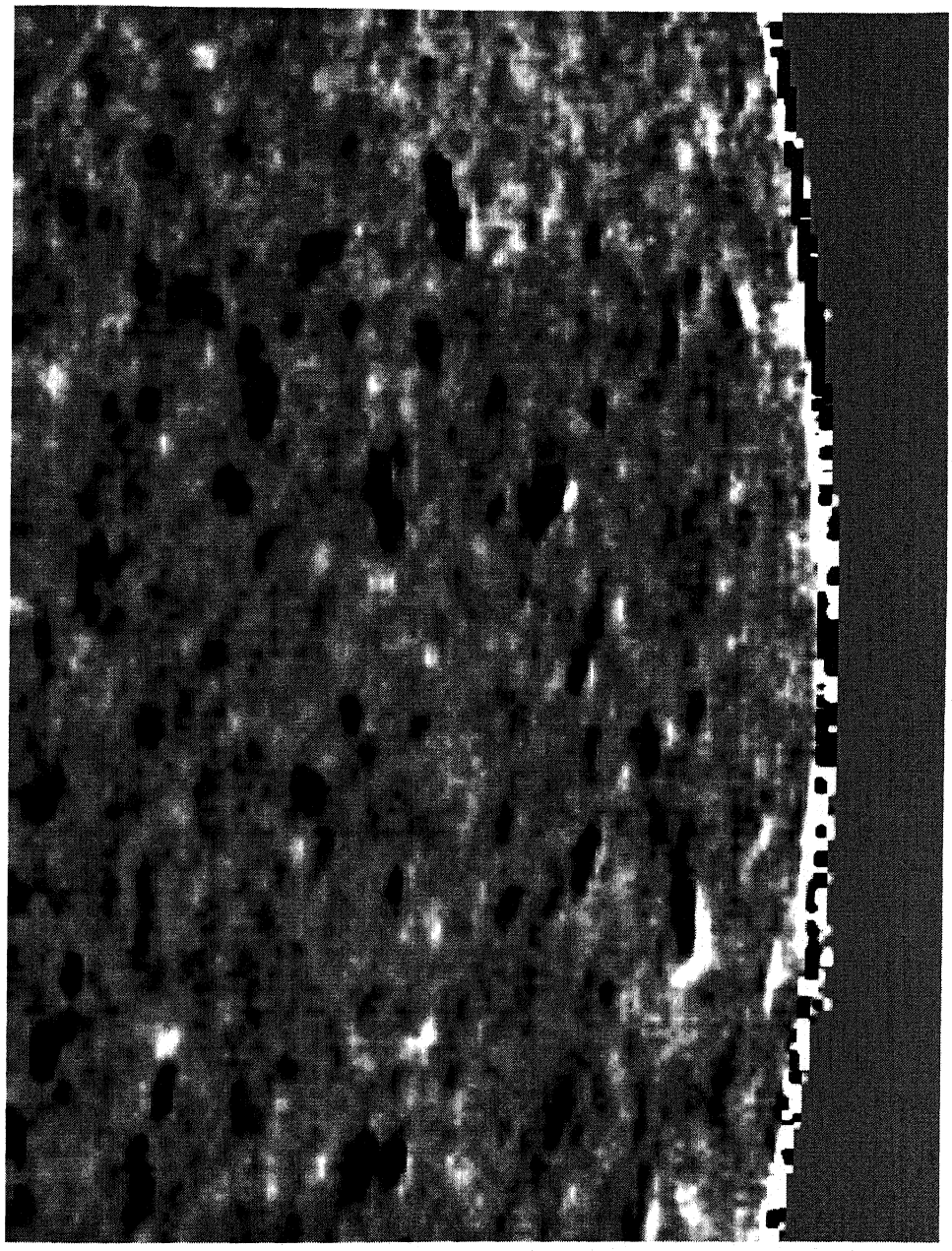

Fig.1b

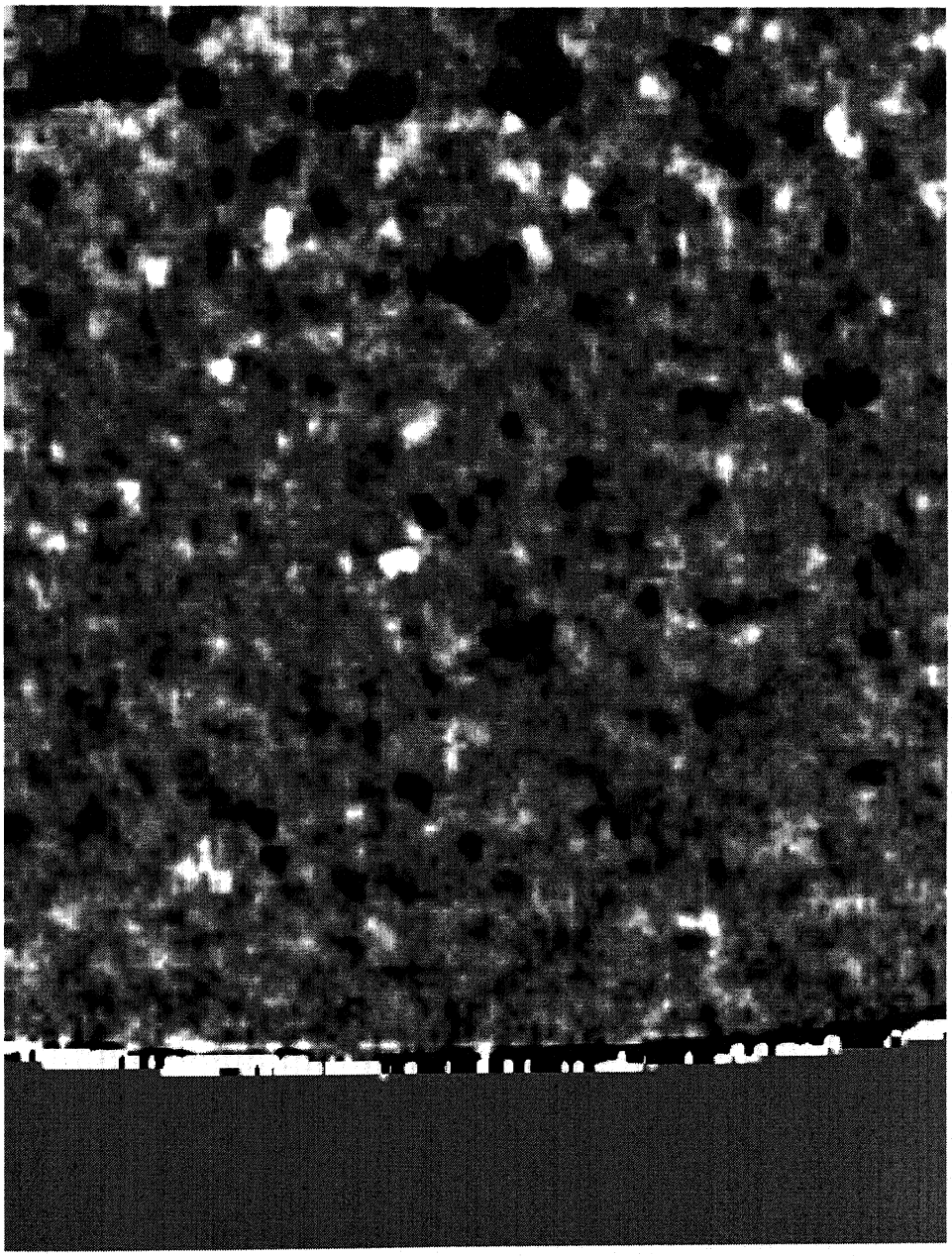

Fig.1c

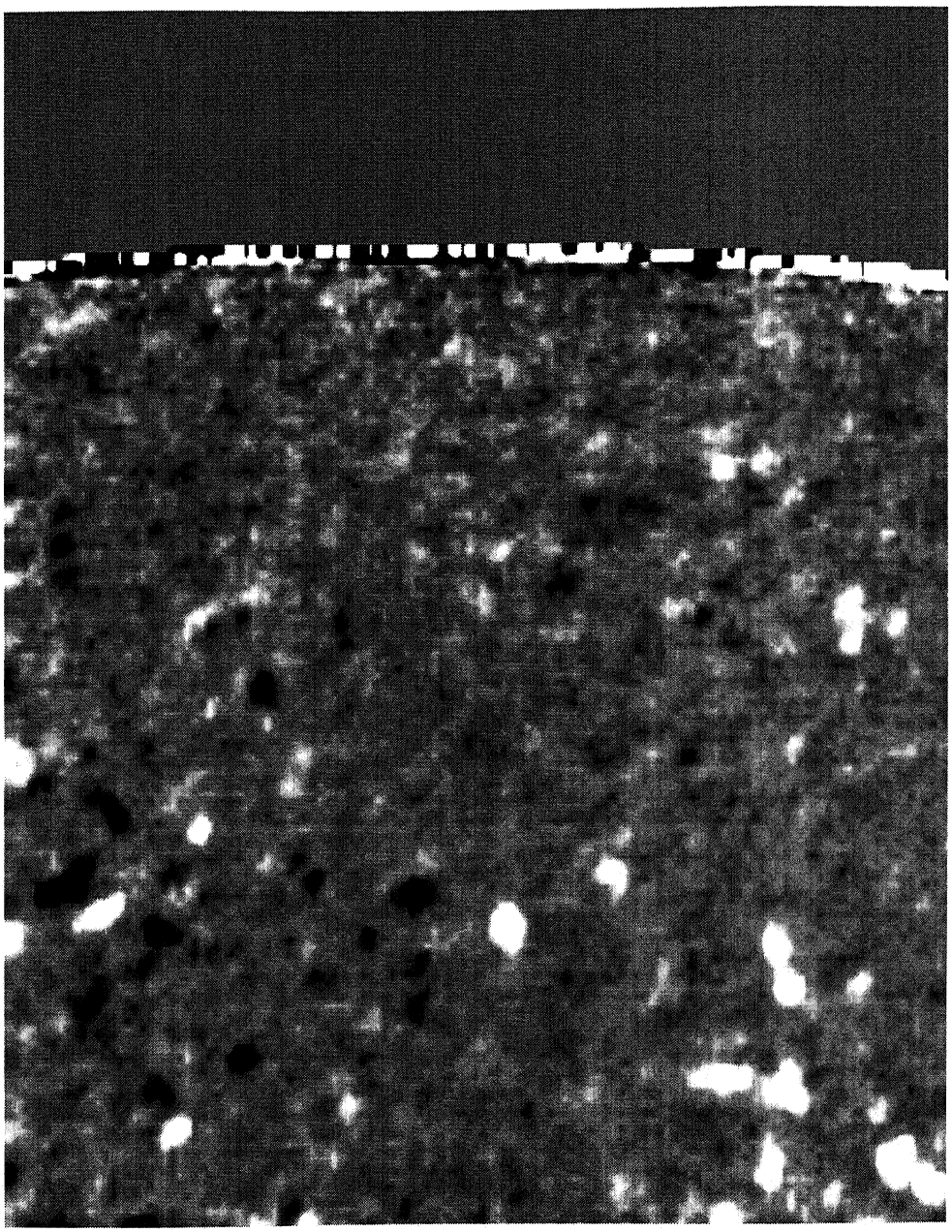

Fig.1d

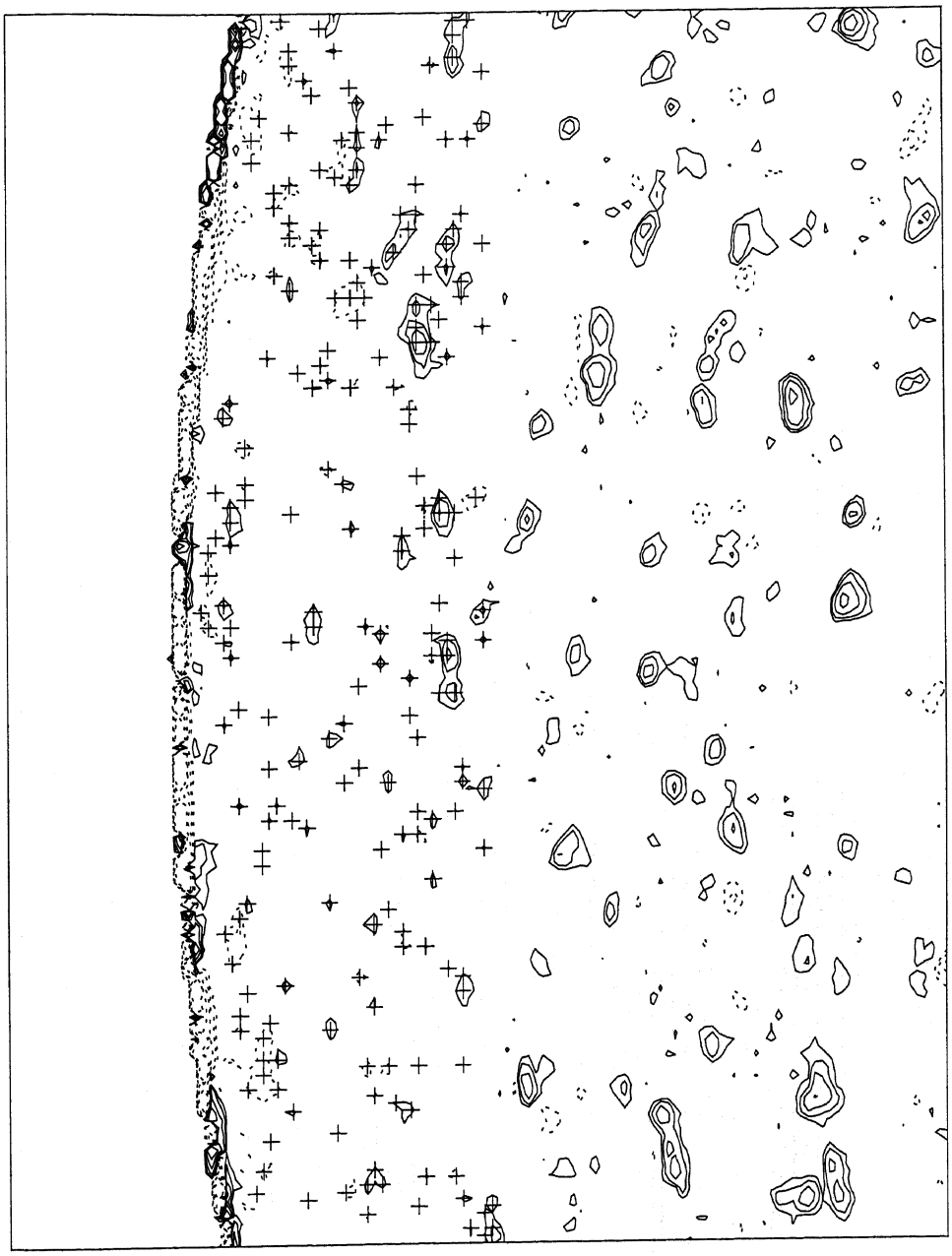

Fig.2a

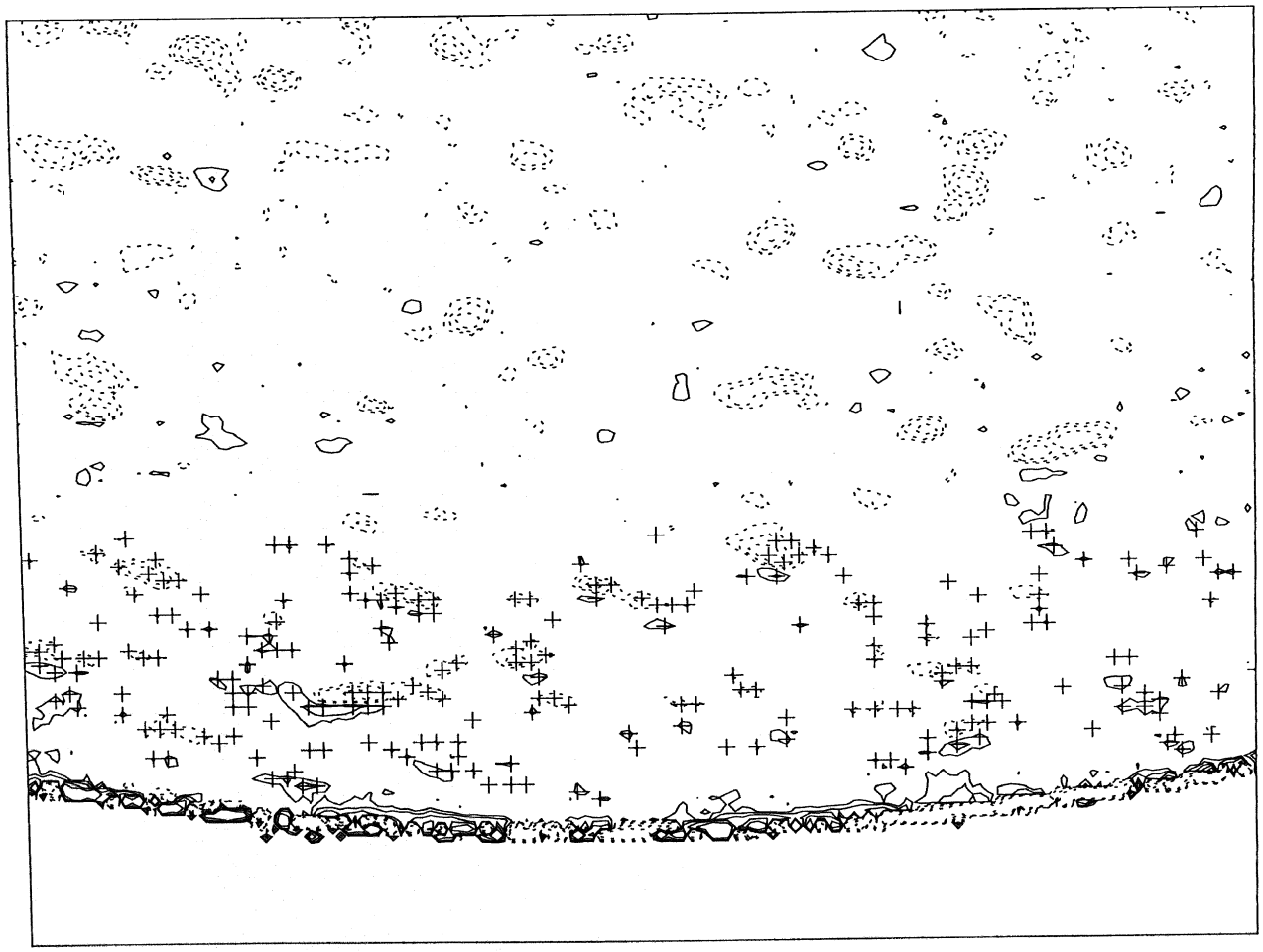

Fig.2b

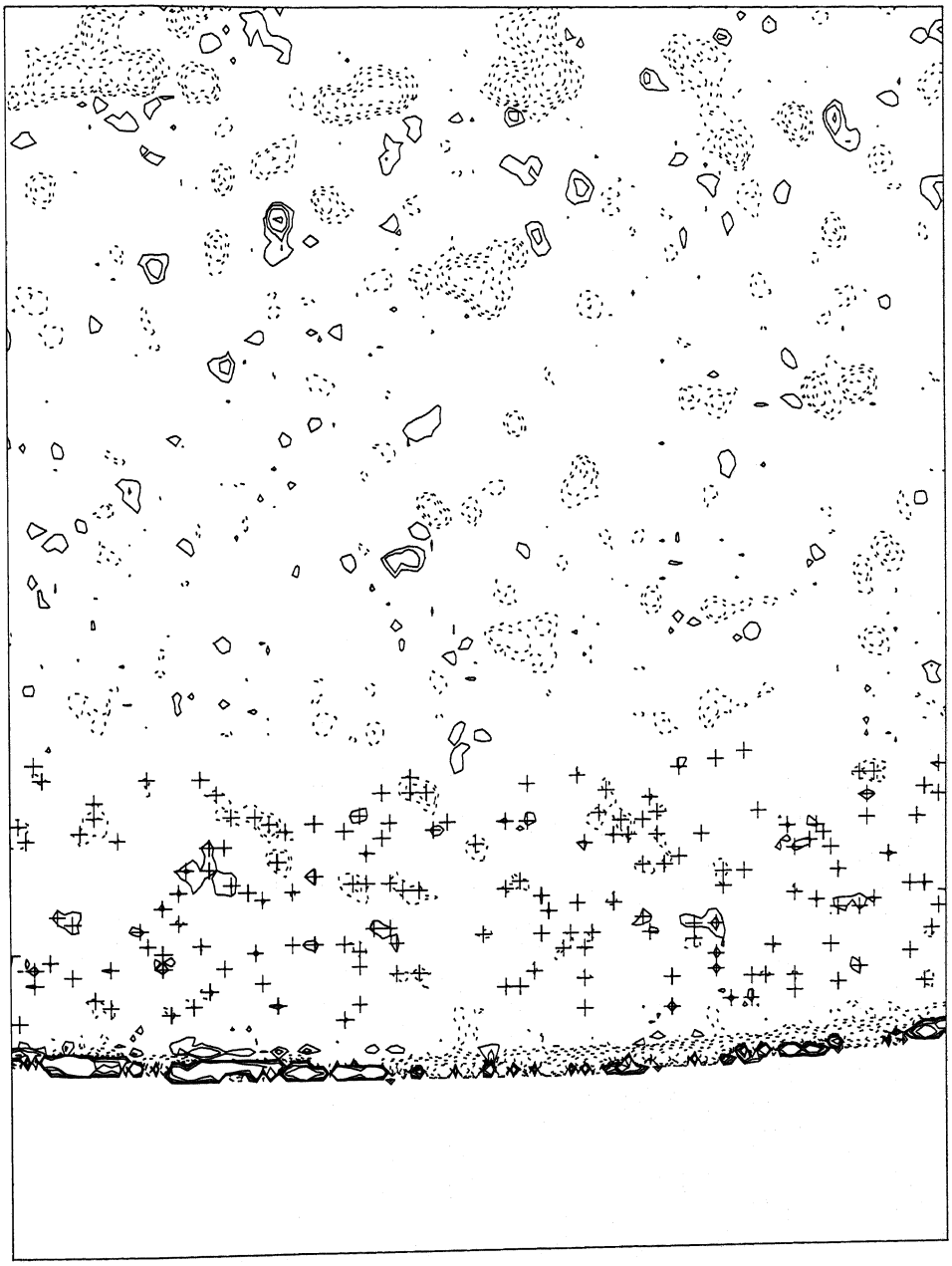

Fig.2c

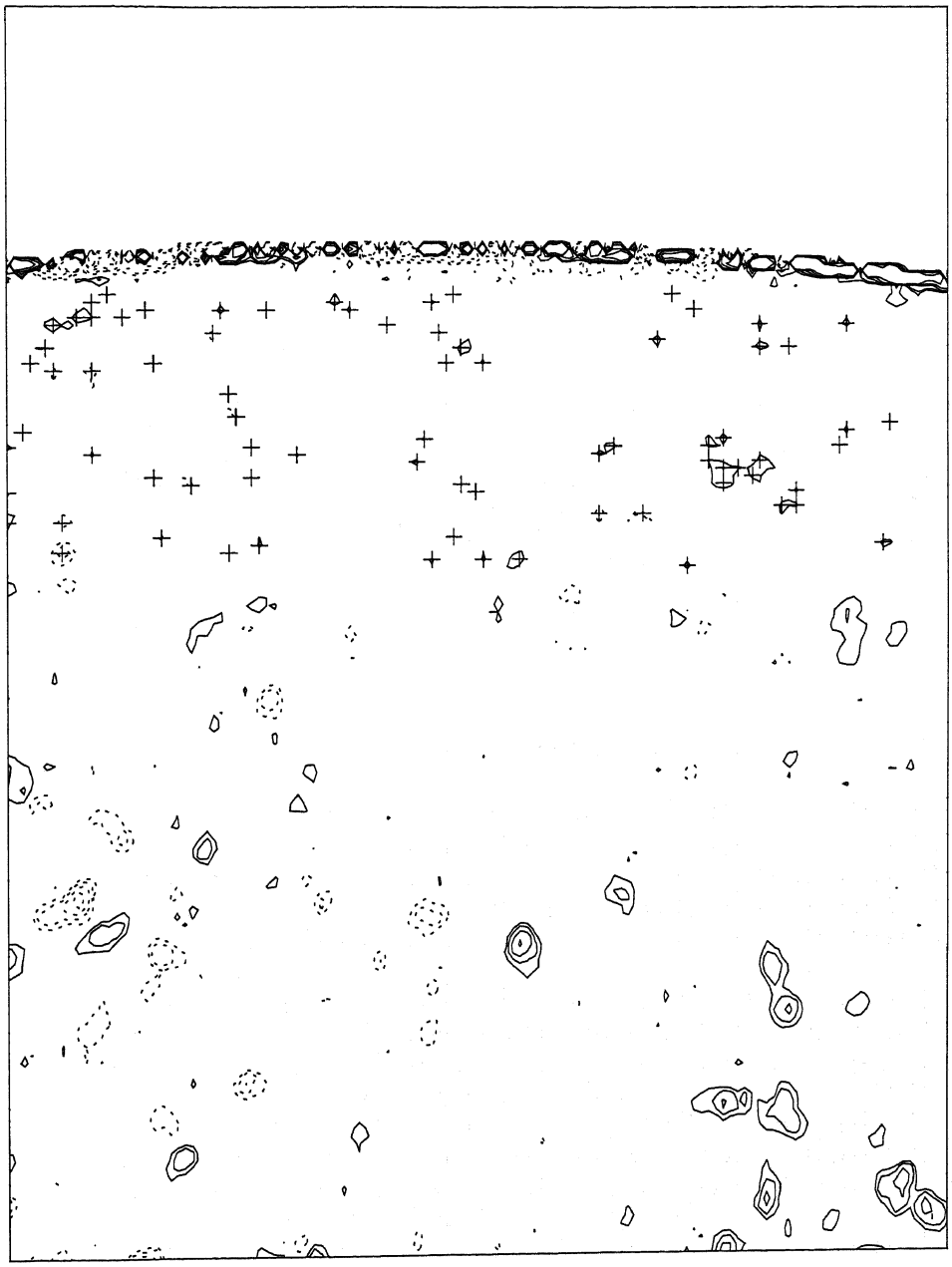

Fig.2d

A comparison between photospheric and chromospheric quiet-Sun magnetograms

Mei Zhang and Hongqi Zhang
Beijing Astronomical Observatory, Chinese Academy of Sciences, Beijing 100080, China
National Astronomical Observatories, Chinese Academy of Sciences, Beijing 100012, China

Received / Accepted

Abstract. Photospheric (FeIλ5324.19Å line) and chromospheric (H_β line) magnetic fields in quiet-Sun regions have been observed in the solar disk center by using the vector video magnetograph at Huairou Solar Observing Station of Beijing Astronomical Observatory.

Observational results show that the quiet-Sun magnetic elements on the solar photosphere and chromosphere present similar magnetic structures. Photospheric and chromospheric magnetograms show corresponding time variations. This suggests that the magnetic fields in quiet-Sun regions propose different 3-D magnetic configurations compared to those in solar active regions.

Keywords: Quiet Sun - Photospheric magnetic field - Chromospheric magnetic field

1. Introduction

It is generally believed that the magnetic field plays an important role in solar performances and activities. To better understand the behaviors of magnetic fields in the solar atmosphere, understanding 3-D structures of magnetic fields and how magnetic fluxes (and hence magnetic energies) are transported in the solar atmosphere becomes a critical problem.

Most of the observations of the solar magnetic fields are made in the solar photosphere. To understand the coronal magnetic fields, we have either to use observational photospheric magnetic fields to infer possible spatial magnetic field configurations (Demoulin et al., 1997; Cuperman et al., 1997; Wang, 1997; Yan and Wang, 1995; Van Driel-Gesztelyi et al., 1994) or to use ultraviolet and soft X-ray images to outline coronal magnetic fields (Worden et al., 1999; Neupert et al., 1998) or to combine both above methods (Wang, Wang and Qiu, 1999).

For active regions, the magnetic fields in the solar chromosphere usually show different structures compared to the photospheric ones. For example, the H_β chromospheric magnetograms show that they are different from photospheric ones in at least two respects. First, photospheric and chromospheric magnetograms sometimes show opposite polarity in some active regions (see Almeida (1997) and references therein), even though different authors have given different explanations. Liu et al. (1995) explained this phenomenon as a real flip and

Almeida (1997) explained it due to radiative transfer effects. Second, Zhang (1996) presented the evidences that the chromospheric magnetic fields in active regions are different from the photospheric one. By observing chromospheric magnetic fields at different wavelengths in the wing of the H_β line, he found that the magnetic fields extend up from the photosphere to the chromosphere continuously in the form of the fibril-like magnetic structures.

In this paper, we will inspect and compare quiet-Sun photospheric (FeIλ5324.19Å) and chromospheric (H_β) magnetograms and try to find whether there are also different magnetic structures existed between photospheric and chromospheric magnetograms in quiet-Sun regions. Observation and data reduction are presented in Section 2. Data analysis is presented in Section 3. Conclusion and discussion are presented in Section 4.

2. Observation and data reduction

The tunable birefringent filter of the solar telescope magnetograph at the Beijing Astronomical Observatory can be aimed at different passbands for different observations (Ai and Hu, 1986). For photospheric observations, the passband of the filter is set in the FeIλ5324 line: at 0.075Å from the line center for the measurement of longitudinal magnetic field. The equivalent width of FeIλ5324 line is 0.344Å, the FWHM of the filter passband is 0.15Å. For the chromospheric observations, the passband of the filter is set in the H_β line: at 0.24Å from the line center for the measurement of longitudinal magnetic field. The equivalent width of H_β line is 4.2Å, the FWHM of the filter passband is 0.12Å.

A series of photospheric and chromospheric magnetograms in quiet solar disk center were observed on 14 April 1998. The field of view is about $6' \times 4'$. The pixel resolution of the CCD is about $0.7'' \times 0.5''$. The spatial resolution of our data is actually $2'' \times 2''$ after a smoothing average of 3×4 pixels. The temporal resolution of one magnetogram we used for this study is 3 minutes.

2.1. OBSERVATION METHOD

Since chromospheric spectral lines (such as H_α, H_β, CaK and CaH lines) usually have wide equivalent widths, the noises of the chromospheric magnetograms gotten by these lines are usually high and have difficulty to detect the chromospheric magnetic field in quiet-Sun regions very well.

As an example, Figure 1 presents a photospheric magnetogram (Figure 1a) and a chromospheric magnetogram (Figure 1b) of the same field observed on 14 April 1998. Each observation has a 3-minutes integration time. From Figure 1, we can see that the noise level of the chromospheric magnetogram is much higher than the noise level

of the photospheric magnetogram and many magnetic features are not presented in the chromospheric magnetogram while they are presented in the photospheric one. By estimating the standard deviations (rms) of Stokes parameter V in blank fields, the noise level is estimated as 4 Gauss for the photospheric magnetogram and 20 Gauss for the chromospheric magnetogram.

In this study, we have used deep integration method to observe quiet-Sun chromospheric magnetic fields. We have observed each one photospheric magnetogram before and after ten chromospheric magnetograms observed. In order to get a low noise chromospheric magnetogram, we have integrated magnetograms for a time duration of several hours. To keep the photospheric and chromospheric magnetogram quasi-simultaneous, we have kept the observation time coverage of photospheric and chromospheric magnetograms almost the same.

The long time integration may indeed decreases the noise level, however, it may smear some intranetwork features due to their proper motions. If an intranetwork element moves at a speed of 0.4 km/s (Wang et al, 1995; Zhang et al., 1998), then in one hour, it moves 2", which is equivalent to the 2" spatial resolution. In 4 hours, it will move 8" (although it may not always move in the same direction). This will certainly smear some intranetwork features. In such a long time, only those low speed intranetwork elements (for example, those intranetwork elements with a speed of 0.05 km/s in Zhang et al. 1998) will not smear much. However, if a network element moves at a speed of 0.05 km/s (Wang et al, 1995), then in one hour, it moves 0.2". In 4 hours, it moves 0.8", which is below the 2" spatial resolution. So the network and some low speed intranetwork elements will not be smeared by this observation.

2.2. CALIBRATION

The radiative transfer of the $FeI\lambda 5324.19\mathring{A}$ line in the magnetic field and its theoretical calibration were made by Ai, Li and Zhang (1982). The radiative transfer of the H_β line in the magnetic field was discussed by Zhang and Ai (1986). The observational calibrations of these two lines were made by Wang, Ai and Deng (1996).

Here, we adopt the calibration of $FeI\lambda 5324.19\mathring{A}$ line in Ai, Li and Zhang (1982) and set the H_β line calibration fixed to achieve equal fluxes (on average) in $FeI\lambda 5324.19\mathring{A}$ and H_β magnetograms for a large number of identical networks near solar disk center. It is found that the results with this calibration of H_β line are almost the same as the results with the calibration of H_β line by Wang, Ai and Deng (1996).

2.3. PRIMARY RESULT

On 14 April 1998, we had a totally 7 hours' observation. We integrated observations from 02:07 UT to 06:00 UT and get Figure 2. Figure

2a is the integrated photospheric magnetogram and Figure 2b is the integrated chromospheric magnetogram.

We have integrated five 3-minutes photospheric magnetograms to get Figure 2a and fifty 3-minutes chromospheric magnetograms to get Figure 2b, all after position correlations of each magnetogram. The field of view is $4.6' \times 3.4'$ in Figure 2. By estimating the standard deviations (rms) of Stokes parameter V in blank fields, the noise level is estimated as 2 Gauss for the photospheric magnetogram (Figure 2a) and 5 Gauss for the chromospheric magnetogram (Figure 2b).

3. Data analysis

3.1. SIMILARITY BETWEEN PHOTOSPHERIC AND CHROMOSPHERIC QUIET-SUN MAGNETOGRAMS

From Figure 2, we can see that the magnetic structures in quiet-Sun photospheric and chromospheric magnetograms are quite similar.

To show this similarity further, we selected the strongest 37 identical network elements in both Figure 2a and Figure 2b and calculated the normalized magnetic flux density profiles of these elements. When calculating the flux density profiles, we have assumed the magnetic elements are nearly circularly symmetrical. Of course, this assumption will cause some error, but it should be correct in statistical meaning.

Normalized flux density profiles of these strongest 37 magnetic elements are shown in Figure 3. From Figure 3, we can see that the median width for elements to reduce to half of their center flux densities is about 2.5" for both photospheric and chromospheric magnetic elements. The variation of this half-center-density-width (HCDW) is somewhat larger for elements in the chromosphere than those in the photosphere. This can be understood since we have integrated 50 3-minutes magnetograms to get the final chromospheric magnetogram (as Figure 2b) and only 5 3-minutes magnetograms to get Figure 2a.

Figure 4 presents the ratios of HCDWs between the chromospheric magnetic elements and corresponding photospheric magnetic elements. We found that these ratios are between 0.91 to 1.19, with the median at 1.04. This shows that, with our observational resolution, the network elements observed in the chromosphere present similar magnetic structures and are not evidently larger than the network elements observed in the photosphere.

3.2. CORRESPONDING VARIATIONS BETWEEN PHOTOSPHERIC AND CHROMOSPHERIC QUIET-SUN MAGNETIC ELEMENTS

In order to study the variations of magnetic fields, we separated our raw data magnetograms into two groups and integrated the magnetograms in each group. Figure 5 presents the integrated photospheric (Figure 5a) and chromospheric (Figure 5b) magnetograms for the duration from

02:07 UT to 04:15 UT. Figure 6 presents the integrated photospheric (Figure 6a) and chromospheric (Figure 6b) magnetograms for the duration from 04:20 UT to 06:40 UT. Figures 5a and 6a have each integrated three 3-minutes photospheric magnetograms. Figures 5b and 6b have each integrated thirty 3-minutes chromospheric magnetograms. The field of view is $4.6' \times 3.4'$ in Figures 5 and 6.

By comparing Figure 5a with Figure 6a, we found that some variation features of the photospheric magnetic fields. A1, A2, A3, A4 and A5 are all features where flux annihilation happened. Elements with opposite polarities originally appeared in Figure 5a disappeared or became smaller in Figure 6a. B1 and B2 are examples where flux emerged. Flux elements appeared in Figure 6a in places where no elements are found in Figure 5a. C1 and C2 are examples of flux density variations. Flux elements became stronger in Figure 6a than they are in Figure 5a. C3 is an example of flux separation and C4 is an example of flux combination. These features are all known features of magnetic field variations happened in the photosphere. However, by comparing corresponding chromospheric magnetograms with photospheric ones, we found that all those variations happened in the photosphere have corresponding variations in the chromosphere.

4. Conclusion and discussion

Photospheric and chromospheric magnetic fields in quiet-Sun regions have been observed in the solar disk center. The photospheric magnetogram is obtained at a noise level of 2 Gauss. The chromospheric magnetogram is obtained at a noise level of 5 Gauss.

From our analysis, we find that:

1. Quiet-Sun photospheric and chromospheric magnetograms show similar magnetic structures. With a spatial resolution of 2", there is only a limited extension of the chromospheric magnetic elements sizes compared to the sizes of photospheric ones on average.

2. With a time resolution of 2 hours, variations of photospheric magnetic fields (such as flux emergence, flux annihilation, flux combination and separation, flux density variations) are found to have corresponding variations in the chromospheric fields.

While previous observations (Liu et al. 1995, Zhang 1996) have found many different features between photospheric and chromospheric magnetograms in active regions, our observations found that the quiet-Sun photospheric and chromospheric magnetograms show quite similar magnetic structures. This imply that the magnetic fields in quiet-Sun regions propose different 3-D magnetic configurations compared to those in solar active regions.

Since radiative transfer effects in the H_β line are complicated and one might expect a broad height range for the Stokes V response function, the H_β observations may be a combination of chromospheric and photospheric fields. This may partially account for the similarity

between the photospheric and chromospheric observations in quiet-Sun regions. However, even if the H_β observations may be a combination of chromospheric and photospheric fields, this effect should influence the quiet-Sun regions and active regions at the same time. The difference of magnetic features between active regions and quiet-Sun regions still suggest a different 3-D magnetic configuration existed in some degree between active regions and quiet-Sun regions. Also it is worth to point out here that, with a spatial resolution of 2", there is a possibility that the similarities in sizes (HCDWs) discussed in Figures 3 and 4 result from the features being unresolved in both data sets. This needs further higher resolution observations to check out.

Acknowledgements

The authors would like to thank all their colleagues in Huairou group for their helpful discussions. This research was supported by the Chinese Academy of Sciences and the National Science Foundation of China.

References

Ai, G., Li, W. and Zhang, H., 1982, Chinese Astronomy and Astrophysics, 6, 129.
Ai, G. and Hu, Y., 1986, Acta Astron. Sin, 27, 173.
Almeida, J.S., 1997, Astro.Astrophy., 324, 763.
Cuperman, S., Bruma, C. and Heristchi, D., 1997, Astro.Astrophy.Suppl.Ser., 122, 381.
Demoulin, P., Bagala, L.G., Mandrini, C.H., Henoux, J.C. and Rovira, M.G., 1997, Astro.Astrophy., 325, 305.
Liu, Y., Srivastava, N., Prasad, D., Li, W. and Ai, G.X., 1995, Solar Physics, 158, 249.
Neupert, W.M., Newmark, J., Delaboudiniere, J.P., et al., 1998, Solar Physics, 183, 305.
Van Driel-Gesztelyi, L., Hofmann, A., Demoulin, P., Schmieder, B. and Csepura, G., 1994, Solar Physics, 149, 309.
Wang, H., Tang, F., Zirin, H. and Wang, J., 1996, Solar Physics, 165, 223.
Wang, H.N., 1997, Solar Physics, 174, 265.
Wang, T.J., Ai, G.X. and Deng, Y.Y., 1996, Publ. Beijing Astronomical Observatory, 28, 31.
Wang, T.J., Wang, H.N. and Qiu, J., 1999, Astro.Astrophy., 342, 854.
Worden, J., Woods, T.N., Neupert, W.M. and Delaboudiniere, J.P., 1998, Astrophy.J., 511, 965.
Yan, Y. and Wang, J., 1995, Astro.Astrophy., 298, 277.
Zhang, H.Q. and Ai, G.X., 1986, Acta Astron. Sin., 27, 217.
Zhang, H.Q., 1996, Astro.Astrophy.Suppl.Ser., 119, 205.
Zhang, J., Wang J., Wang,H. and Zirin, H., 1998, Astro.Astrophy., 335, 341.

Fig.1. A photospheric magnetogram (a) and a chromospheric magnetogram (b) of the same field observed on 14 April 1998.

Fig.2. Quiet-Sun photospheric magnetogram (a) and chromospheric magnetogram (b) in the solar disk center. The observation duration is from 02:07 to 06:00 on 14 April 1998. The field of view is $4.6' \times 3.4'$. Bright (dark) structures correspond to positive (negative) polarities. Black (white) contours correspond to positive (negative) fields of 15, 30, 60, 120 Guass.

Fig.3. Normalized flux density profiles of strongest 37 identical magnetic elements in the field observed on 14 April 1998. The X-axis is the angle distances from centers of magnetic elements to their edges. The Y-axis is the normalized magnetic flux densities at different positions from centers of magnetic elements to their edges. Figure 3a is for the photospheric ones and Figure 3b is for the chromospheric ones.

Fig.4. Ratios between chromospheric HCDWs and corresponding photospheric HCDWs of 37 identical networks observed on 14 April 1998. X-axis is the distances from solar disk center. Y-axis is the ratios of HCDWs between chromospheric magnetic elements and corresponding photospheric magnetic elements.

Fig.5. Photospheric (a) and chromospheric (b) magnetograms of the field observed on 14 April 1998 for the duration from 02:07 UT to 04:15 UT. The field of view is $4.6' \times 3.4'$. Bright (dark) structures correspond to positive (negative) polarities. Black (white) contours correspond to positive (negative) fields of 15, 30, 60, 120 Guass.

Fig.6. Photospheric (a) and chromospheric (b) magnetograms of the field observed on 14 April 1998 for the duration from 04:20 UT to 06:40 UT. The field of view is $4.6' \times 3.4'$. Bright (dark) structures correspond to positive (negative) polarities. Black (white) contours correspond to positive (negative) fields of 15, 30, 60, 120 Guass.

a

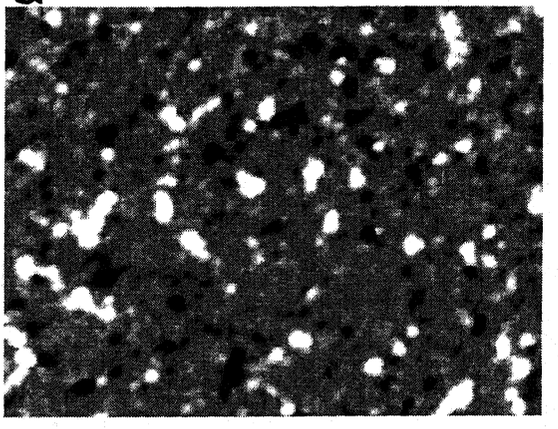

b

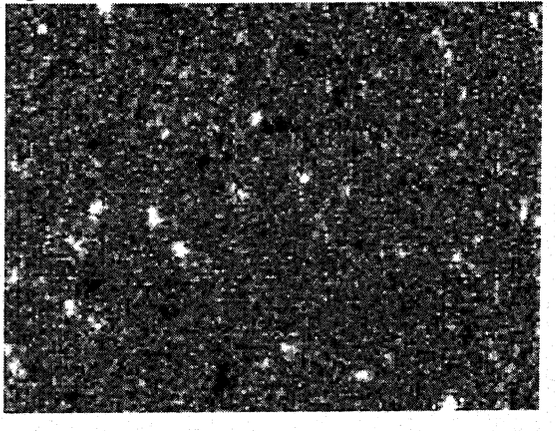

Fig.1

a

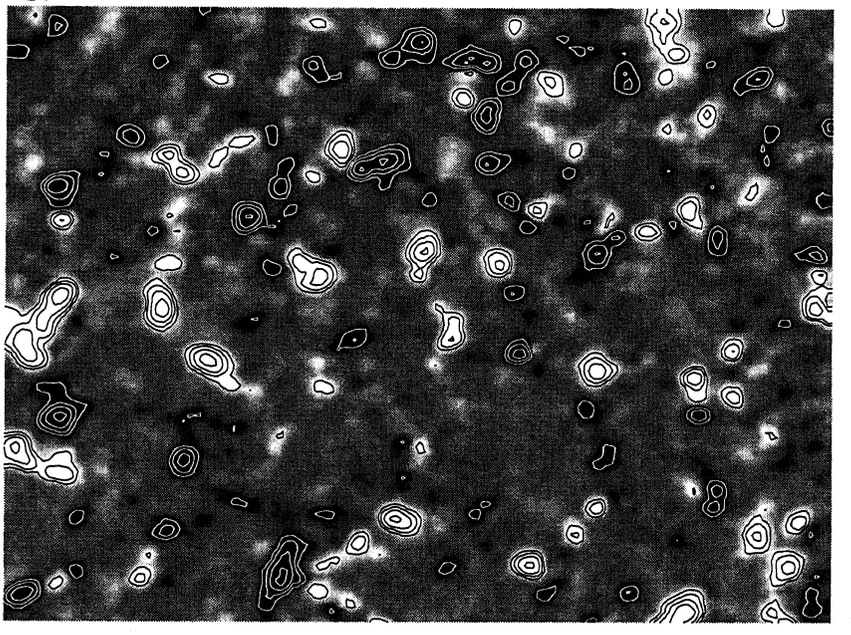

b

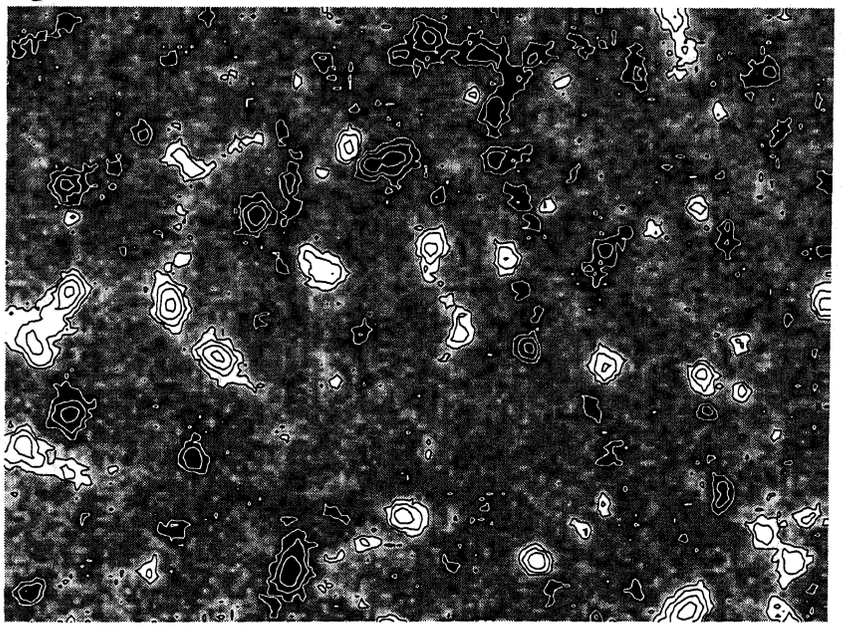

Fig.2

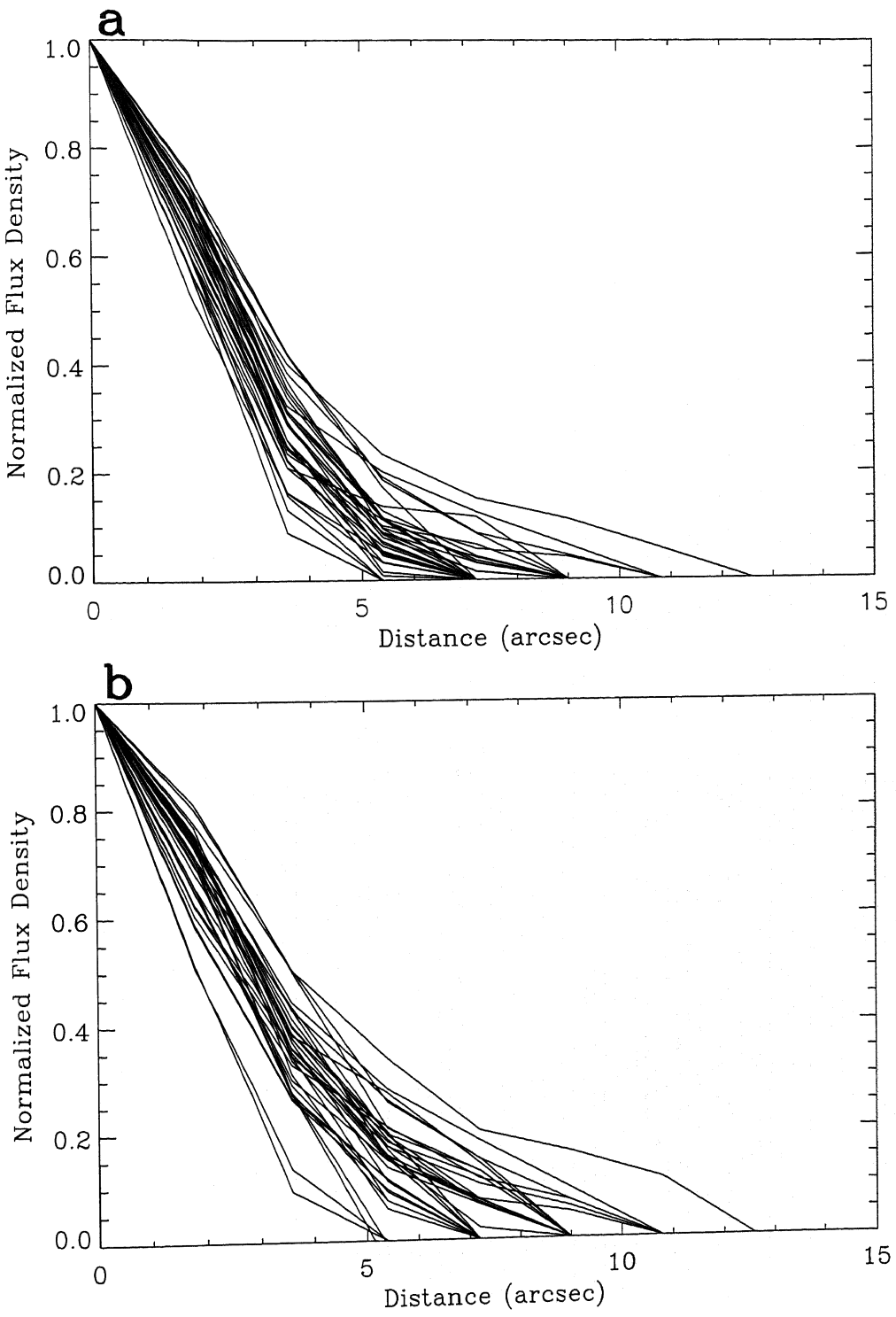
a
1.0
0.8
0.6
0.4
0.2
0.0
Normalized Flux Density
0
5
10
15
Distance (arcsec)
b
1.0
0.8
0.6
0.4
0.2
0.0
Normalized Flux Density
0
5
10
15
Distance (arcsec)

Fig.3

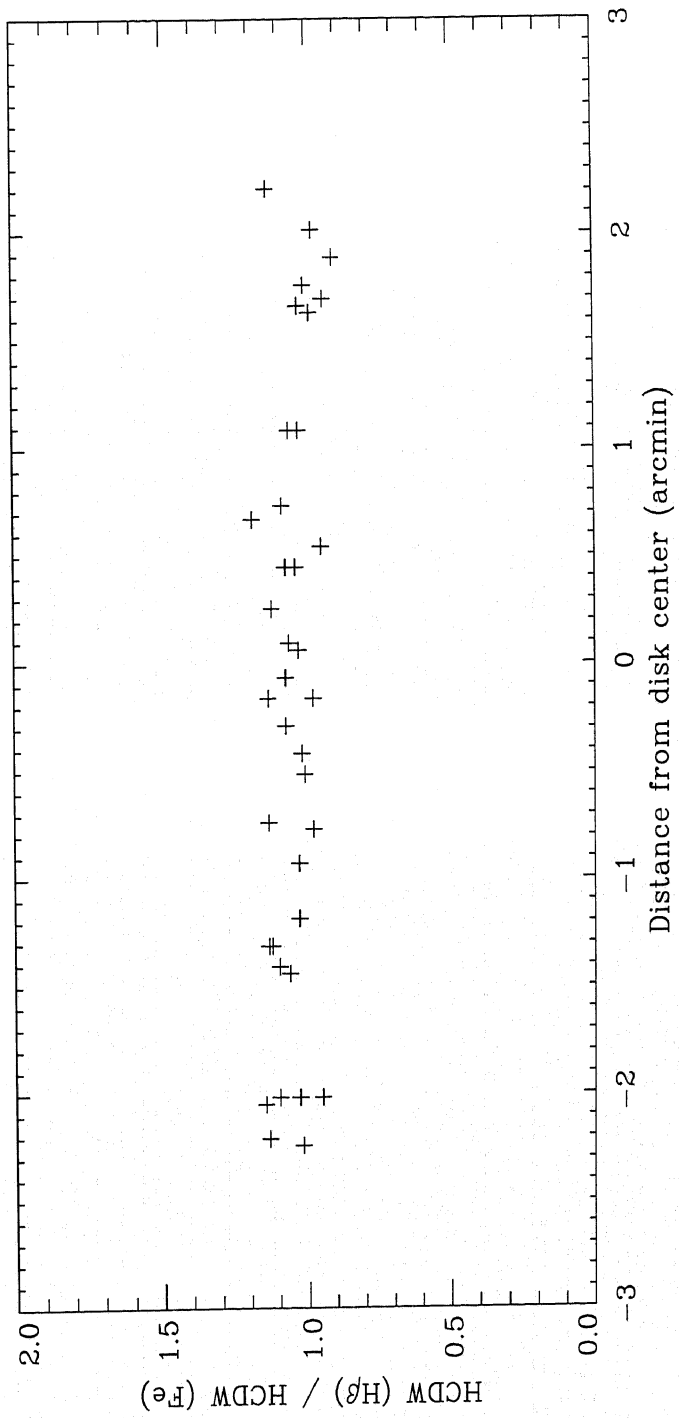
HCDW (Hβ) / HCDW (Fe)
2.0
1.5
1.0
0.5
0.0
−3
−2
−1
0
1
2
3
Distance from disk center (arcmin)

Fig.4

a

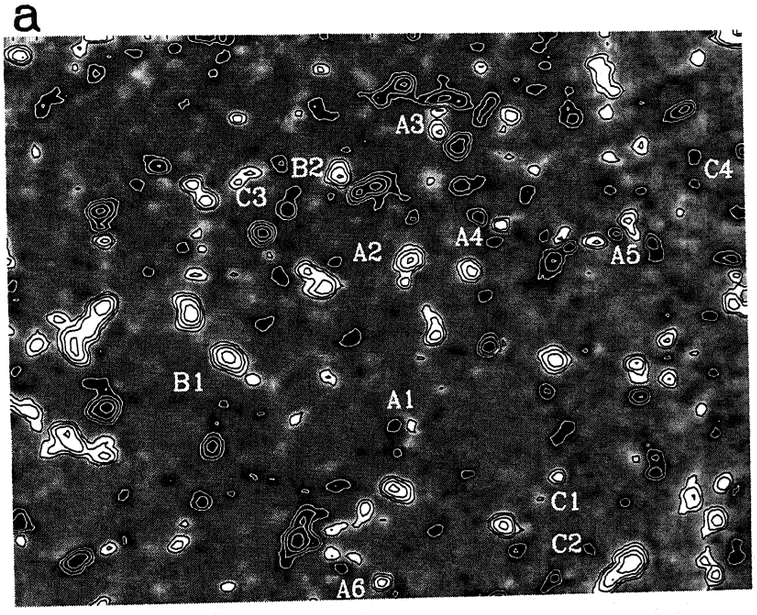

b

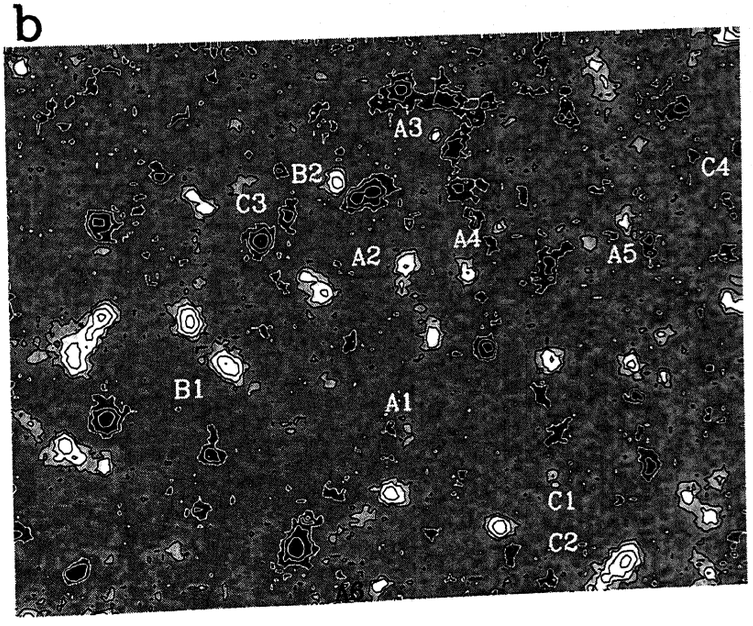

Fig.5

a

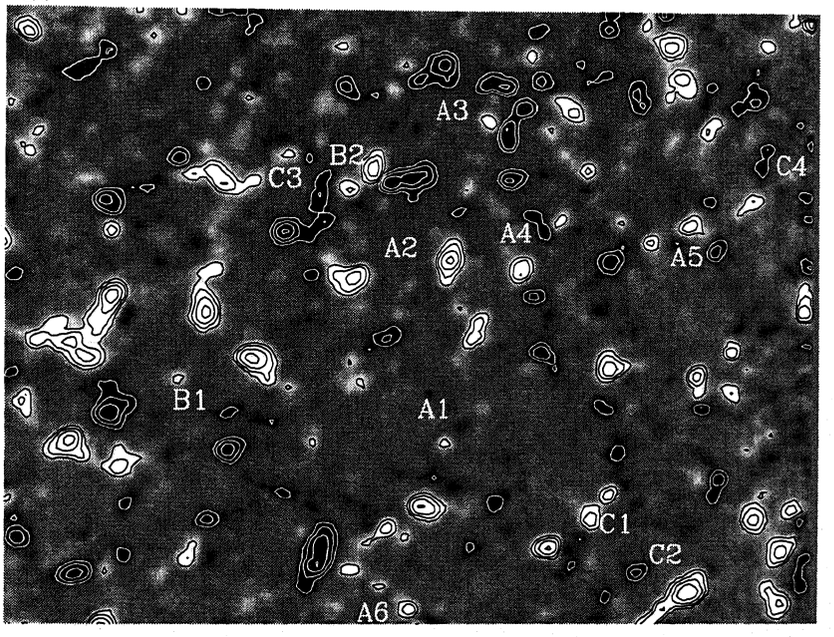

b

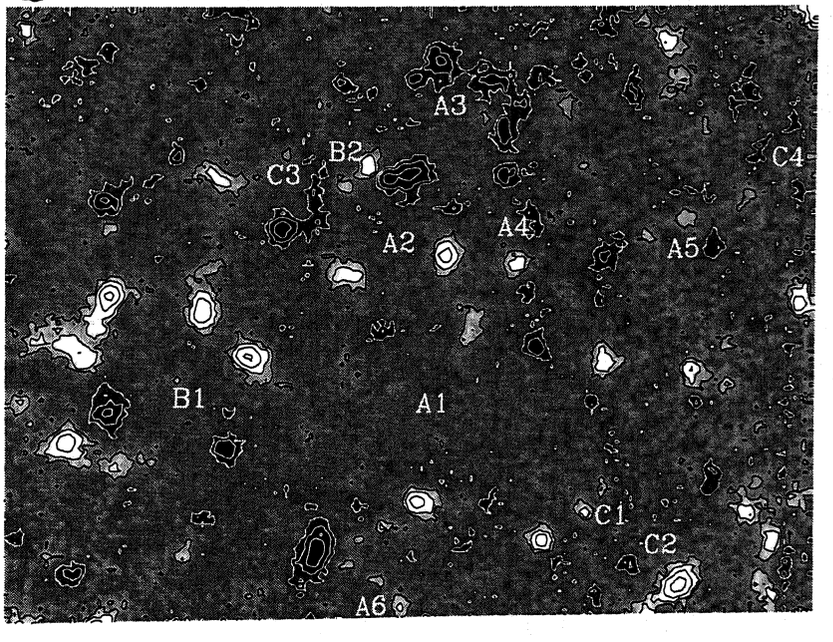

Fig.6

* 研究简讯 *

用多色测光方法发现红移 $z=3.3$ 类星体*

张 枚 陈建生 周 旭 严暾璟
朱 进 蒋兆基 郑中原 李耀华
(中国科学院北京天文台,北京 100080)

关键词 多色测光 巡天 类星体 高红移

宇宙的起源及演化一直是天文学热切关注的课题,而类星体以其具有的高红移及高内秉光度而成为探寻早期宇宙的探针,因此,寻找高红移类星体一直是天文学中一个热门且富于挑战性的课题.

本文报道了北京天文台观测宇宙学小组正在进行的利用多色测光巡天探寻高红移类星体的工作,并简介此项工作的早期进展——发现了一颗红移 $z=3.3$ 的类星体.

1 巡天观测

北京天文台观测宇宙学研究小组利用北京天文台兴隆站的 60/90 cm Schmidt 望远镜及 2048×2048 Areospace Ford CCD 及 15 色中带滤光片(覆盖 300~1 000 nm),开展了利用多色测光寻找高红移类星体的课题[1)]. 15 色中带测光组成的 SED (Spectral Energy Distribution)相当于一个低分辨率光谱[1],从一个典型天区(1 平方度)的上万个源中可以找出具有反常 SED 的天体,从而挑选红移直至 6 的类星体候选者.

从 1994 年 9 月到 1997 年 2 月,我们对中心位于 $6^h59^m48^s, 63°22'00''$附近的 1 平方度大小的 Abell 星系团 A0566 天区,进行了 7 个颜色的测光及定标观测. 测光波段及积分时间如表 1.

表 1 A0566 天区观测表

中心波长/nm	带宽/nm	积分时间/s
389.0	34.0	6 600
455.0	34.0	13 200
527.0	34.0	9 600
579.5	31.0	9 600
607.5	31.0	12 000
666.0	48.0	9 000
705.0	30.0	9 400

测光程序使用的是 IRAF 中的 DAOPHOT(Ⅱ)软件包. 经过测光及定标,在 A0566 天区得到了 10 096 个源的 SED.

1997-05-09 收稿,1997-07-18 收修改稿
* 国家自然科学基金资助项目
1)Chen J S. 准备中

2 选源方法

如何从一个天区的上万个源中选出类星体候选者是此项研究的关键. 北京天文台观测宇宙学小组发展了多种选源方法,本文介绍其中的一种:与模板比较法.

我们搜集了许多已知恒星、星系及类星体的光谱作为我们的光谱库. 其中恒星光谱有: Silva & Cornell[2], Jocoby, Hunter & Christian[3], Straizyz (理论)[4], Gunn & Stryler[5], Kurucz(理论)[6]. 星系光谱有:Kennicutt(观测)[7] Coleman, Wu & Weedman(观测)[8], Rocca-Volmerange & Guiderdom(理论)[9]. 类星体光谱有 Waymann & Morris[10]. 将这些光谱与我们的滤光片透过率卷积就可得到各类恒星及星系、类星体(包括不同红移处)的在我们测光系统中的 SED. 我们把这些各类恒星、星系及类星体应具有的 SED 形状称为模板.

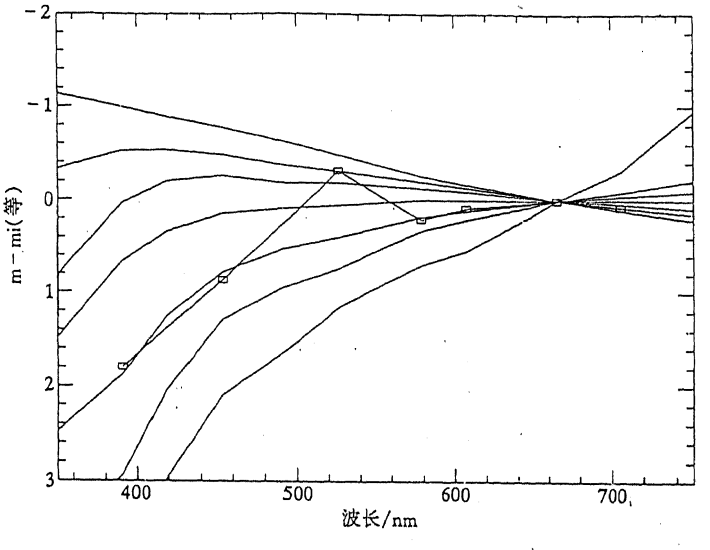

图 1 典型恒星的 SED(实线)以及选出的 $z=3.3$ 的类星体的 SED (加小方框的实线)

在选源时,首先把观测的 SED 与模板进行比较,剔除掉与恒星、星系具有相似 SED 的源,即得到特殊 SED 的源. 其次,再从这些具有特殊 SED 的源中,挑选与类星体 SED 相似的源作为类星体候选者. 第一步剔除过程完全采用计算机选源,从大约 1 万个源中选出 100 个左右. 第二步采用人工选择的方法,逐个选出. 图 1 给出了若干典型恒星的 SED 和选出的 $z=3.3$ 的类星体. 从图 1 可以看出,类星体的 SED 与恒星的 SED 有很大的差别.

3 有缝光谱观测

1997 年 3 月 4 日,我们把从 A0566 天区中选出的几个候选者在北京天文台兴隆站 2.16 m 望远镜上进行了光谱观测,即发现了一颗红移 $z=3.3$ 的高红移类星体. 它的坐标为:07:08:02.3,63:16:01 (历元 2 000.0).

观测使用的是 OMR 卡焦光谱仪,采用的色散为 20.0 nm/mm,分辨率为 0.48 nm/pixel,光谱覆盖从 345.0～845.0 nm,用 Kitpick 分光流量标准星进行了流量定标,爆光时间为 1 h. 图 2 即为观测到的 $z=3.3$ 的类星体,上半部为多色巡天得到的 SED,下半部为光谱.

4 讨论

从图 2 可以看出,低分辨率的 SED 与光谱符合相当好,且已基本勾画出光谱的特征. 这

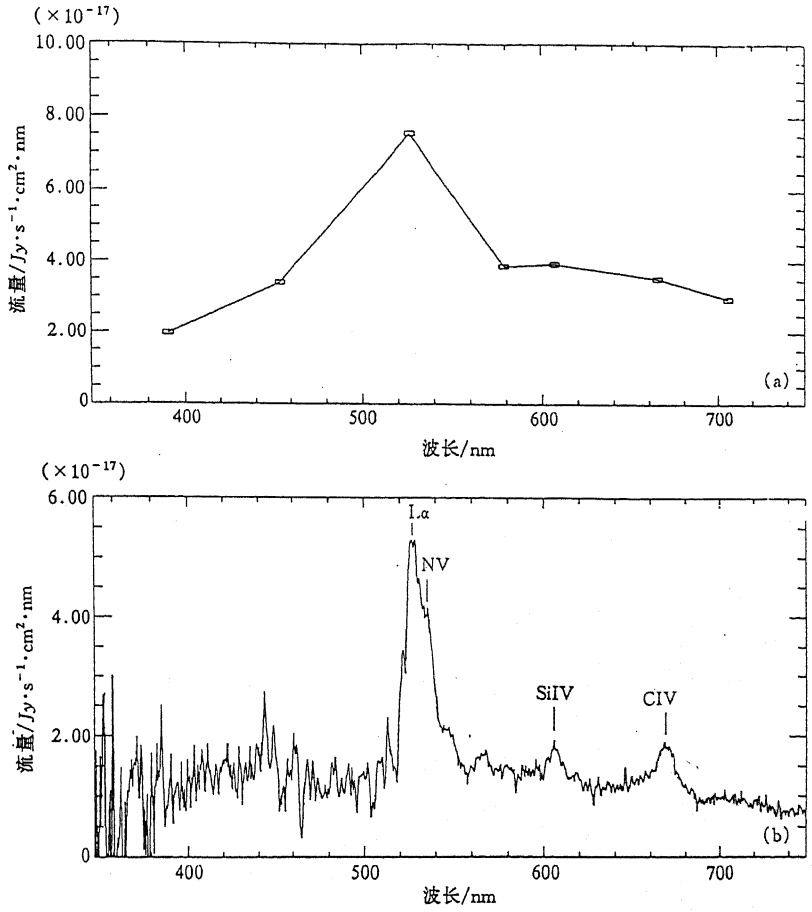

图 2　红移 $z=3.3$ 的类星体的 SED (a)及光谱(b)

表 2　发射线波长及谱线证认

发射线波长/nm	证认	静止波长/nm	红移
525.9	Lyα	121.6	3.325
535.6	N V	124.0	3.319
605.8	Si IV	140.0	3.327
669.6	C IV	154.9	3.323
			平均:3.324

表明利用多色 SED 作为低分辨率的光谱进行选源的方法是相当可靠与成功的. 同时,这颗类星体的视星等相当亮($m_{5270}=16.9$ 等),其绝对星等为 $M_{5270}=-29.5$ 等(取 $H_0=50$ km/s·Mpc),属于极高光度的类星体. 另外,这颗类星体在 L_α 发射线的蓝侧并没有象通常高红移类星体光谱那样,L_α 的蓝侧比红侧有一个下降台阶,如果这一点得到高分辨率、高信噪比及精确流量定标观测所证实的话,则是研究 L_α 森林及 Gunn-Peterson 效应的重要天体.

致谢　对北京天文台观测宇宙学组的王嘉力、李钱明及夜间观测的助手,以及吴宏处理光谱数据,均表感谢.

参 考 文 献

1 Fan X H, Burstein D, Cheng J S, et al. Deep wide-field spectrophotometry of the open cluster M67. Astronomical Journal, 1996, 112: 628

2 Silva D R, Cornell M E. A new library of stellar optical spectra. Astrophysical Journal Supplement Series, 1992, 81: 865

3 Jacoby G H, Hunter D A, Christian C A. A library of stellar spectra. Astrophysical Journal Supplement Series, 1984, 56: 278

4 Straizyz V. Multicolor stellar photometry. Ph D thesis of Lithuanian of Sciences, 1972

5 Gunn J E, Stryler L L. Stellar spectrophotometric atlas. Astrophysical Journal Supplement Series, 1983, 53: 121

6 Kurucz R L. Model atmosphere for population synthesis, in the stellar population of galaxies. In: Barbuy B, Renzini A, eds. Proceedings of the 14th Symposium of the International Astronomical Union. Angra Dos Reis, Brazil, 1991. Netherlands: Kluwer Academic Publisher, 1991. 225

7 Kennicutt R C. A spectrophotometric atlas of galaxies. Astrophysical Journal Supplement Series, 1992, 79: 255

8 Coleman G D, Wu C C, Weedman D W. Colors and magnitudes predicted for high redshift galaxies. Astrophysical Journal Supplement Series, 1980, 43: 393

9 Rocca-Volmerange R B, Guiderdoni B. An atlas of synthetic spectra of galaxies. Astronomy & Astrophysical Supplement Series, 1988, 75: 93

10 Weymann R J, Morris S L. Comparisons of the emission-line and continuum properties of broad absorption line and normal quasi-stellar objects. Astrophysical Journal, 1991, 373: 23

Newly discovered bright high redshift $z = 3.3$ quasar by multi-color photometry

ZHANG Mei (张 枚), CHEN Jiansheng (陈建生), ZHOU Xu (周 旭), YAN Haojing (严峭璟), ZHU Jin (朱 进), JIANG Zhaoji (蒋兆基), ZHENG Zhongyuan (郑中源) and LI Yaohua (李耀华)

(Beijing Astronomical Observatory, Chinese Academy of Sciences, Beijing 100080, China)

Received May 9, 1997

Keywords: multicolor photometry, sky survey, quasar, high redshift.

The origin and formation of the universe is a hot topic of modern astronomy. Since quasars have high redshifts and high luminosity, they can be used as the probe for studying the early universe. To search for high-redshift quasars has always been an exciting and challenging project in the world.

In this note, we introduce briefly a project to search for high-redshift quasars through our multicolor photometry sky survey, which is under way and its early progress: a newly discovered $z = 3.3$ quasar.

1 Sky-survey observation

60/90 cm Schmidt telescope was used in Beijing Astronomical Observatory with 2048×2048 Aerospace Ford CCD and 15-color intermediate-band filters (coverage: 300—1 000 nm) to do multi-color photometry sky survey for finding high-redshift quasars[1]. The spectral energy distribution (SED) formed by the 15-color photometry can function as a low-resolution spectrum. We can pick up sources with abnormal SEDs out of about 10 000 sources in one typical field (~1 square degree), and select the candidates for quasars with redshifts up to 6.

We have observed the Abell Cluster field A0566 which is centered at $6^h59^m48^s$, 63°22′00″, with a size of 1 square degree from September 1994 to February 1997. Photometry and calibration for 7 colors have been done. The color bands and integration times are listed in table 1.

Table 1 Observation log for A0566 field

Central wavelength/nm	Bandwidth of filters/nm	Integrated times/s
389.0	34.0	6 600
455.0	34.0	13 200
527.0	34.0	9 600
579.5	31.0	9 600
607.5	31.0	12 000
666.0	48.0	9 000
705.0	30.0	9 400

The data are reduced in standard way. The DAOPHOT(Ⅱ) software in IRAF package is used in the photometry. After calibration, the SEDs of 10 096 sources in A0566 field were obtained.

2 The select method of candidates

How to select the candidates for quasars with minimum selection effect is a key to this research project. Our group has developed several methods and made cross-check of the methods. Here we only introduce the method, in which the observed SEDs are compared with the model SEDs.

We have built up an SED data bank which includes spectra of different types of stars, galaxies and quasars. The SED bank consists of spectroscopic observations and theoretical model spectra. The spectra of stars are from Silva and Cornell[2], Jocoby, Hunter and Christian[3], Straizyz (model)[4], Gunn and Stryler[5], Kurucz (model)[6]. The spectra of galaxies are from Kennicutt[7], Coleman, Wu and Weedman[8], Rocca-Volmerange and Guiderdom (model)[9]. The spectra of quasars are from Waymann and Morris[10]. By convolution of these spectra with our filter transmission function, the SEDs of various stars, galaxies and quasars (with different redshifts) can be obtained in our system. We call these SEDs model SEDs.

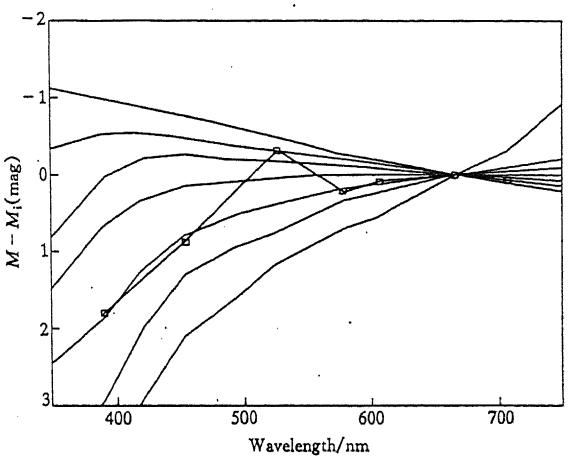

Fig. 1. SEDs of several typical stars (solid lines) and the SED of the selected $z=3.3$ quasar (solid line with squares).

By best fitting the SEDs of the sources in A0566 field with the model SED, we get a sample with SEDs similar to SEDs of quasars. The fitting process is performed by computer automatically. The program picks up about 100 sources out of about 10 000 sources, then the candidates are examined one by one manually. Fig. 1 shows the SEDs of several typical stars (solid lines) and the SED of the selected $z=3.3$ quasar (solid line with square). From fig. 1, we can see that the SED of quasar is very different from those of the stars.

3 Spectral observation

We observed the spectra of several sources selected from the A0566 field with the 2.16 m telescope at Beijing Astronomical Observatory on March 4, 1997. In this first round, a high redshift quasar with $z=3.3$ was found. Its coordinate (epoch of 2 000) is RA=07:08:02.3, Dec =63:16:01.

We used the OMR Carsigreen Spectrograph. The dispersion used was 20.0 nm/mm, giving the resolution of 0.48 nm/pixel. The exposure time was 1 h. Table 2 lists the identified emission line and the deduced redshift. The average redshift from 4 emission lines is 3.324. Fig. 2 shows

the SED (top) and the spectrum (bottom) of this quasar.

Table 2 Identification of emission line

Emission line wavelength/nm	Identified emission lines	Rest wavelength/nm	Redshift
525.9	Lα	121.6	3.325
535.6	NV	124.0	3.319
605.8	SiIV	140.0	3.327
669.6	CIV	154.9	3.323
			average 3.324

4 Discussion

Figure 2 shows that the SED from the multi-color photometry agrees very well with the spec-

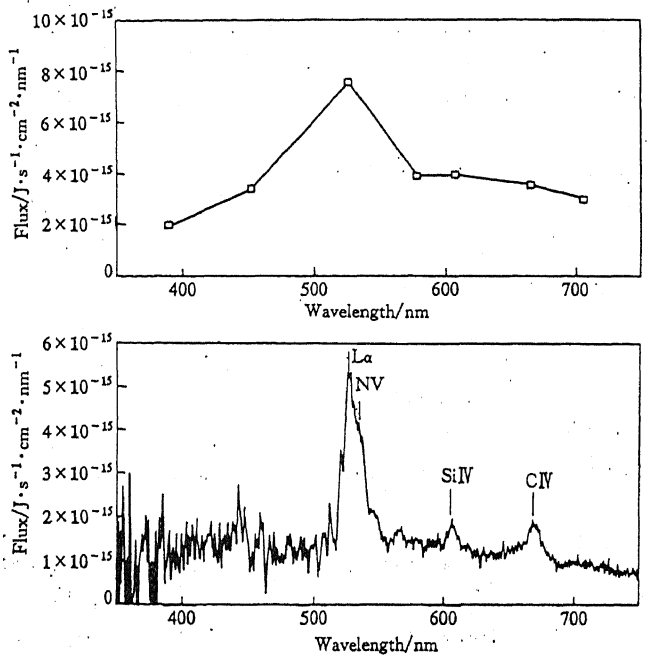

Fig. 2. SED (top) and the spectrum (bottom) of this quasar.

trum. This suggests that our method of picking up quasar candidates based on multi-color photometry SEDs is reliable and successful.

This quasar is very luminous. Its visual magnitude is $M_{5270}=16.9$ mag. The absolute magnitude is $M_{5270}=-29.5$ mag ($H_0=50$ Km/s·Mpc). It is still one of several most luminous quasars ever found. Another interesting feature of this quasar is that its blue side of Lα emission does not have a sharp drop compared to the red side, while such a drop is a common feature of the high redshift quasars. If this can be confirmed by further observation with higher resolution, higher S/N and more accurate flux calibration, this quasar will be an important object for investigating Lα forest and Gunn-Peterson effect.

Acknowledgement The authors would like to thank Wang Jiali, Li Qianming and the observation assistants for their help and Wu Hong for reducing the spectral data.

References

1 Fan, X. H., Burstein, D., Cheng, J. S. et al., Deep wide-field spectrophotometry of the open cluster M67, *Astronomical Journal*, 1996, 12: 628.
2 Silva, D. R., Cornell, M. E., A new library of stellar optical spectra, *Astrophysical Journal Supplement Series*, 1992, 81: 865.
3 Jacoby, G. H., Hunter D. A., Christian, C. A., A library of stellar spectra, *Astrophysical Journal Supplement Series*, 1984, 56: 278.
4 Straizyz, V., Multicolor stellar photometry, *Dissertation Thesis*, Lithuanian Academy of Sciences, 1972.
5 Gunn, J. E., Stryler, L. L., Stellar spectrophotometric atlas, *Astrophysical Journal Supplement Series*, 1983, 53: 121.
6 Kurucz, R. L., Model atmosphere for population synthesis, in *The Stellar Population of Galaxies*, *Proceedings of the* 14*th Symposium of the International Astronomical Union*, Angra Dos Reis, Brazil, August 5—9, 1991, Dordrecht: Kluwer Academic Publisher, 225.
7 Kennicutt, R. C., A spectrophotometric atlas of galaxies, *Astrophysical Journal Supplement Series*, 1992, 255.
8 Coleman, G. D., Wu C. C., Weedmen D W., Colors and magnitudes predicted for high redshift galaxies, *Astrophysical Journal Supplement Series*, 1980, 43: 393.
9 Rocca-Volmerange, R. B., Guiderdoni, B., An atlas of synthetic spectra of galaxies, *Astronomy & Astrophysical Supplement Series*, 1988, 75: 93.
10 Waymann, R. J., Morris, S. L., Comparisons of the emission-line and continuum properties of broad absorption line and normal quasi-stellar objects, *Astrophysical Journal*, 1991, 373: 23.

Astron. Astrophys. 300,359–365 (1995)

ASTRONOMY
AND
ASTROPHYSICS

Faint radio sources with peaked spectra

I. VLA observations of a new sample with intermediate flux-densities

I.A.G. Snellen[1], M. Zhang[2], R.T. Schilizzi[1,3], H.J.A. Röttgering[1,6,7], A.G. de Bruyn[4,5], and G.K. Miley[1]

[1] Leiden Observatory, P.O. Box 9513, 2300 RA Leiden, The Netherlands
[2] Beijing Astronomical Observatory, Beijing, Peoples Republic of China
[3] Joint Institute for VLBI in Europe, Postbus 2, 7990 AA Dwingeloo The Netherlands
[4] Netherlands Foundation for Research in Astronomy, Postbus 2, 7990 AA Dwingeloo, The Netherlands
[5] Kapteyn Institute, Postbus 800, 9700 AV Groningen, The Netherlands
[6] Mullard Radio Astronomy Observatory, Madingley Road, Cambridge, CB3 OHA, England
[7] Institute of Astronomy, Madingley Road, Cambridge, CB3 OHA, England

Received 12 September 1994 / Accepted 1 February 1995

Abstract. We present 2 and 20 cm observations with the VLA of 25 candidate peaked spectrum radio sources. These data combined with those from earlier surveys have allowed us to construct radio spectra spanning a range of frequency from 0.3 to 15 GHz. Ten of the 25 sources are found to be variable with no dominant peak in their spectra, four are large extended sources with simple steep spectra, and ten are confirmed as definite peaked spectrum sources, whose spectra are dominated by a peak between 1.0 and 2.5 GHz, with peak flux densities between 0.4 and 3.8 Jy. Two of the latter group are variable in flux density, but their spectra appear to remain peaked during the variation.

Key words: galaxies: active – radio continuum: galaxies – quasars: general

1. Introduction

Compact steep spectrum (CSS) sources have emerged as the third major category of extragalactic radio source in cm wavelength surveys, in addition to extended steep spectrum sources and compact flat spectrum sources. In a survey at 2.7 GHz, 31% of the radio sources was found to be compact ($\theta < 5''$) and to have a steep spectrum ($\alpha < -0.5$, $S \sim \nu^{\alpha}$) (Peacock & Wall 1982). A typical CSS source has a turnover in its spectrum at frequencies around 100 MHz. Compact steep spectrum sources appear to be a subset of a more general class of peaked spectrum sources characterized by a narrow peak in their spectra, and (steep) fall off in flux density above and below the peak. Sources which have peaks in flux density close to 1 GHz have been called Gigahertz Peaked Spectrum (GPS) sources.

Send offprint requests to: I.A.G. Snellen

Known peaked spectrum sources are intrinsically powerful ($L_{radio} \sim 10^{45}$ erg s^{-1}) yet restricted to small dimensions (< 1 kpc, e.g., Mutel & Phillips (1988). Peaked spectrum sources have low radio polarizations (Rudnick & Jones 1982; O'Dea et al. 1991), which may be caused by a tangled magnetic field or very large Faraday rotation measures. The scale of the radio emission corresponds to the characteristic scale of the narrow emission line region in the optical (~ 1 kpc) for sources whose spectra peak in the 100 MHz range, but for sources whose spectra peak close to 1 GHz, scale sizes of 1 to 10 pc (somewhat larger than the broad line region) are observed. This behaviour is consistent with the spectral turnover being due to synchrotron self absorption, and as expected from synchrotron theory, the shorter the wavelength at which the radio emission peaks, the smaller the emitting source (Slysh 1963; Williams 1963).

The steep fall-off in the spectra at high frequencies probably implies that there is no fresh injection of relativistic plasma in the cores of these objects, or that the electrons are injected with very steep dependence on energy (O'Dea et al. 1991). The first is consistent with the fact that these sources are weakly if at all variable (e.g. OQ 208, de Bruyn 1990). The steepness in the optically thick part of the spectrum strongly suggests that the sources are sharply confined with morphologies not likely to consist of a long jet or series of components peaking at different frequencies (de Bruyn 1991).

The few VLBI observations of peaked spectrum sources in the literature (e.g., Phillips & Mutel 1980; Dallacasa et al. 1994) show that their morphologies are dominated by two components with very similar spectra. It can be expected that changes in the physical conditions in these components caused by component expansion or variability in the supply of relativistic electrons from the central source will generate changes in the spectral shape of the source which are coherent across the spectrum. Variability in flat spectrum sources composed of components

peaking at different frequencies is likely not to occur in a coherent manner across the whole spectrum.

The nature of peaked spectrum sources and their relationship in an evolutionary sense, to compact flat spectrum sources and extended steep spectrum sources, is unclear. We do not know if they are small in linear size, because they are (i) young radio sources (Mutel & Phillips 1988), (ii) old sources smothered by a very dense intergalactic medium, (iii) old classical doubles in a second stage of their life (Baum et al. 1990), or (iv) frustrated radio sources (Schilizzi 1990; O'Dea et al. 1991).

To be able to address these issues it is important to investigate the properties of peaked spectrum sources as a function of luminosity, redshift and rest-frame peak frequency. Until now such studies (Fanti et al. 1990; O'Dea et al. 1991) have only concentrated on the bright members of the class, due to the lack of a significant sample of peaked spectrum sources at lower flux densities. In this paper we present the results of VLA observations at 2 and 20 cm of 25 candidate peaked spectrum sources. These data combined with earlier survey data allow us to construct radio spectra for the sample, and select the truly peaked spectrum objects. This is the first part of a general program to investigate a low flux density sample of peaked spectrum radio sources. The median peak flux density of a source in our sample is ~ 0.7 Jy, a factor 4 lower than the median flux density of the Fanti et al. and Stanghellini et al. samples (Fanti et al. 1990; O'Dea et al. 1991).

2. Sample selection

Sources from the Texas 365 MHz and NRAO/Condon 1.4 and 5 GHz surveys were compared to select objects with optically thick spectral behaviour at frequencies below 1 GHz. Because initially only the images were available for the NRAO data, it was necessary to measure the flux densities for the Texas sources at 1.4 and 5 GHz ourselves (Röttgering et al. 1994). We restricted our attention to the most reliable sources from the Texas catalogue, i.e. those that had no indication of position or structure lobe shifts and whose structure were well modeled (code='+++', see Douglas et al. 1980). At the location of these Texas sources a gaussian brightness distribution was fitted to the 4850 MHz and 1400 MHz maps using the standard program 'JMFIT' from the NRAO image processing system AIPS. In cases of source confusion, the fitting algorithm can be unstable and give incorrect answers. Rejecting sources that have 4850 MHz and 1400 MHz positions that differ from the Texas positions by more than the specified uncertainties alleviates this problem. However, with this selection criterion, the number of sources will be incomplete and biased against sources whose structures and centroid positions change with frequency. The resulting sample consists of 13000 sources (Röttgering 1994). Fifty three sources were selected which had positive spectral indices ($\alpha \geq 0.2$) in the range 365-1400 MHz. Ten of these were at that time included in the O'Dea and Stanghellini et al. sample and have been excluded from our sample.

3. Observations and reduction

Twenty five sources from our sample (all sources with $3^h < R.A. < 15^h$) were observed with the VLA* in B array at wavelengths of 20 and 2 cm on 13 October 1991. A bandwidth of 50 MHz was used at both wavelengths. The resolutions are $3''.5$ at 20 cm and $0''.25$ at 2 cm. Observations of 3C286 were used for amplitude calibration. The phases were calibrated using standard nearby VLA phase calibrators, observed about every half hour. The sources were observed in "snapshot"mode for about 2.5 minutes at 20 cm and about 3.5 minutes at 2 cm. All the reduction was performed using AIPS. The maps for the 20 and 2 cm data were produced and cleaned using the ungridded subtraction method (Schwab 1984) implemented in the AIPS task MX. Self calibration was applied with two iterations on the phases alone and one on both phases and amplitudes. The rms noise in the maps is typically 0.5 mJy at both 2 and 20 cm. The flux densities and positions are determined using a gaussian fitting procedure as incorporated in the AIPS task IMFIT.

4. Results

Table 1 shows the position and flux density information for the 25 sources observed. The cores are sufficiently bright that the uncertainty in the flux density is dominated by systematic errors (2% at 20 and 3% at 2 cm, e.g. Carilli et al. 1991), except for the faintest sources at 2 cm. In column 1 the IAU name is given, in columns 2 to 7 the position determined from the 2 cm observations. The position uncertainty $\sim 0.1''$ is estimated from comparing our positions with the positions in the Patnaik sample (Patnaik 1992) for the ten sources which appear in both samples. Columns 8 to 12 give the Texas flux density, the Greenbank 20 and 6 cm flux densities and the 20 and 2 cm VLA flux densities. Since the different surveys have been carried out with widely varying beamwidths, we first checked for confusion. Since the beam for the 20 cm Greenbank survey is 12 arcminutes, we looked at the 6 cm Greenbank maps, and the 20 cm VLA maps for confusing sources. We found no cases in which confusion can be the reason for discrepancies between 20 cm Greenbank and VLA flux densities. The last column of Table 1 gives the source type. With our selection criteria, we find three types of radio sources: truly peaked spectrum sources (10), flat spectrum variables (10) and large extended sources (4). These sources are indicated by peaker, var and ext. For 0805+269, no 2 cm observations were obtained, so although we could not confirm that it is a peaked spectrum source, it remains a candidate.

Extended steep spectrum sources appear in the sample because the interferometer used for the Texas survey underestimates flux densities of sources larger than $> 15''$ and does not detect emission on angular scales greater than $2'$ (due to poor sampling of the uv plane), while the 20 cm Greenbank beam is $12'$, so an extended source with emission on scales of the order

* The Very Large Array is operated by the U.S. National Radio Astronomy Observatory which is operated by the Associated Universities, Inc., under cooperative agreement with the National Science Foundation.

Table 1. The sample of candidate peaked spectrum sources observed.

IAU name	Position(J2000) RA h	m	s	Dec °	′	″	S^{80}_{texas} (mJy)	S^{20}_{gb} (mJy)	S^{20}_{vla} (mJy)	S^{6}_{gb} (mJy)	S^{2}_{vla} (mJy)	type
0312+149	03	14	47.786	15	08	43.78	235	400	128	145	2	ext
0428+205	04	31	03.760	20	37	34.26	2760	3883	3710	2767	1110	peaker
0506+056	05	09	25.969	05	41	35.31	509	805	459	1010	429	var
0642+449	06	46	32.028	44	51	16.55	392	574	460	1188	2756	var
0700+470	07	04	09.563	47	00	55.86	518	817	824	437	226	peaker
0705+486	07	09	08.008	48	36	55.53	498	672	260	240	69	ext
0706+460	07	10	10.507	45	57	24.80	227	418	412	102	17	peaker
0727+409	07	30	51.345	40	49	50.82	215	401	387	461	303	var
0754+100	07	57	06.642	09	56	34.86	731	1058	805	761	1756	var
0805+269	08	08	36.742	26	46	36.53	287	507	438	257	-	cand
0829+046	08	31	48.880	04	29	39.13	641	959	1200	2113	1113	var
0851+202	08	54	48.875	20	06	30.59	1216	2259	1937	2621	5750	var
0930+493	09	34	15.760	49	08	21.81	460	725	774	573	285	peaker
1048+556	10	51	47.396	55	23	08.50	270	426	132	135	10	ext
1059+282	11	02	14.289	27	57	08.70	303	430	270	400	281	var
1128+385	11	30	53.282	38	15	18.54	652	879	717	729	787	var
1131+493	11	33	59.223	49	03	43.42	779	1066	150	346	30	ext
1133+432	11	35	55.983	42	58	44.65	640	1443	1385	449	118	peaker
1144+542	11	46	44.201	53	56	43.07	289	410	406	477	300	peaker
1144+352	11	47	22.126	35	01	07.45	370	679	600	670	359	peaker
1145+268	11	47	59.762	26	35	42.26	260	419	300	377	407	var
1225+368	12	27	58.724	36	35	11.69	1249	2151	2070	812	154	peaker
1324+574	13	26	50.570	57	12	06.70	198	472	506	236	224	peaker
1355+441	13	57	40.592	43	53	59.80	294	781	709	452	225	peaker
1418+546	14	19	46.592	54	23	14.75	720	1547	1140	1704	1450	var

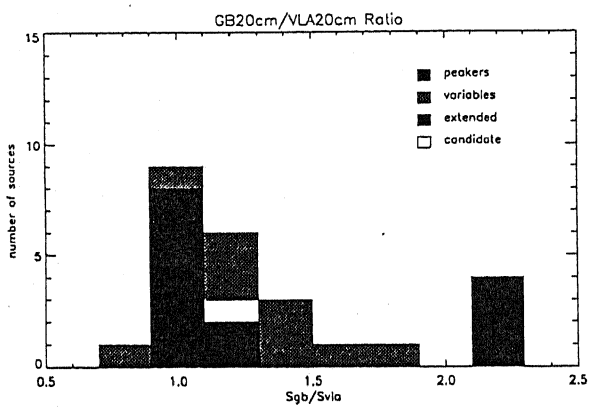

Fig. 1. The ratio between the Greenbank and VLA 20 cm flux densities

of 10′ will also appear with a peaked spectrum when the two surveys are combined. In this case the 20 cm VLA flux density is much smaller (like 50%) than the 20 cm Greenbank flux density and the VLA map shows extended structure.

We are sensitive to flat spectrum variable sources, because the three finding surveys were produced at different epochs. For example, a flat spectrum source whose flux density increased in the middle range of wavelengths will appear to have a peaked spectrum. In this case the 2 and 20 cm VLA flux densities can not be related to the Greenbank and/or Texas flux densities. We conclude that a source appears in our sample because of variability, if (1) the difference between the Greenbank and VLA 20 cm flux densities is larger than 20% (see Fig. 1) or (2) additional fluxpoints introduce a large scatter and the eventually cone shape of the spectrum disappears. For 19 of the sources we have found additional fluxpoints in literature. Two additional sources were found in this way to appear in our sample because of variability (0727+409 and 0851+202).

The sources 1144+542 and 1144+352 do show variability but are not excluded from the sample of true peaked spectrum sources because their spectral morphology appears to remain peaked during the variability. This is discussed in more detail in Sect. 5.

Of the ten peaked spectrum sources in our sample, two appear also in the O'Dea et al. and Fanti et al. samples (see Table 2). A curve of the form

$$\log S = a + b \times \log \nu + c \times \log^2 \nu \qquad (1)$$

has been fitted to the four spectral data points (Texas, 6 cm Greenbank and 2 and 20 cm VLA) to determine the peak frequency and peak flux density (columns 2 and 3 of table). Column 4 gives the spectral index ($S \sim \nu^{\alpha}$) below the peak, which is the spectral index between the Texas and the 20 cm VLA data point. Because this spectral index is measured very close to the

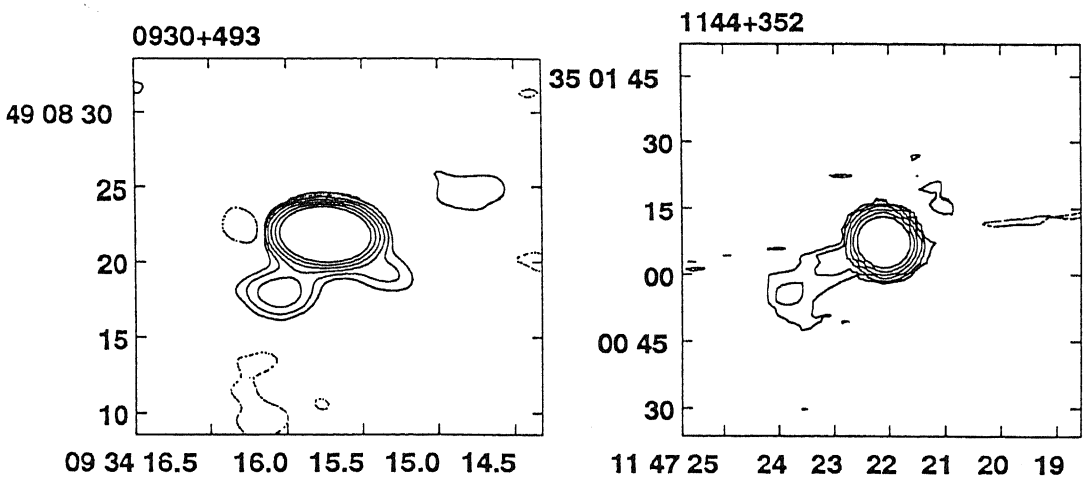

Fig. 2. (left) 20 cm VLA map of the components associated with 0930+493. Contourlevels are at 0.3 mJy x(-3, 3, 6, 12, 24, 48, 96, 192). (right) 20 cm VLA map of the jet eminating from the core of 1144+352. Contours at 0.7 mJy x(-3, 3, 6, 12, 24, 48, 96, 192)

Table 2. Sources with Definite Peaked Spectra

IAU name	ν_{max} (GHz)	S_{max} Jy	Spectral Index α_{1400}^{365}	α_{14700}^{4850}	Opt. ID	z	θ_{eq} mas	References for additional flux densities
0428+205[1]	1.3	3.8	0.21	-0.82	G	0.22	7	a, d, g
0700+470	1.3	0.7	0.33	-0.60	G			c, e, f, h
0706+460	1.0	0.4	0.43	-1.62				e
0930+493	1.7	0.8	0.37	-0.63	Q	2.57	4	h
1133+432[3]	1.2	1.16	0.55	-1.21				c, e, f
1144+542	2.6	0.5	0.24	-0.42	Q	2.20	2	c, h, i
1144+352	2.4	0.7	0.35	-0.56	G	0.06	2	b, f, h
1225+368[1,2]	1.1	2.02	0.36	-1.50	Q	1.98	12	c, h
1324+574	2.2	0.4	0.34	-0.05	G			h
1355+441	1.9	0.6	0.57	-0.63	G			c, e

[1] also in O'Dea et al. sample
[2] also in Fanti et al. sample
[3] also in Ghopal-Krishna'93 sample
additional data from literature:
a) Blake (1970)
b) Colla (1975)
c) Pauliny-Toth et al. (1978)
d) Parkes Catalogue (Bolton et al. 1979)
e) Bologna Sky Survey (Ficarra et al. 1985)
f) Cambridge 6C2 Survey (Hales et al. 1988)
g) Wright et al. (1991)
h) Patnaik et al. (1992)
i) Okudaira (1993)

peak this is an lower limit to the spectral index below the peak. The spectral index above the peak, given in column 5, is formed from the Greenbank 6 cm and the VLA 2 cm data points. Because of the curvature in the spectrum, these spectral indices are peak-frequency dependent. When the peak frequency is higher, the spectral index above the peak will be flatter, because it is measured closer to the peak.

Three sources have previously been optically identified with quasars, and two with galaxies (column 6, Véron-Cetty and P. Véron 1983; Stickel et al. 1994). Their redshift is known and is listed in column 7. We looked for optical identifications on the POSS-plates for the other sources. Faint optical identifications on the POSS plates (using APM data supplied by Richard McMahon, McMahon & Irwin 1992) are found for three additional sources, which are probably galaxies. To have an estimate

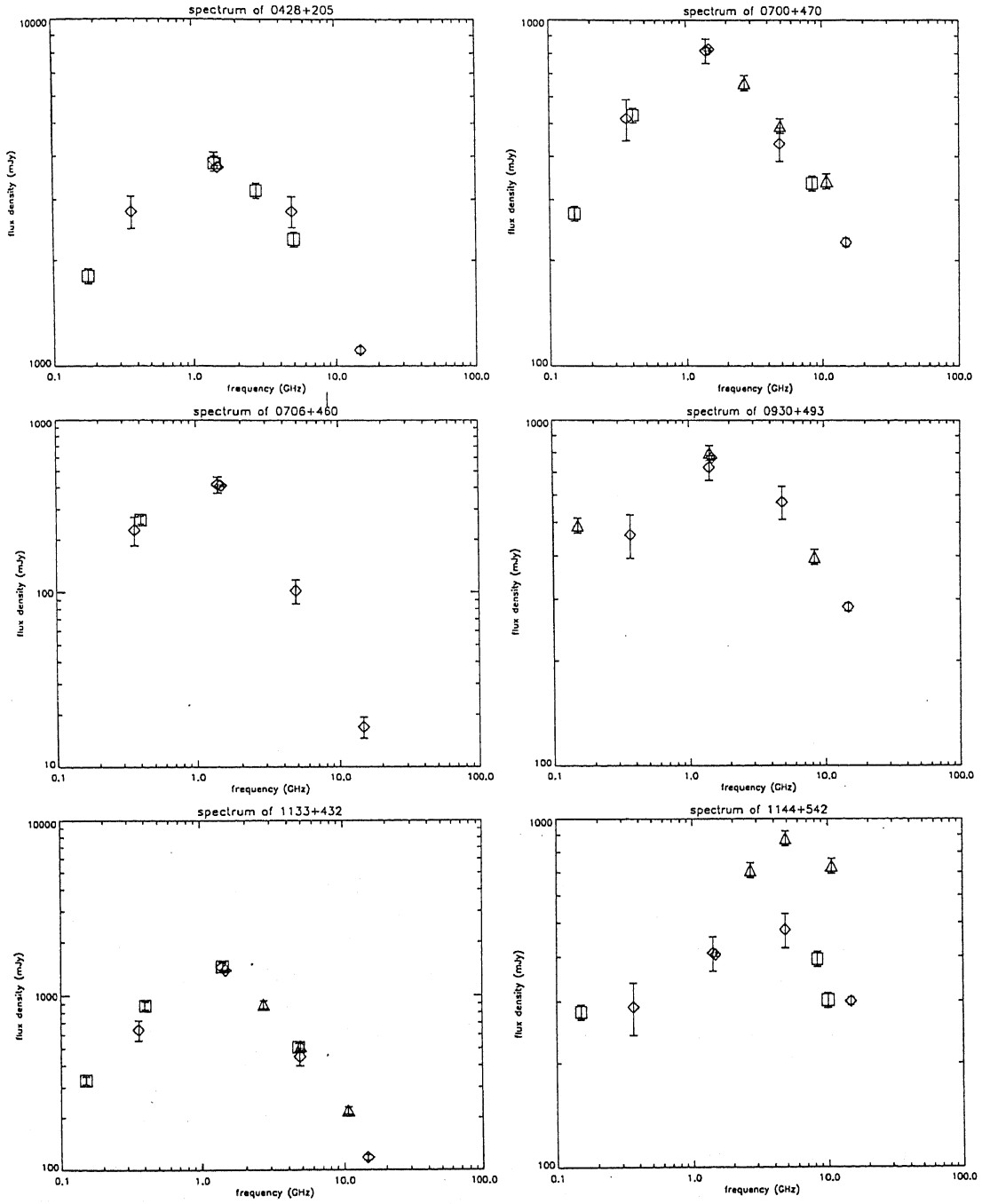

Fig. 3. Spectra of true peaked spectrum sources. The dotted line in the figure of 1144+352 indicates the spectrum of the extended emission

of the physical extent of the radio sources, we use the "equipartition angular size", θ_{eq}, derived by Scott & Readhead (1977). This is the size which a source with the given flux density and frequency at the synchrotron self-absorption turnover must have to be in equipartition. The angular size is only weakly dependent on the internal energy. Even if the source is ten times more energetic than assumed by the equipartition condition, the angular size will only be 25 percent larger. The equipartition angular size is given in column 8 of Table 2, assuming $H_0 = 50\ km\ s^{-1} Mpc^{-1}$ and $\Omega_0 = 1$. Upper limits for the angular sizes, obtained from our 2 cm VLA observations, are consistent with the equipartition angular sizes ($\theta < 20$ mas). 0428+205 and 1225+368 have been observed by Spencer et al. (1989) at 2 cm with the VLA in A configuration. 1225+368 is unresolved, but 0428+205 has probably a double or multi-component morphology, spread out over 100 mas. The true angular sizes and radio morphologies should be revealed using VLBI techniques.

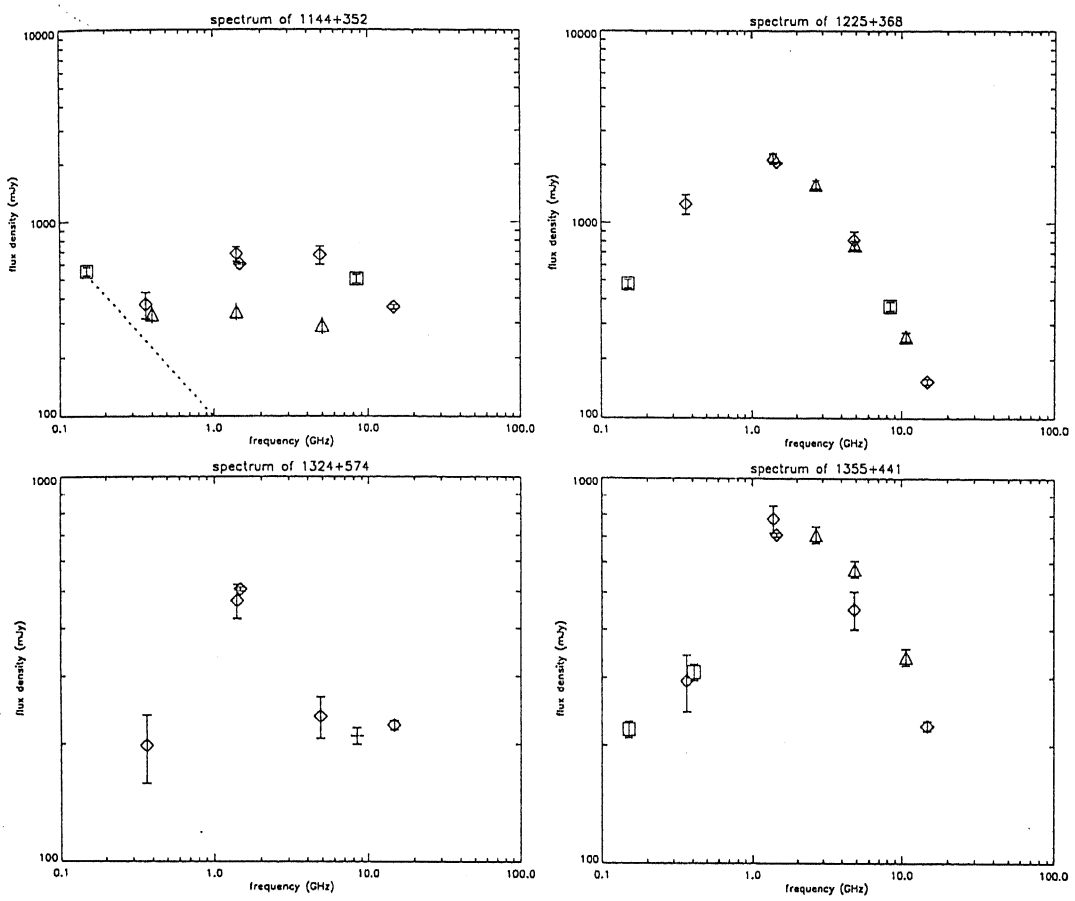

Fig. 3. (continued)

Figure 3 shows the radio spectra of the ten definitely peaked spectrum sources. The diamond symbols represent the VLA data points and the 6 and 20 cm Greenbank and Texas flux densities. The squares are data points from various papers in the literature, and the triangles are data points from Pauliny-Toth et al. (1978). The triangles in the figure of 1144+352 are data points from Colla et al. (1975).

5. Discussion on individual sources

The presence or lack of variability can give us information about the evolution of peaked spectrum sources. We shall attempt to explain this variability in terms of expansion of the radio core. We distinguish expansions with and without continuous injection of electrons by a central engine.

i) A radio source expanding isotropically and adiabatically from radius r to fr, without fresh injection of relativistic electrons, will cause the peak flux density to *decrease* by

$$f^{(10-14\alpha)/(5-2\alpha)} \quad (2)$$

where α is the spectral index of the optically thin part of the spectrum (Moffet 1975). The peak frequency will decrease by

$$f^{(10-8\alpha)/(5-2\alpha)} \quad (3)$$

ii) A radio source expanding with continuous injection of electrons will undergo an *increase* in flux density of f^2 and f^3 for respectively the optically thick and thin part of the spectrum, assuming that the magnetic field strength and electron density is constant during the expansion. In this case, the internal energy density and pressure remains the same during the expansion. The peak flux density will increase by a factor of

$$f^{(12-4\alpha)/(5-2\alpha)} \quad (4)$$

and the peak frequency will increase by a factor of

$$f^{2/(5-2\alpha)} \quad (5)$$

The most striking example of a *decrease* in flux of a radio source in our sample is 1144+542. Three flux density measurements, taken by Pauliny-Toth et al. (1978) in 1972, are a factor two higher than our measurements. If this is caused by an adiabatic expansion, the expansion factor f is ~ 1.3 (using $\alpha = -0.4$). This expansion mechanism would decrease the peak frequency by a factor 1.8. We do indeed see a peak frequency decrease of this size (see Fig. 3), but unfortunately there are only observations available at 2 epochs. Using the equipartition size, and taking the redshift from literature, we determine the expansion velocity to be of the order of 0.5 c.

A second source 1144+352 has *increased* in flux density over the last 20 years. In the early seventies the flux densities at 0.4, 1.4 and 5 GHz were respectively 330, 340 and 290 mJy (Colla et al. 1975), so it appears that the spectrum was flat. However, taking into account the non-variable extended emission ($S_{1.4GHz}$=100 mJy, α=-0.75, see below), the flux densities of the core can be estimated to be 70, 240 and 250 mJy at these three frequencies. Hence the spectrum of the core was peaked at that epoch, and has remained peaked during the flux density increase. The flux density at 6 cm has increased from 290 mJy in 1974 to 670 mJy in 1987 (30 ± 5 mJy/year, e.g. Ekers et al. 1983). An increase of this magnitude in the optically thin part of the spectrum can be caused by an expansion of 5×10^4 km/s, assuming expansion with continuous injection of electrons. The presence of a jet in the VLA map at 20 cm hints at a continuous outflow of matter. The flux density at 1.4 GHz in the optically thick region of the spectrum of the core increased from 340 mJy in 1974 (Colla et al. 1975) to 600 mJy in 1991. In the expansion scenario the optically thick flux density increase should be equal to the increase in the optically thin part of the spectrum to the power 2/3 (see (ii) above), which is what we see for 1144+352.

No variability is seen for the other sources in our sample, for which the redshift is known, on timescales of 5 to 15 years. The flux density measurements however are not accurate enough to give useful upper limits to the expansion velocities.

Two of our peaked spectrum sources, 0930+493 and 1144+352 show a change in spectral index at low frequencies from inverted to steep. We attribute this to contributions from extended structure with a steep spectrum, which dominates at the low frequencies. The 20 cm VLA maps of both sources show clearly the presence of extended structure; three components with a combined flux density of $\sim$ 15 mJy, within a radius of 10″ of the core of 0930+493 are detected, and a one sided jet about 25″ in extent with a flux density of $\sim$ 28 mJy emanating from the 1144+352 core (see Fig. 2). The 20 cm Greenbank flux density of 1144+352 is 80 mJy higher than the total 20 cm VLA flux density, which is probably due to large scale extended emission, not detected with the VLA. Hence the total flux density of the extended emission is about 100 MJy at 1.4 GHz. Assuming a spectral index of $\alpha = -0.75$ for the extended emission, its contribution at 151 MHz is more than 90% of the total flux density.

The spectrum of 1324+574 shows a flattening at high frequencies, which implies the existence of an even more compact component whose spectrum peaks at frequency > 20 GHz.

VLBI and optical studies will be undertaken to investigate their properties and compare them with those of bright peaked spectrum sources. We have also begun to define even fainter samples of peaked spectrum sources in the Westerbork Northern Sky Survey (WENSS).

6. Conclusions

We have presented 10 radio sources whose spectra peak between 1 and 2.5 GHz, with flux densities in the 1 Jy range. For 1144+542, a flux density decrease of a factor $\sim$ 2 in about 20 years is seen, which can be explained by the source expanding without fresh injection of relativistic electrons and with a velocity on the order of 0.5 c. For 1144+352, an increase in flux density over the last 20 years has been observed, which can be explained if the radio source expands with continuous injection of relativistic electrons.

References

Baum S. A., O'Dea C. P., Murphy D. M., de Bruyn A. G., 1990, A&A 232, 19

Blake G. M., 1970, ApJ 6, L201

Bolton J. G., Wright A. E., Savage A., 1979, Aust.J.Phys.Astrophys. Suppl. 46, 1

Carilli C. L., Perley R. A., Dreher J. W., Leahy J. P., 1991 ApJ 383, 554

Colla G., Fanti C., Fanti R., Gioia I., Lari C., Lequeux J., Ulrich M. H., 1975, A&AS 20, 1

Dallacasa D., Fanti C., Fanti R., Schilizzi R. T., Spencer R. E., 1995, A&AS submitted

de Bruyn A. G., 1990, Workshop on 'CSS and GPS radio sources', eds. C. Fanti and R. Fanti and C. P. O'Dea and R. T. Schilizzi, p206

de Bruyn A. G., 1991, in: Variability of Active Galaxies, eds. W. J. Duschl and S. J. Wagner, p105

Douglas J. N., Bash F., Torrence G. W. Wolfe C., 1980, The University of Texas Publications in Astronomy 17, 1

Ekers R. D., Fanti R., Miley G. K., 1983, A&A 297, 120

Fanti R., Fanti C., Schilizzi R. T., Spencer R. E., Nan Rendong, Parma P., van Breugel W. J. M., Venturi T., 1990, A&A 231, 333

Ficarra A., Grueff G., Tomassetti G., 1985, A&AS 59, 255

Gopal-Krishna, Spoelstra T. A. T., 1993, A&A 271, 101

Hales S. E. G., Baldwin J. E., Warner P. J., 1988, MNRAS 234, 919

McMahon R. G., Irwin M. J., 1992, in: Digitised Optical Sky Surveys, eds. T. MacGillivray and E. B. Thomson, p417

Moffet A. T., 1975, in: Stars and Stellar Systems, Volume IX, eds. A. Sandage and M. Sandage and J. Kristian, p211

Mutel R. L., Phillips R. B., 1988, in: Proc. of IAU Symp. No. 129 'The impact of VLBI on Astro- and Geophysics' eds. M. J. Reid and J. M. Moran, p73

O'Dea C. P., Baum S. A., Stanghellini C., 1991, ApJ 380, 66

Okudaira, 1993, PASP 45, 153

Patnaik A. R., Browne W. A., Wilkinson P. N., Wrobel J. M., 1992, MNRAS 254, 655

Pauliny-Toth I. I. K., Witzel A., Preuss E., Kuhr H., 1978 AJ 83, 451

Peacock J. A., Wall J. V., 1982, MNRAS 198, 843

Perley R. A., 1982, AJ 87, 859

Phillips R. B., Mutel R. L., 1980, ApJ 236, 89

Röttgering H. J. A., Lacy M. Miley G., Chambers K., Saunders R., 1994, A&AS 108, 79

Rudnick L., Jones T. W., 1982, ApJ 255, 39

Schilizzi R. T., 1990 Workshop on 'CSS and GPS radio sources', eds. C. Fanti and R. Fanti and C. P. O'Dea and R. T. Schilizzi, p1

Schwab F. R., 1984, AJ 89, 1076

Scott M. A., Readhead A. C. S., 1977 MNRAS 180, 539

Slysh V. I., 1963, Nat 199, 682

Spencer R. E., McDowell J. C., Charlesworth M., Fanti C., Parma P., Peacock J. A., 1989, MNRAS 240, 657

Stickel M., Kühr H., 1993, A&AS, 103, 349

Véron-Cetty M. P., Véron P., 1983 A&AS 53, 219

Williams I. P., 1963, Nat 200, 56

Wright A. E., Wark R. M., Troup E., Otrupcek R., Jennings D., Hunt A., Cooke D. J., 1991, MNRAS 251, 330